NEOGENE EXHUMATION OF THE SIKKIM HIMALAYA FROM ZIRCON (U-TH)/HE THERMOCHRONOLOGY AND 3-D THERMO-KINEMATIC MODELLING

by

Kyle R. Landry

Submitted in partial fulfillment of the requirements
for the degree of Master of Science

at

Dalhousie University
Halifax, Nova Scotia
August 2014

TABLE OF CONTENTS

LIST OF TABLES

LIST OF FIGURES

ABSTRACT

Erosion and exhumation of upper crustal material in active orogens, like the Himalaya, result from a combination of both tectonic and surface processes. Although recent studies have well defined the Miocene-Pliocene exhumation history and deformation kinematics along most of the length of the Himalayan arc, the exhumational history and late Tertiary tectonic model of the Sikkim Himalaya are still poorly constrained. In Sikkim, the Indo-Tibetan convergence is accommodated along the Main Himalayan Thrust (MHT), a crustal scale décollement that currently reaches the surface through the Main Boundary Thrust (MBT) and the Main Frontal Thrust (MFT), at the toe of the orogenic prism. Erosion in central Sikkim has uncovered a double tectonic window exposing the underlying Lesser Himalayan Sequence (LHS) through the overlying nappe of Greater Himalayan Sequence (GHS). Within the windows, the LHS is structured in a duplex system which is thought to have accommodated significant amounts of horizontal shortening. The goal of this study is to discriminate between tectonic scenarios that might have impacted the exhumational history of the Sikkim Himalaya and determine the relative contribution of steady displacement on the MHT combined (or not) with duplexing in the LHS.

This study adopts a multi-faceted approach involving (U-Th)/He thermochronology on zircon (ZHe) coupled with 3-D thermokinematic modelling. Fifteen rock samples collected along two N-S-trending profiles across the Rangit and Tista Windows yielded cooling ages ranging from 11.87 ± 0.49 Ma to 1.30 ± 0.07 Ma. Approximately 20 - 30 km north of the MBT, the ZHe cooling age distribution shows an abrupt decrease; south of this break cooling ages range from ~12 to ~6 Ma, and north of it, within the double window and beyond, ages are younger than ~4 Ma. This break corresponds roughly to the southern exposure of the LHS units within the windows.

The age dataset was inverted using the thermo-kinematic modelling software *Pecube* to define the Late Miocene to present deformation and exhumation kinematics of the Sikkim Himalaya. Model scenarios were run both with and without the presence of a duplex. We find that a tectonic scenario only involving steady displacement on the basal décollement (MHT) during the last 12 Ma does not provide a satisfactory fit to the age data, while when combined with localized duplex-driven rock uplift in the LHS, it reproduces the young ages observed in the core of the double window. These results suggest that the MHT is not the only tectonic control on exhumation in Sikkim and that duplexing is a key process in the tectonic evolution of Sikkim since the late Miocene.

LIST OF ABBREVIATIONS USED

TSS	Tethyan Sedimentary Sequence
STDZ	South Tibetan Detachment Zone
GHS	Greater Himalayan Sequence
MCTZ	Main Central Thrust Zone
HHT	High Himalayan Thrust
MCT	Main Central Thrust
LHS	Lesser Himalayan Sequence
RT	Ramgarh Thrust
MBT	Main Boundary Thrust
MFT	Main Frontal Thrust
MHT	Main Himalayan Thrust
GPS	Global Positioning System
ZHe	Zircon (U-Th)/He
NA	Neighbourhood Algorithm
Ma	Mega Anum (Million Years)
AFT	Apatite Fission Track
OSL	Optically Stimulated Luminescence
TSL	Thermally Stimulated Luminescence
LVZ	Low Velocity Zone
INDEPTH	International Deep Profiling of Tibet and the Himalaya
ITRF	International Terrestrial Reference Frame

SRTM	Shuttle Radar Topography Mission
DEM	Digital Elevation Model
HePRZ	Helium Partial Retention Zone
SPT	Sodium Polytungstate
MI	Diiodomethane
UCSC	University of California Santa Cruz
ICP-MS	Inductively Coupled Mass Spectrometer
HF	Hydrofluoric Acid
HNO_3	Nitric Acid
SA/V	Surface Area to Volume Ratio
Ga	Giga Anum (Billion Years)
ka	Kilo Anum (Thousand Years)
PDF	Probability Density Function

ACKNOWLEDGEMENTS

I'd first and foremost like to thank my supervisor, Isabelle Coutand, whose patience and guidance have been instrumental in encouraging me to both start and complete this thesis. Also, Dave Whipp was invaluable in helping me to both use *Pecube* and understand how it works. I'd like to thank my committee members (Dave Whipp, Martin Gibling and John Gosse) for their constructive comments on various parts of the project and especially on the final submission. Keith Taylor and Jeremy Hourrigan (UCSC) were instrumental in helping me complete my age analysis. I'd like to thank all of the rest of the faculty and staff in the Earth Sciences department at DAL for all the help and support given to me over the past two degrees. Finally I'd like to thank the other grad students who have worked and studied with me over the past three years for the good times had.

Chapter 1 - Introduction

The mechanisms which control exhumation across the Himalayan orogen and the interactions between them have seen substantial debate over the past decade. Erosion and exhumation of the Himalaya are controlled by the interactions between tectonic and climatic processes (e.g., Beaumont et al., 2001; Hodges et al., 2004; Grujic et al., 2006; Whipple and Meade, 2006; Whipple, 2009). In convergent orogens, tectonic processes such as thrust faults transport material towards the surface while climatic processes and associated surface processes (e.g. river erosion, mass movement) erode the surface. The net result is exhumation (or burial where sedimentation outpaces erosion). However, the contribution of tectonic processes to the observed upper crustal exhumation and the mechanisms by which they have done so remain poorly constrained. This study adopts a multi-faceted approach, coupling (U-Th)/He thermochronology on zircons and 3D-thermokinematic Modelling, to test and refine conceptual tectonic models for the Eastern Himalaya in Sikkim (India) and to highlight the key tectonic mechanisms that may have contributed to the late Neogene (12 Ma to present) development of this part of the orogen. Previous thermochronological and modelling studies have primarily focused on the western and central Himalaya where findings about crustal deformation, exhumation, and the resulting thermal structure have been extrapolated to other parts of the orogen (e.g., Gansser, 1964; Avouac, 2003; Bollinger et al., 2004; Hodges 2004; Wobus et al., 2005; Herman et al., 2010; Robert et al., 2011). However, the applicability of previous studies to the Sikkim Himalaya is limited because this part of the range is located in a transition zone between Nepal to

the west (e.g., Whipp et al., 2007, Herman et al., 2010) and Bhutan to the east (e.g., Grujic et al., 2006; Coutand et al., 2014) (Figure 1.1), each area having different structural and morphological characteristics. These along-strike variations are detailed in Chapter 2.

1.1 - Orogen-Scale Geologic Setting

The Himalaya, the largest active collisional orogenic system on earth, is the result of collision between the Indian and Eurasian plates. From west to east, the orogen spans over 2500 km between its two syntaxes, from Nanga Parbat in Pakistan to Namche Barwa in the Arunachal Pradesh state of India, the entire range curving in a concave-to-the-north arc (Figure 1.1) (LeFort, 1975). The range has a total width of about 200-250 km and is bounded to the south by the Gangetic Plains of northern India and to the north by the Tibetan plateau.

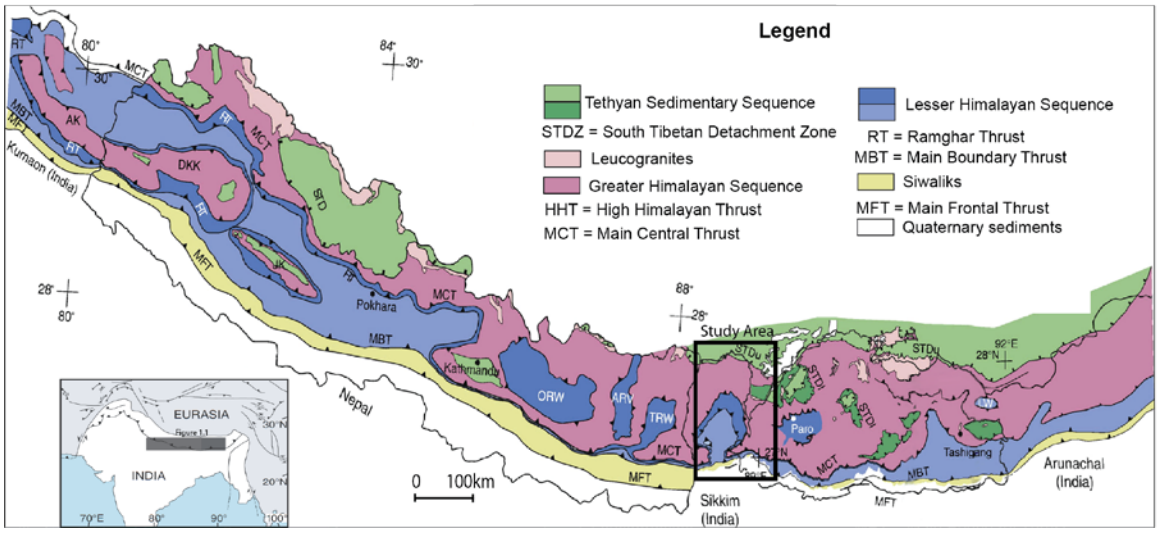

Figure 1.1: Geological map of the Himalaya showing the major geological units and bounding structures. The inset map in the bottom left corner shows the surface covered by the map on a continental scale. The black box on the map shows the location of the study area. (McQuarrie et al., 2008).

The Indian subcontinent was connected to northern Gondwana until the Jurassic when rifting caused the breakup of Gondwana, allowing India to move northwards (Segev, 2002). Collision of the Himalayan Range began at ~55 Ma (e.g., LeFort, 1975; Patriat and Achache, 1984; Besse et al, 1984) when the drifting Indian plate collided with the Eurasian plate (Figure 1.2). Paleomagnetic reconstructions suggest that initial collision occurred at ~10 ° N latitude (Patriat and Achache, 1984) and that ~2600 ± 900 km of convergence has taken place since then (Patriat and Achache, 1984; Molnar and Stock, 2009). Although collision has progressed more or less continuously since ~55 Ma, the convergence rate between India and Eurasia has apparently not been constant over geologic time, likely slowing down from 57 mm/a to 44 mm/a (in the NE corner of India) and from 44 mm/a to 34mm/a (in the NW corner of India) sometime between 20-10 Ma (Molnar and Stock, 2009). More recently, it has been suggested that the convergence velocity has decreased exponentially since before collision occurred (~67 Ma; Clark, 2012).

Along the entire length of the Himalaya, the major geological units and their bounding structures are remarkably continuous with little variation in their petrological composition and structural arrangement. From north to south, these units/structures are: the Tethyan Sedimentary Sequence (TSS), South Tibetan Detachment Zone (STDZ), Greater Himalayan Sequence (GHS), Main Central Thrust (MCT), Lesser Himalayan Sequence (LHS), Main Boundary Thrust (MBT), Siwalik Group, Main Frontal Thrust (MFT) and foreland basin sediments (Figure 1.1) (e.g., Hodges, 2000).

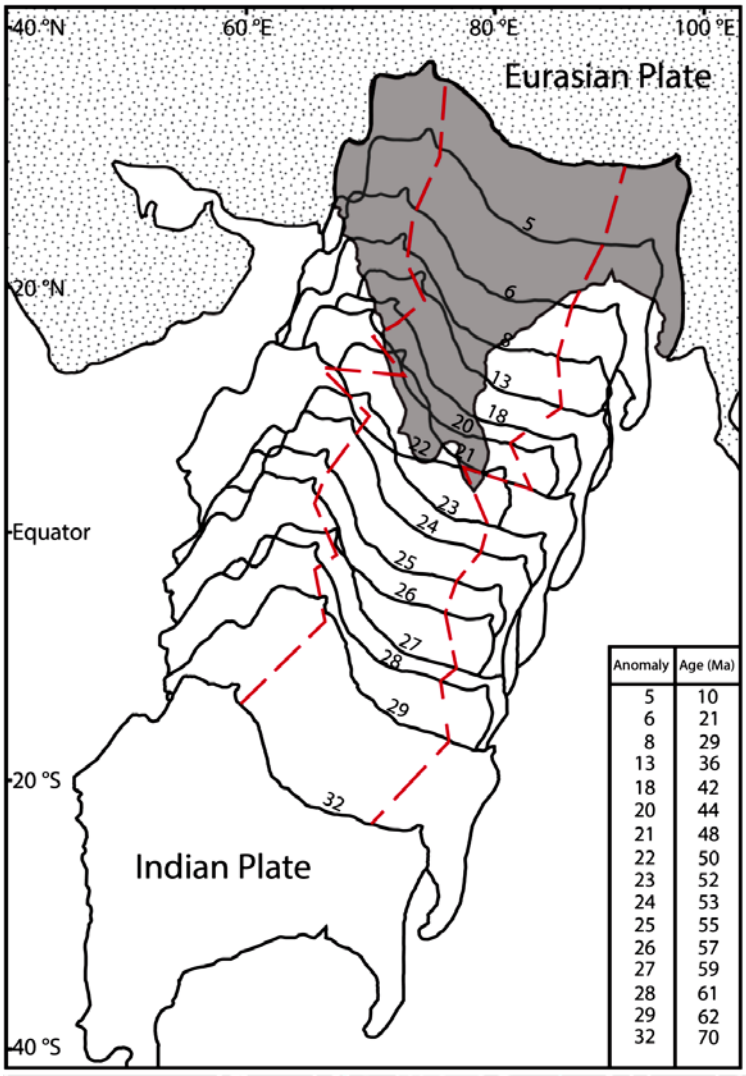

Figure 1.2: Paleomagnetic reconstruction showing the northern drift of the Indian subcontinent from 70 Ma, through collision at ~55 Ma and to the present. Each anomaly represents a specific magnetic reversal which was dated and correlated with the location of the Indian subcontinent at that time. The red dashed lines show the relative motion of two static points on the subcontinent. The grey shaded section shows the current position of India. (From Patriat and Achache, 1984).

The TSS is a Cambrian to Eocene low-grade metasedimentary sequence (Gansser, 1964; Gaetani and Garzanti, 1991) bounded to the north in Tibet by the Indus-Tsangpo Suture, the boundary between the Indian and Eurasian plates, and to the south by the northward-dipping normal-sense shear zone known as the STDZ. Structurally

below and to the south of the STDZ is the GHS, a series of medium-to-high metamorphic-grade gneisses, metasediments, and migmatites intruded by Miocene leucogranites (e.g., Hodges, 2000). It is bounded to the south by the MCT ductile shear zone, which overlies an 8-10 km thick package of Proterozoic to Permian marine metasedimentary rocks known as the LHS (e.g., Hodges, 2000). The base of the LHS is bounded to the south by the MBT, the second oldest major north-dipping thrust fault in the Himalayan range front, which is a fairly narrow zone (<100 m wide) of cataclasis (Schelling, 1992; Meigs et al 1995). To the south of the MBT are strata of the Siwalik Group, a series of syn-orogenic sedimentary rocks derived from the eroded material of topographically and structurally higher units and deposited in the foreland basin (e.g., Gansser, 1983). The southern boundary of the Siwaliks is the MFT, the youngest of the major south-propagating thrust faults and active toe of the orogen. The MFT, MBT and MCT branch at depth from the Main Himalayan Thrust (MHT; Nelson et al., 1996) which is the basal detachment of the modern Himalayan orogenic wedge.

1.2 - Tectonic Models for Neogene Development of the Present Orogenic Front

Different models have been used to explain different parts of the growth history of the Himalaya. One of these is the channel flow model (e.g., Beaumont et al., 2001; 2004; Grujic et al., 2002; Godin et al., 2006) which involves the lateral migration, extrusion and exhumation of partially molten mid-crustal material due to localized climatically-induced surface erosion. Exhumation occurs through concurrent and opposite displacement on structures bounding the paleo-channel. In the Himalayan case the GHS is bounded by two north-dipping opposite-sense shear zones, the thrust-sense

MCT in the south and normal-sense STDZ in the north, both active from at least the Early Miocene (~23 Ma) until the late Middle Miocene (~10 Ma at the latest; e.g., Godin et al., 2006; Grujic et al., 2006; Harris et al., 2006; Catlos et al., 2007). Channel flow is a ductile process; it can only occur at temperatures above the brittle-ductile transition. Thus when the channel rocks cooled, exhumation of material continued through brittle processes (Grujic et al., 2006) such as thrusting along newer major north-dipping faults (e.g., MBT), or re-activation of older shear zones (e.g., MCT). Metamorphic petrology coupled with geochronology suggests that in the eastern Bhutan Himalaya channel flow, and associated ductile deformation, ceased by ~10 Ma (e.g., Grujic et al., 2011).

Deformation in the cooler upper crust occurs for the most part in brittle fashion and can be described using the critical wedge model (Davis et al., 1983), commonly applied to active fold-and-thrust belts (e.g., Dahlen, 1990). The wedge features (Dahlen, 1990; Figure 1.3) a basal décollement (a large orogen-scale thrust fault) with a dip angle of β along which the wedge slides. The average topographic surface of the wedge has an angle, α. The angle $\alpha+\beta$ is called the taper of the wedge and can be used to determine what state the wedge is in. The taper can be modified through changes in erosion, sedimentation or internal deformation.

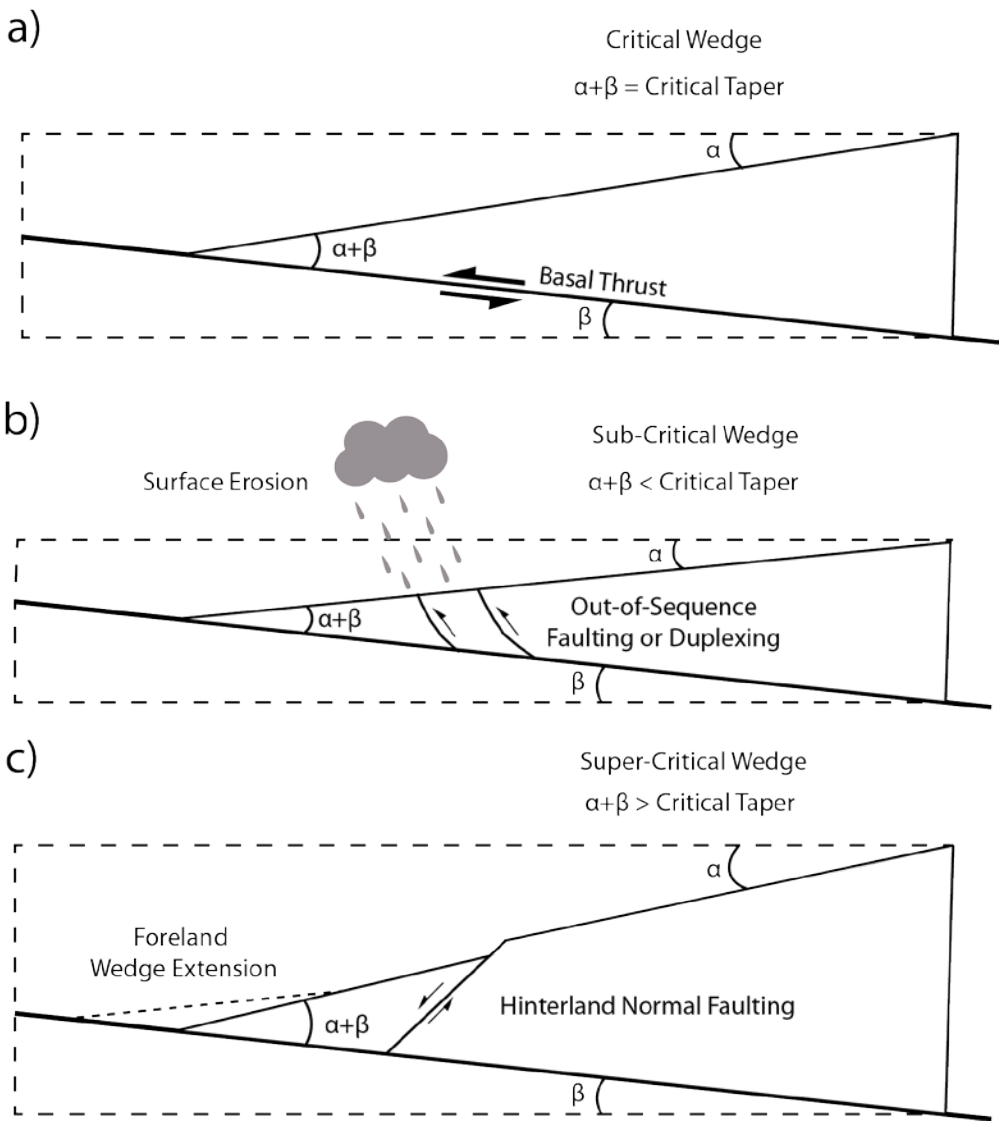

Figure 1.3: Three states of a wedge under the critical wedge model. Overthrusting is to the left of the diagrams along a basal thrust. a) A critical wedge where the wedge propagates along the basal thrust without internal deformation, b) a sub-critical wedge where thinning of the wedge is balanced by internal thrusting and wedge thickening and c) a super-critical wedge where an over-thickened wedge is thinned by normal faulting and extension of the wedge toward the foreland.

In this model, the Himalayan wedge can be approximated by one of three states: critical, sub-critical or super-critical (e.g., Mitra, 1997; Figure 1.3). The critical wedge state (Figure 1.3a) is an equilibrium state where the wedge advances along its basal décollement, the MHT in the Himalaya, without the need for internal deformation of the

wedge, which grows via basal accretion. This occurs when a critical taper angle (α+β) is maintained through a balance of forces that thicken and thin the wedge. A sub-critical state (Figure 1.3b) occurs when the taper of the wedge is at an angle shallower than the critical taper, due to erosion at the surface, and the wedge must thicken internally through the formation of out-of-sequence thrusts and duplexes. A super-critical state (Figure 1.3c) occurs in the case where the taper is at an angle higher than the critical taper and must compensate through normal faulting in order to extend the wedge and lower the angle of repose. In the cases of both sub- and super-critical wedges, the purpose of internal deformation is to return to the equilibrium state of the critical wedge (Davis et al., 1983). It has been suggested from activity on presumed out-of-sequence faults north of the MFT that the Sikkim wedge may be in a sub-critical state (Mukul, 2000). While the Sikkim range-front can be approximated to first order to have been a critical wedge since at least 10 Ma, the tectonic model that best describes the evolution of the wedge during that time frame is still under debate.

It is important to note that the channel flow and critical wedge models are not mutually exclusive. While these two models describe different processes, Jamieson and Beaumont (2013) showed that the models can coexist within the Himalaya with brittle critical wedge mechanics governing the fold-thrust belt to the south of the exhumed channel and that they can occur contemporaneously.

There are currently three major tectonic models to account for the development of the frontal part of the Himalaya from the Late Miocene to the present (Figures 1.4 a-c):

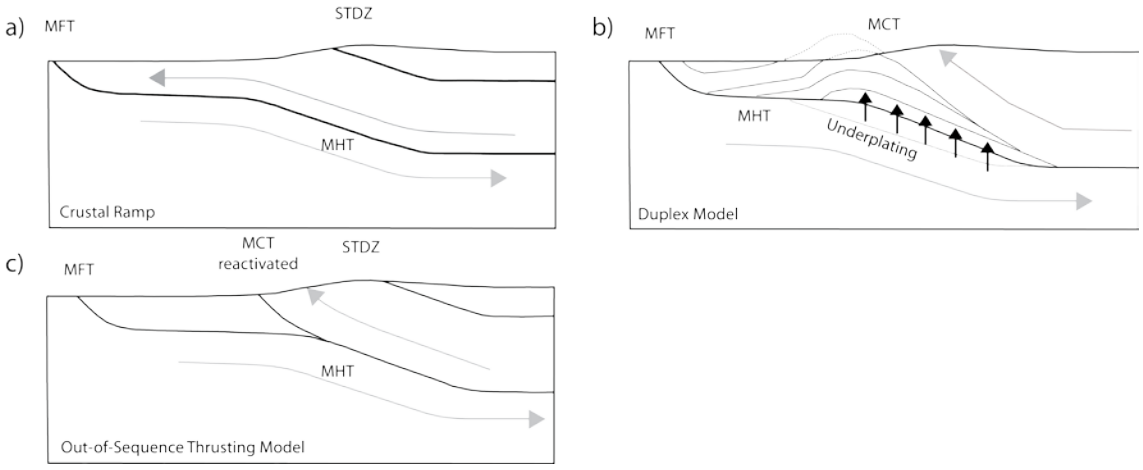

Figure 1.4: Tectonic models of the Himalayan wedge for the late Neogene. a) Model of a wedge overthrusting the foreland on a geometrically variable basal décollement (MHT). Grey arrows show the particle pathway on both sides of the décollement. b) Out-of-sequence thrusting in a wedge in sub-critical state. c) Development of a duplex at mid-to-upper crustal depths above a crustal ramp. Black arrows show the area where underplating is occurring (Modified after Herman et al., 2010).

The first model involves overthrusting of the orogenic wedge on a major crustal-scale basal décollement with a ramp-and-flat geometry (e.g., Gansser, 1964, Herman et al., 2010; Robert et al., 2009, 2011) (Figure 1.4a). The basal décollement, the MHT, is characterized by ramp-and-flat sections as constrained by geophysical data (e.g., Nelson et al., 1996; Alsdorf et al., 1998; Nábělek et al, 2009; Acton et al., 2011). In this model, enhanced exhumation occurs at the surface above the ramp segments due to the more vertical particle path combined with steady-state topography (Robert et al., 2011; Coutand et al., 2014). Robert et al., (2009; 2011) used thermokinematic Modelling of thermochronologic data to suggest that lateral changes in the MHT geometry may be the primary control of upper crustal exhumation along the orogen.

The second model involves the growth of a mid-crustal duplex on top of a ramp segment of the MHT (e.g., Avouac, 2003, Bollinger et al., 2004, Herman et al., 2010)

(Figure 1.4b). Duplexes accommodate India-Eurasia convergence through horizontal shortening in the brittle domain of the crust (e.g., in Nepal, DeCelles et al., 1998; in Bhutan, McQuarrie et al., 2008; in Sikkim, Bhattacharrya and Mitra, 2011). These structures propagate from the hinterland to the foreland and in most cases are located within the LHS. The duplex systems are arranged in a series of repeating north-dipping imbricate slices of LHS and, in the cases of Sikkim and Nepal, by antiformal stacks in the foreland portion of the LHS (Mitra et al., 2010). This arrangement forms a surface pattern of repeated slices of the same cycle of LHS units, which results in thickening of the wedge (e.g., Bhattacharrya and Mitra, 2009). Underplating of material transported across the MHT from the underlying Indian crust, as is the case in this model, locally increases rock uplift rates and, at topographic steady-state, locally enhances upper crustal exhumation (e.g., Herman et al., 2010). In Sikkim, Bhattcharrya and Mitra (2009) used structural analysis to show the presence of a 40 km-long N-S trending duplex beneath the Rangit and Tista windows (Figure 1.1). Through cross-section balancing, Mitra et al. (2010) suggested that duplexing may be responsible for accommodating up to >95% of horizontal shortening in the Sikkim and Bhutan LHS during the late Miocene.

The third model involves out-of-sequence thrusting where the MCT, with ductile activity that mostly concluded at the end of the middle Miocene, was reactivated in the Plio-Pleistocene due to sustained climatically focused erosion (e.g., Mukul, 2000; Hodges 2004; Wobus et al., 2005) (Figure 1.4c). Detailed structural mapping by Hodges et al. (2004) in the Marsyandi valley in Nepal suggested the existence of south-vergent Quaternary thrust faults located south of the MCT. Using *in situ* cosmogenic ^{10}Be data

combined with $^{40}Ar/^{39}Ar$ data, Wobus et al. (2005) found evidence of an age discontinuity just over 20 km south of the MCT, north of the active MFT, and interpreted it to represent the trace of a re-activated thrust.

The goal of this study is to discriminate between these three hypotheses and develop a best-fit model for existing and new structural, geophysical and thermochronological data for the tectonic development of the range-front in Sikkim from 12 Ma to the present. Distinguishing which of the models best describes the current active orogenic front is important because the kinematics and geometry of the major structures across the orogen, combined with topography-modifying surface processes, can strongly affect the thermal structure of the mid-to-upper crust (e.g., Mancktelow and Grasemann, 1997; Ehlers, 2005; Whipp et al., 2007, Herman et al., 2010, Robert et al., 2011). We present new low-temperature thermochronological data consisting of 15 zircon (U-Th)/He samples distributed along a NNW-SSE oriented transect cutting across the major structures in Sikkim (Figure 1.1). This dataset will be used as input for 3D-thermokinematic modelling using a modified version of the software *Pecube* (Braun, 2003; Braun et al., 2012). This study focusses on the tectonic aspect of the problem, specifically, discriminating between possible tectonic hypotheses. Three scenarios were tested: 1) the variation of the geometry and kinematics of the basal décollement (MHT), 2) the development of a duplex at mid-to upper crustal depth combined with slip along the MHT, and 3) variation on the timing of initiation of duplexing.

Chapter 2 - Geological Setting

2.1 – Introduction

The Indian Province of Sikkim is located in the eastern Himalayan orogen between Nepal to the west, Bhutan to the east, and Tibet to the north (Figure 1.1). Although the major geological units and structures in Sikkim are, on first approximation, similar to those observed at the scale of the orogen (see Chapter 1), the Sikkim Himalaya presents unique lithological, structural and geomorphological features that I introduce in detail in this chapter.

2.2 – Geology of Sikkim

2.2.1 - Tethyan Sedimentary Sequence (TSS) and South Tibetan Detachment Zone (STDZ)

The Tethyan Sedimentary Sequence (TSS) has been mapped as a continuous unit in the northern part of Sikkim and extends northwards into Tibet (Figure 2.1). However, it has not been formally described in Sikkim and observations from neighbouring Nepal and Bhutan (e.g., Garzanti 1999; Kellett et al., 2012) are used here. It is composed of unmetamorphosed to greenschist facies marine shales and carbonates, associated with continental sandstones and conglomerates of Devonian to Jurassic age (Gaetani and Garzanti, 1999; Kellett et al., 2012). The sequence overlies a discontinuous higher-grade unit of greenschist-to-amphibolite-grade metasediments (Gansser, 1964) locally known as the Chekha Group in Bhutan or the Everest Group in Nepal (e.g., Kellett et al., 2012). An isolated slice of slate and schist overlain by sandstone, quartzite and marble mapped within the TSS in northwestern Sikkim (Pan et al., 2004) has similar metamorphic

characteristics and occupies the same structural level as the Chekha Group in Bhutan (Kellett et al., 2013), and may be an equivalent unit.

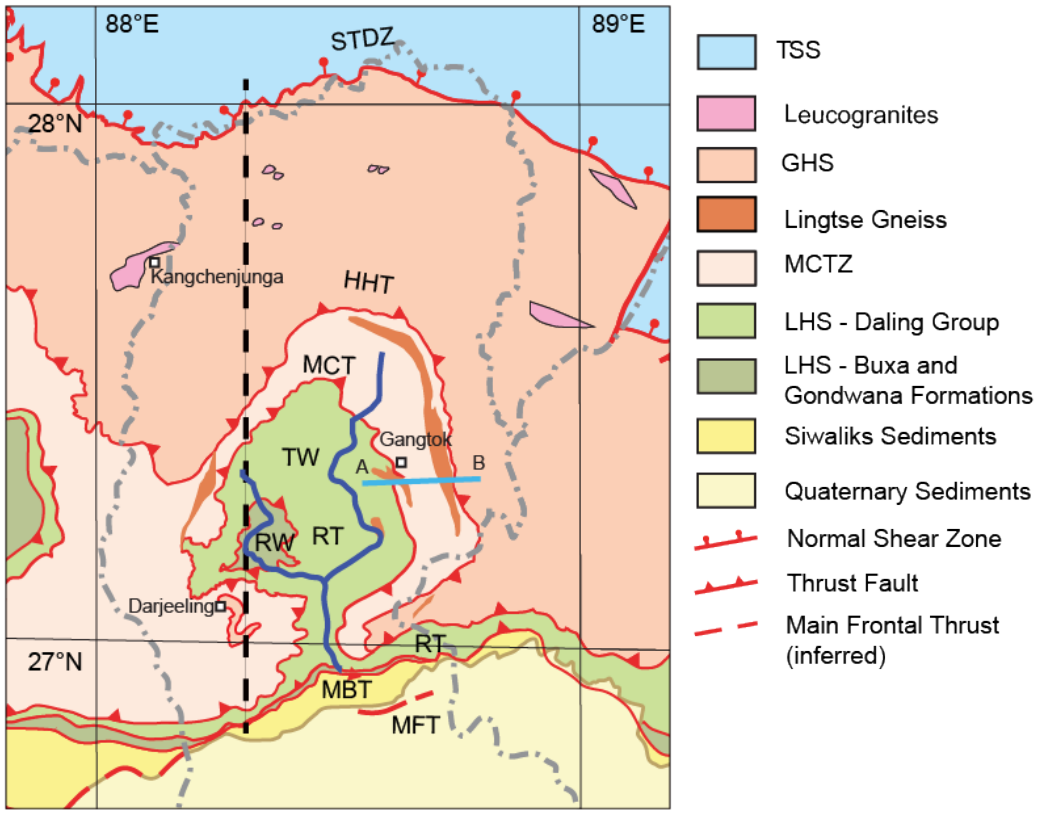

Figure 2.1: Geological map of Sikkim (for location, see Figure 1.1). TSS - Tethyan Sedimentary Sequence, GHS - Greater Himalayan Sequence, MCTZ - Main Central Thrust Zone, LHS - Lesser Himalayan Sequence, STDZ - South Tibetan Detachment Zone, HHT - High Himalayan Thrust, MCT - Main Central Thrust, MBT - Main Boundary Thrust, MFT - Main Frontal Thrust, RT - Ramgarh Thrust, TW - Tista Window, RW - Rangit Window. Note that the GHS located in the hanging wall of the MCT and HHT has been deeply incised, exposing the underlying LHS within the Tista half-window, itself containing the Rangit full-window. The main channels of the Rangit and Tista rivers are shown in dark blue, passing through their respectively named windows. The dashed black line indicates the location of the cross section shown in Figure 2.2. The solid light blue line shows the approximate location of the profile in Figure 2.3. The location of the Lingtse Formation is from Mottram et al., 2014. The map is modified from Grujic et al., 2011.

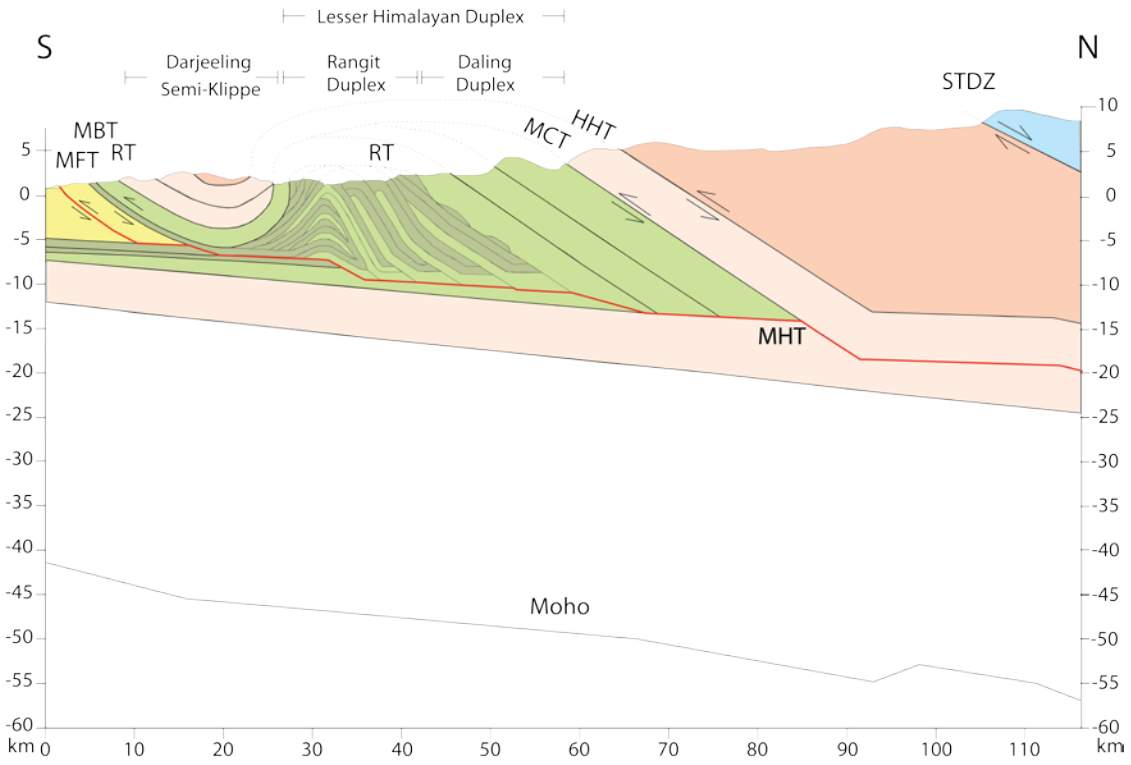

Figure 2.2: Interpretative section across the Sikkim Himalaya showing the main geological units and structures. Colour coding and abbreviations are same as for Figure 2.1. The major thrust faults, the MFT, MBT, RT and MCT root on the MHT at depth. The MHT is outlined in red. Location of the Moho is from Acton et al., 2011. Modified from Mitra et al., 2010.

The TSS is bounded to the south by the South Tibetan Detachment Zone (STDZ) (Figures 2.1 & 2.2), a northward shallow-dipping normal-sense shear zone (e.g., Burg and Chen, 1984; Burchfiel and Royden, 1985; Burchfiel et al., 1992). In Sikkim, it was recently described as a composite structure comprising a ductile, north-dipping, low-angle shear zone cut by a steeper north-dipping network of brittle normal faults (Kellett et al., 2013). The footwall of the STDZ is composed of the metamorphic Greater Himalayan Sequence (GHS) described in the following section.

Onset of motion along the ductile section of the STDZ in Sikkim occurred at ~23 Ma as documented by U-Th-Pb dating of prograde monazites within garnets sampled

from the STDZ footwall (Kellett et al., 2013). U-Pb dating of undeformed leucogranites (i.e., no ductile shearing) located in the footwall (< 5 km south of the STDZ) suggests that ductile motion ended by ~13 Ma, about 2 Ma earlier than in neighbouring Bhutan (Kellett et al., 2009). AFT (apatite fission track) and AHe (Apatite (U-Th)/He) data from one leucogranite sample located in the immediate footwall of the STDZ yielded near-identical ages of 12.9 $\pm$ 0.7 and 12.8 $\pm$ 0.8 Ma, respectively, indicating very fast cooling from temperatures of about 400°C, and are interpreted as representing the timing of ductile activity on the STDZ in Sikkim. $^{40}Ar/^{39}Ar$ data on muscovites from these leucogranites yielded total gas ages ranging from 12.4 ± 0.7 to 13.3 ± 0.4 Ma, within the same range to slightly older than the AFT and AHe ages from the same samples. Finally, biotite and muscovite $^{39}Ar/^{40}Ar$ ages in the Sa'er region between Sikkim and Nepal show rapid cooling after the end of ductile deformation between 13.6 and 11 Ma suggesting that brittle activity ceased at that point (Leloup et al., 2010).

2.2.2 - Greater Himalayan Sequence (GHS) and Main Central Thrust Zone (MCTZ)

The Greater Himalayan Sequence (GHS) is exposed in the footwall of the STDZ (Figure 2.1) and is composed of high-grade metamorphic rocks of both igneous and sedimentary origin intruded by leucogranites, as observed elsewhere in the Himalaya (e.g., LeFort, 1975; Schwan, 1980; Hodges, 2000). The high-grade metamorphic crystalline rocks of Sikkim are divided into the Darjeeling and Lingste Formations (e.g., Acharya, 1975). The predominant Darjeeling Formation (also known as the Darjeeling Gneiss Unit) is composed of stromatic migmatites of pelitic origin, associated with less common calc-silicates, metabasites, augen gneisses and minor quartzites (Ghosh, 1968;

Neogi et al., 1998). The GHS is exposed in the hanging wall of the MCTZ and extends northwards to the STDZ; it is also found further south where remnants are preserved in the Darjeeling klippe (Figure 2.1) (e.g., Mohan et al., 1989). The Lingtse Formation (or Lingtse Gneiss) is present in isolated slivers located structurally above both the MCTZ and LHS to the south (e.g., Mohan et al 1989; Mottram et al., 2014; Figure 2.1). The unit is composed of pelitic schists, psammites, quartzites, calc-silicates and orthogneiss (Paul et al., 1982; Neogi et al., 1998), is well foliated to highly mylonitized (Dasgupta et al., 2009), and has been used in previous studies as a marker for the location of the MCT shear zone (e.g., Neogi et al., 1998).

In Sikkim the MCT shear zone is represented by a 10 - 15 km wide zone of GHS rocks that have undergone ductile deformation, referred to as the MCTZ (Figures 2.1 & 2.2, e.g., Neogi et al., 1998; Harris et al., 2004; Mottram et al., 2014). It is bounded by two north-dipping thrust-sense shear zones variably called MCT1 and MCT (e.g., Catlos et al., 2004), MCT2 and MCT1 (e.g., Bhattcharyya and Mitra, 2009) or MCT and HHT (High Himalayan Thrust; e.g., Grujic et al., 2011) for the southern and northern structures, respectively (Figures 2.1 & 2.2). The terminology MCT and HHT will be used herein. The rocks present in the MCTZ are known as the Paro Formation (e.g., Acharya 1975) and are primarily composed of biotite-muscovite schists (Harris et al., 2004). The MCTZ, along with the upper LHS and lower GHS, preserves an inverted metamorphic sequence documented across the Himalaya (e.g., Mohan et al., 1989, MacFarlane et al., 1995; Harrison et al., 1997; Grujic et al., 2002) where the metamorphic grade progressively increases towards higher structural levels (from the LHS to the GHS).

Across the MCTZ the metamorphic grade increases from chlorite + biotite grade in the Daling schists of the LHS, increasing to the garnet-, staurolite-, kyanite- and sillimanite-in isograds, and finally to the sillimanite+K-feldspar-in isograd over a horizontal distance of 10-15 km, ending in the southernmost GHS. The schists show a progressive increase in pressure-temperature conditions from 480°C and peak pressure of 4.8 kbars at the top of the LHS to 715°C and 8.4 kbars in the GHS in the north (Figure 2.3; Mohan et al., 1989; Harris et al., 2004; Dasgupta et al., 2004, 2009; Mottram et al., 2014).

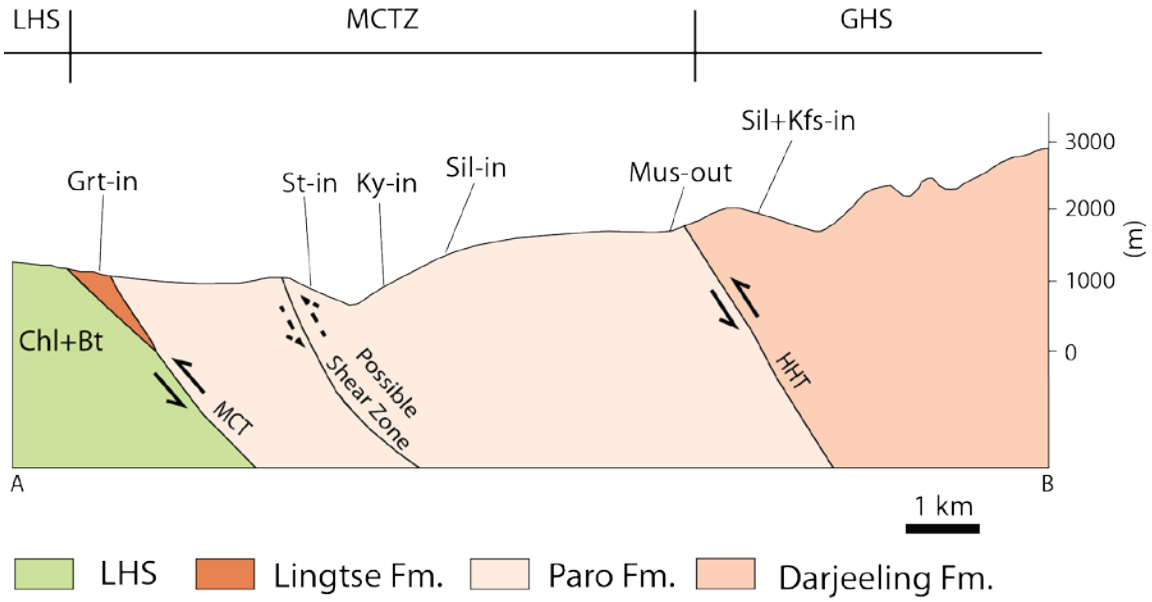

Figure 2.3: Schematic cross-section showing the sequence of metamorphic isograds increasing from lower (LHS) to higher (GHS) structural levels along an E-W profile in central Sikkim (for location, see Figure 2.1). Abbreviations are: Chl - Chlorite, Bt - Biotite, Grt - Garnet, St - Staurolite, Ky - Kyanite, Sil - Sillimanite, Mus - Muscovite. A mineral followed by *-in* signifies that it is the first time the mineral was encountered (the lowest pressure/temperature) along the section; *-out* signifies that the mineral no longer occurs at temperatures/pressures beyond that point. Modified from Dasgupta et al., 2004, sillimanite isograds from Mottram et al., 2014.

Based on pressure-temperature data and compositional zoning of garnets found within migmatites in the footwall of the STDZ, the northern section of the GHS may have experienced peak metamorphic conditions of up to ~10 kbars and 800 °C (Ganguly et al.,

2000). Retrograde mineral reactions within garnet and cordierite combined with thermobarometric Modelling suggest initial rapid exhumation of the GHS at a rate of ~15 mm/yr from a depth of ~34 km to 14.7 km followed by a brief period of heating and rapid cooling to 11.8 km and finally a much slower phase of exhumation at ~2 mm/yr to a depth of ~5 km below the surface. If this rate is extrapolated for the last 5 km of exhumation to the surface, then the GHS would have been exhumed to the surface from a depth of ~34 km over a period of ~8 Ma, corresponding to an average exhumation rate of 4.25 mm/yr (Ganguly et al., 2000).

Leucogranites intruding the GHS and the TSS are found as dykes, sills and plutons up to several kilometres size directly related to the anatexis of the GHS; partial melting due to muscovite dehydration caused differentiation of the GHS resulting in felsic intrusions into the rest of the GHS and overlying TSS (LeFort et al., 1987; Harris and Massey, 1994; Zhang et al., 2004). The ages of these leucogranites has been constrained by U-Th-Pb chronology and trace element analyses on zircons and monazites and suggests that emplacement occurred primarily between 23-22 Ma and 13-12 Ma (e.g., Parrish et al., 1992; Rubatto et al., 2012; Kellett et al., 2013). In Sikkim, the majority of these leucogranites are found in the NW corner of the province, in and around the Kangchenjunga massif (Figure 2.1, Searle and Szulc, 2005).

Several studies used both geo-and thermochronological dating methods to constrain the chronology of tectonic movement on the MCTZ in Sikkim. Catlos et al. (2004) used Th-Pb dating on monazite from GHS samples from the hanging wall of the MCT, and LHS samples from the footwall on the northeastern edge of the Tista Window

(Figure 2.1). The oldest monazites are located in the footwall of the HHT and range in age from 22.0 ± 0.3 to 20.1 ± 0.7 Ma; these results are interpreted as representing the crystallization ages of the monazites formed during the first movement along the MCTZ (Catlos et al., 2004). A younger group of ages ranging from 18.3±0.1 to 12.9±0.2 Ma derived from samples from the footwalls of both the HHT and the MCT are interpreted to represent monazite growth during shearing across the MCTZ and date the onset of ductile deformation along the MCT. Finally, the youngest group of samples from the MCT footwall range from 11.9±0.3 to 10.3±0.2 Ma which suggests that the MCT was active until at least 10 Ma (Catlos et al., 2004).

Garnets from migmatites and granites located in the hanging wall of the MCTZ (Harris et al., 2004) yielded Sm-Nd ages of 16.1 ± 2.4 Ma and 23 ± 2.6 Ma, from rim and core respectively, and are interpreted as representing different periods of garnet growth. Incidentally, the age of the core of the garnet coincides with the onset of activity on the MCT (~20-23 Ma) as determined by Catlos et al. (2004); Harris et al (2004) further suggested that the age of the cores may represent the onset of significant displacement on the MCT, whereas the age of the rims may represent younger movement episodes. From these and other geochronological studies in other parts of the orogen (c.f., Figure 4 in Godin et al., 2006) it is suggested that the MCTZ was active between ~23 Ma and ~10 Ma.

The GHS and the MCTZ were thrust over the LHS along the MCT (Figure 2.2). The convoluted modern trace of the MCT in map view results from differential erosion affecting the GHS nappe which exposes the underlying LHS in the Tista half-window

(Figure 2.1). Away from this peculiar erosional feature both HHT and MCT are parallel to the E-W trend of the major Himalayan structures (Figure 2.1).

2.2.3 - Lesser Himalayan Sequence (LHS) and Ramgarh Thrust (RT)

The LHS exposed in Sikkim consists of three units: the Daling Group, the Buxa Formation and the Gondwana Formation (e.g., Schwan, 1980; Bhattacharrya and Mitra, 2009; Figures 2.1 & 2.2, Table 2.1).

Table 2.1: Summary of the lithologies and stratigraphic thicknesses of the LHS units (Daling, Buxa and Gondwana) in Sikkim. From Mitra et al., 2010.

Units & Age	Lithology	Thickness
Siwaliks (Miocene - Pliocene)	Synorogenic clastic sediments associated with Himalayan thrusting	
Gondwana (Permian)	Coaly shales interbedded with sandstones Massive grey sandstones Conglomeratic sandstones and Rangit pebble slates	~ 1 km
Buxa (Late Proterozoic-Early Cambrian)	Massive, thick-bedded dolomites Cherts and phyllites with dolomite bands Limey shales with thin beds of pink limestone	~ 1.2 km
Daling (Early Proterozoic)	Flysch sequence made up of dirty sandstones/siltstones and mafic-rich pelites (commonly meta-morphosed to dark green phyllites and schists)	~ 5 km

The oldest but structurally highest LHS unit, the Precambrian Daling group, consists of the quartzitic Reyang Formation and the overlying meta-pelitic Daling Formation (Bhattacharrya and Mitra, 2009). The Daling Group has a maximum stratigraphic thickness of approximately 5 km (Bhattacharrya and Mitra, 2009) and is primarily composed of green-grey chloritic slates and phyllites of marine origin (Bhattacharrya and Mitra, 2009; 2011). There are no data available on the age of the

section in Sikkim; however equivalent formations have been dated in both Bhutan and Nepal. U-Pb dates on detrital zircon from the Ranimata and Kushma formations in Nepal, which can be correlated with the Daling and Reyang formations, respectively, suggest a maximum depositional age of ~1.86 to ~1.83 Ga (DeCelles et al., 2001). Dates from the Daling and Shumar Formations, which can be correlated with the Reyang Formation in Bhutan, suggest a maximum depositional age of ~1.8 - 1.9 Ga (McQuarrie et al., 2008; Long et al., 2011).

The Buxa Formation unconformably overlies the Daling Group and is composed of both marine and continental carbonaceous slates and interbedded quartzites, limestones and conglomerates up to 1.2 km thick (Bhattacharrya and Mitra, 2009). The Buxa Formation is interpreted to be Late Precambrian on the basis of marine microfossils found within cherts in the Rangit window (Schopf et al., 2008). U-Pb dates on detrital zircons from the equivalent Baxa Formation in Bhutan, however, suggest a maximum Early Cambrian (520 - 485 Ma) depositional age (McQuarrie et al., 2008; Long et al., 2011).

At the top of the sequence but at the lowest structural level, the Gondwana Formation lies unconformably on the Buxa Formation. It is an up to 1 km thick section of basal conglomerates overlain by sandstones, quartzites, and topped by carbonaceous slates (Bhattacharrya and Mitra, 2009). Plant fossils found within the Gondwana formation suggest a Permian depositional age, with deposition in a subaerial environment (Acharyya, 1971).

The Ramgarh Thrust (RT) is a prominent thrust fault located within the LHS, separating the Daling Group from the Buxa and Gondwana formations (Figures 2.1 and 2.2; Bhattacharrya and Mitra, 2009). It is exposed (1) within the double window at the boundary between the Rangit and Tista windows and (2) to the south along strike of the orogen between the MCT and the MBT (Figure 2.1). The RT is suggested to have been active in western Nepal by ~15 Ma (Pearson and DeCelles, 2005) based on the minimum age of the Dumri Formation, a synorogenic sedimentary unit stratigraphically located above the Gondwana Formation in Nepal, exposed in the footwall of the RT. No absolute or relative timing of activity is available for the RT in Sikkim. During the formation of the Rangit Duplex, the rocks were folded and eroded resulting in the circular pattern now observed at the surface and the shape of the Rangit window (Figure 2.1; Bhattacharrya and Mitra, 2009).

2.2.4 - The Main Boundary Thrust (MBT), the Siwalik Group and the Main Frontal Thrust (MFT)

The LHS is bounded to the south by the MBT, a thrust fault dipping steeply (~50°) towards the NNE (Mukul, 2000) (Figures 2.1 and 2.2). In Bhutan, the MBT is suggested to have been active after about 10 Ma, when displacement associated with ductile deformation on the MCT ceased (Coutand et al., 2014). Similar reasoning applies in Sikkim where the MCTZ became inactive by 12-10 Ma. It is likely that the MBT became active at that time in order to accommodate ongoing convergence (Catlos et al., 2004; Harris et al., 2004).

The Siwalik Group is a sequence of syn-orogenic clastic sediments derived from the erosion of material from structurally higher units (e.g., GHS, LHS), transported and

deposited into the Himalayan foreland basin. The Siwaliks can be subdivided into three lithotectonic units termed the lower, middle and upper Siwaliks, all of alluvial origin (Burbank et al., 1996). The lower unit is predominantly mudstones, the middle unit sandstones, and the upper unit is defined by a large proportion of conglomerates (Najman, 2006). No information is available for the thickness of the Siwaliks in Sikkim, but elsewhere in the Himalaya it ranges from less than 3 km in eastern Bhutan, to over 7.5 km in northwestern India (e.g., Hirschmiller et al., 2013).

The southern boundary of the Siwaliks is the Main Frontal Thrust (MFT), the southernmost thrust fault in the orogenic wedge and the currently active frontal toe of the Himalaya (Lavé and Avouac, 2000; Lavé and Avouac, 2001). The MFT is only discontinuously exposed at the surface (e.g., Figure 2.1) and thrusts the Siwalik Group on top of the modern foreland basin. Mukul et al. (2007) combined optically and thermally stimulated luminescence ages (OSL and TSL) from fault gouge from the MFT and obtained an age of ~40 ka which was interpreted as reflecting ongoing activity on the MFT into the late Pleistocene. In Nepal, Lavé and Avouac (2000) examined offset fluvial terraces and concluded that during the Holocene, the MFT accommodated an average of 21.5 mm/yr of N-S shortening during periodic slip events. Similar geomorphic work on offset fluvial terraces was conducted in Bhutan and yielded an average rate of ~20 mm/yr during the last 2 ka (Berthet et al., 2014).

The MFT, MBT and MCT all branch at depth from the Main Himalayan Thrust (MHT) (Figure 2.2) (e.g., Schelling and Arita, 1991; Nelson et al., 1996), a crustal-scale décollement along which the Himalayan wedge is being thrust on top of the Himalayan

foreland basin and the Indian craton to the south (Figure 2.2). The MHT has been imaged through geophysical surveys (e.g., Zhao et al., 1993; Nelson et al., 1996; Acton et al 2011) and its location and geometry are detailed in section 2.4.

2.3 - The Rangit and Tista Windows and the Lesser Himalayan Duplex System

Among the most striking geological features observed in Sikkim are the two erosional windows which expose the LHS units beneath the GHS (Bhattacharyya and Mitra, 2009; Figures 2.1 and 2.2). The larger Tista half-window is bounded by an irregular circular MCT map pattern (Figure 2.1) within which is exposed the smaller full Rangit window which is delimited by the folded RT (Figure 2.2). The Rangit and the Tista rivers, which flow through the center of their respectively named windows (Figure 2.1), have likely played a significant role in incising and exposing the LHS units (Bhattacharyya and Mitra, 2009).

Structural and stratigraphic analysis suggests that the LHS units are structurally repeated, forming a system of imbricated duplexes which have been eroded resulting in the windows on the surface (Bhattacharrya and Mitra, 2009; Mitra et al., 2010) (Figures 2.1 & 2.2). Figure 2.4 outlines the major components of a duplex.

The Daling duplex, bounded to the north by the MCT (Figure 2.2) is interpreted to contain up to four horses of the Daling group rocks. The roof thrust (the upper bounding thrust) of the Daling duplex system is the RT, which is soled by the MHT (Figure 2.2). The horses dip towards the north at an angle of ~ 30° (Bhattacharrya and Mitra, 2009; Figure 2.2). In the Rangit duplex further south, four horses are stacked in a similar orientation to those observed in the north, but involve the repetition of all three LHS units (Daling,

Buxa and Gondwana) (Figures 2.2 & 2.5). In the central part of the Rangit Duplex, several LHS slices have been stacked, creating a double antiformal stack. Gravity (Bouguer anomaly) Modelling suggests a total thickness of up to 12 km of stacked LHS units in central Sikkim, thinning both to the east and west (Tiwari et al., 2006). Finally, south of the antiformal stacks, there are several small imbricates that have been translated over the top/roof of the stacks and now dip to the south (Figure 2.5).

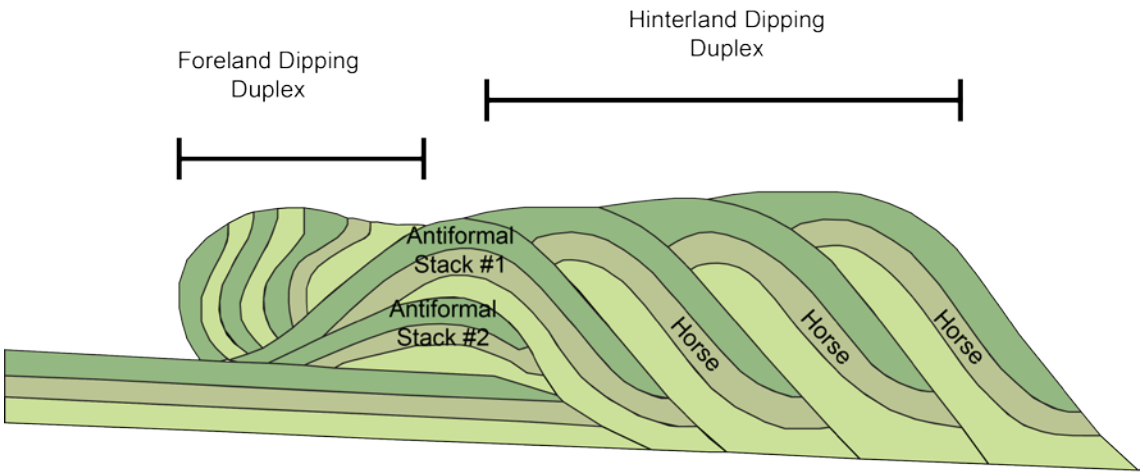

Figure 2.4: Schematic diagram showing the Rangit duplex. Duplexes consist of a series of fault-bounded crustal imbricates that contain repeated geological units. Each fault-bounded repetition is termed a horse. Multiple horses stacked up against/on top of one another constitute a duplex; where the horses stack vertically in a convex up way they are known as antiformal stacks. Modified from Bhattacharyya and Mitra, 2009.

According to the sequence of duplex evolution presented in Bhattacharrya and Mitra (2009), the oldest, and now southernmost, imbricate slices were progressively stacked against each other towards the foreland. During that early stage, a section of the RT (labeled RT 1), became disconnected from the main roof thrust and was deactivated (Figure 2.5 a-c). New crustal slices continued to be accreted through underplating, as splays from the MHT basal thrust (Figure 2.5 d-h).

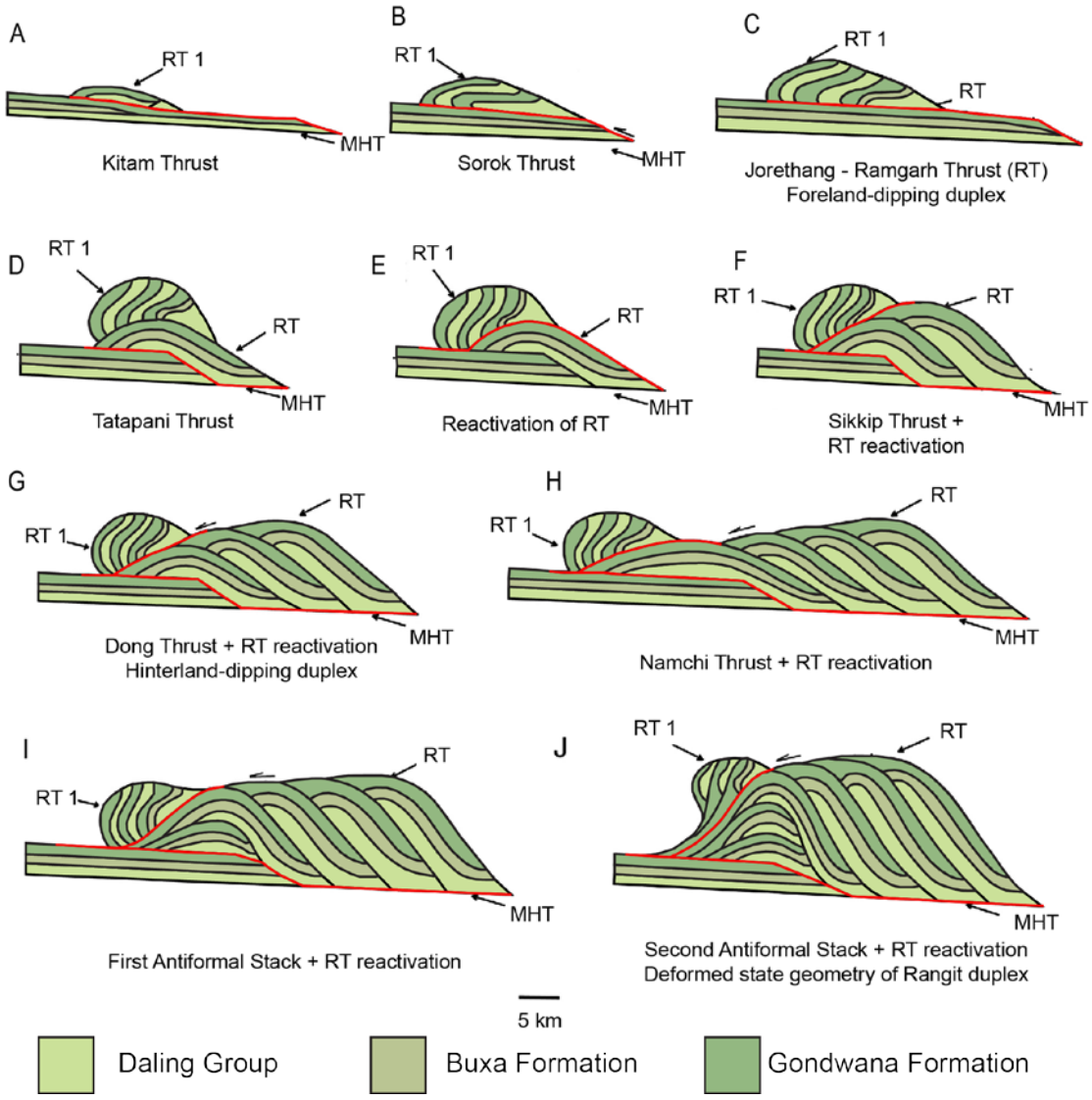

Figure 2.5: Interpretative reconstruction of the formation of the Rangit Duplex. Each panel corresponds to a time-step (A-J) at which a particular thrust within the duplex was active. The active thrust at each time-step, as well as the re-activated RT, is/are highlighted in red on the different figures. The roof thrust of the duplex is either the RT or the older RT 1, a deactivated section of the RT forming the roof thrust of the foreland ward dipping duplex section. The basal thrust in all cases is the MHT. North is to the right. From Bhattacharyya and Mitra, 2009.

Concurrently, as the younger horses were being emplaced through motion along the MHT, the roof thrust (the Ramgarh Thrust) was also translated south carrying the earliest three horses formed (Figure 2.5 a-b) over the top of the duplex package to

become the current foreland dipping horses (Figure 2.5 e-j). Finally, horses began to stack vertically beneath growing antiformal stacks and rotating the foreland-dipping duplex to its current position (Figure 2.5 i-j). According to this interpreted reconstruction, the antiformal stacks are located above a ramp in the MHT (Figures 2.2 & 2.5). At a crustal ramp, the trajectory of material advected by a fault has a larger vertical component, which equates to a local increase in rock uplift rates above the ramp.

South of the Rangit duplex, remnants of GHS preserved in the Darjeeling klippe (Figure 2.1) suggest that the GHS nappe once extended further south than its current surface trace, and was eroded, exposing the underlying LHS (Figures 1.1 and 2.1) (Bhattacharrya and Mitra, 2009).

2.4 – Geophysical Data

Several geophysical studies have found evidence of a discontinuity at depth that corresponds to the location of the MHT. Using deep reflection seismic data, Project International Deep Profiling of Tibet and the Himalaya (INDEPTH) (Alsdorf et al., 1998a; Alsdorf et al., 1998b; Hauck et al., 1998; Makovsky et al., 1996; Nelson et al., 1996; Zhao et al., 1993) imaged a strong reflector beneath the Tethyan Himalaya that is interpreted to be the MHT underneath northern Sikkim and southern Tibet (e.g., Zhao et al., 1993; Nelson et al., 1996 Hauck et al., 1998; Figure 2.6). The reflection data show a discrete structure, first imaged just south of the STDZ at ~28 km depth (Figures 2.7 & 2.8) and dipping gently (average dip ~9°) to the north in northern Sikkim and into Tibet. The structure dips sharply below the southern limb of the Kangmar dome (~28°45’N)

beneath the Tethyan Himalaya, to a depth of ~50 km under southern Tibet where it disappears from the profile (Nelson et al., 1996; Figure 2.8).

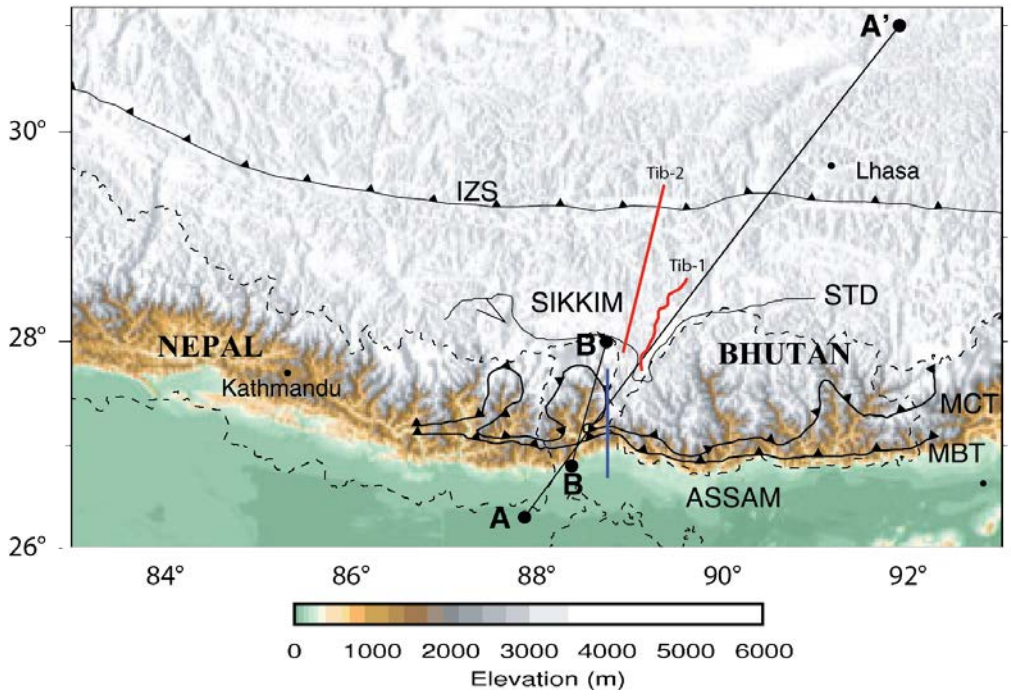

Figure 2.6: Location of receiver function profiles A-A' and B-B' from Acton et al., 2011 (shown in black) as well as the locations of profiles Tib-1 and Tib-2 from the INDEPTH survey (shown in red; e.g., Hauck et al., 1998) and profile T2 (in blue) showing the location of the earthquake hypocenter cross-section shown in Figure 2.9 (De and Kayal, 2003). Modified after Acton et al., 2011.

In Sikkim, Acton et al. (2011) used receiver function data, combined with INDEPTH reflection data (Hauck et al., 1998) to image the structures at depth and reported a distinct Low Velocity Zone (LVZ) beneath the Darjeeling-Sikkim Himalaya (Figures 2.6 & 2.7) which they interpreted to be the MHT. The trace of the LVZ was imaged at a depth of 10 - 15 km as a nearly flat feature beneath the lesser Himalaya from 90 - 150 km along the A-A' profile (SW-NE across Sikkim; Figures 2.6 & 2.7), 10 - 70 km north of the MBT. The LVZ then begins to dip (~20 - 30 °) northwards before disappearing entirely at ~260 km along their profile, corresponding to a distance of ~160

km north of the MBT, at a depth of ~ 35 km (Figure 2.7). The connection between the MHT imaged by Acton et al. (2011) and the frontal structures of the wedge (MBT and MFT) remains unconstrained (Figure 2.7). Their second profile B-B' (Figure 2.6), imaged structures at similar locations and depths.

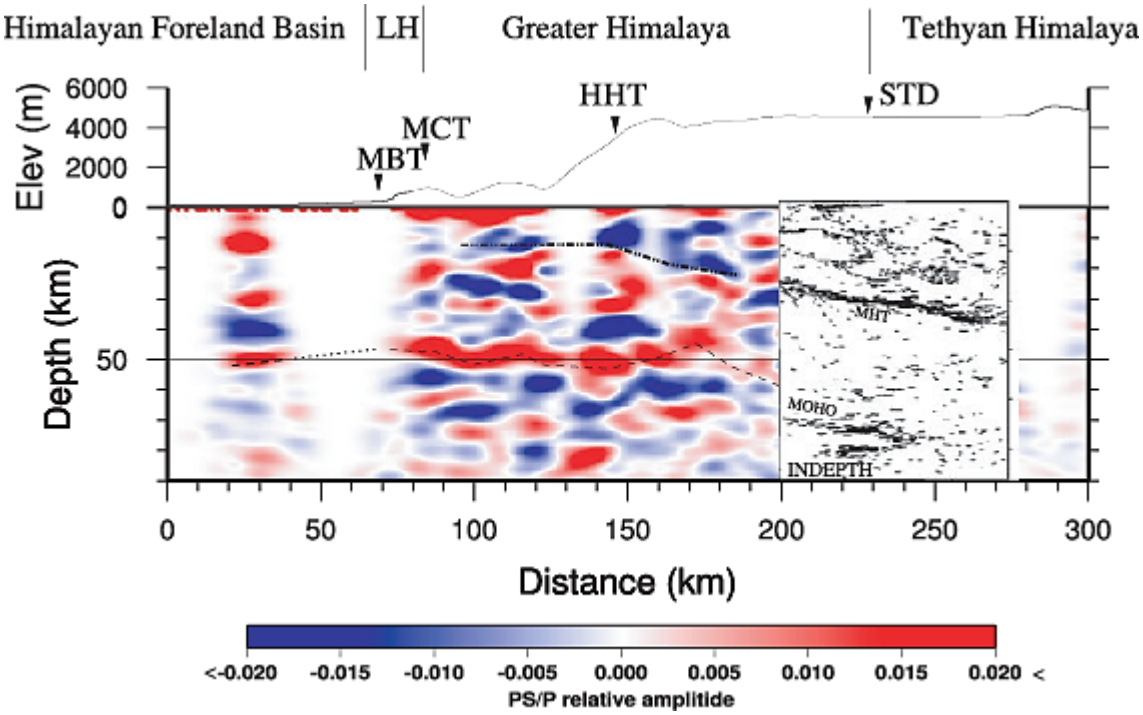

Figure 2.7: Results of a receiver function survey through the Sikkim Himalaya along the profile A-A' shown in Figure 2.6, combined with INDEPTH data for the northern part of the transect. A Low Velocity Zone (blue) starting at ~10 km depth has been interpreted to represent the trace of the basal MHT. A high velocity zone (red) is also seen at ~50 km depth and likely represents the Moho. Discrete velocity zones (either high or low) generally represent either a geologic contact or other abrupt change in rock properties. The flat MHT begins to dip northwards beneath the HHT and continues to do so until the signal is lost. Interpretations of seismic reflection data from the INDEPTH survey (Hauck et al., 1998) show both the MHT and the Moho underneath southern Tibet and provide a reliable continuation of Acton et al's interpretations. From Acton et al., 2011.

Both INDEPTH and Acton et al. (2011) data also imaged the Moho along the same profiles. Acton et al. (2011) reported the depth of the Moho to be 44 - 48 km under the

foothills of the Sikkim Himalaya (Figures 2.3 & 2.7). Under the Darjeeling-Sikkim Himalaya the Moho dips generally northwards but also exhibits secondary topography, appearing to flex upwards under the MCTZ before descending rapidly beneath the GHS, disappearing at a depth of ~58 km (Figure 2.7). INDEPTH imaged the Moho at depths of 70 - 80 km underneath Tibet (e.g., Nelson et al., 1996; Figure 2.8), as a generally flat structure along most of the INDEPTH profiles.

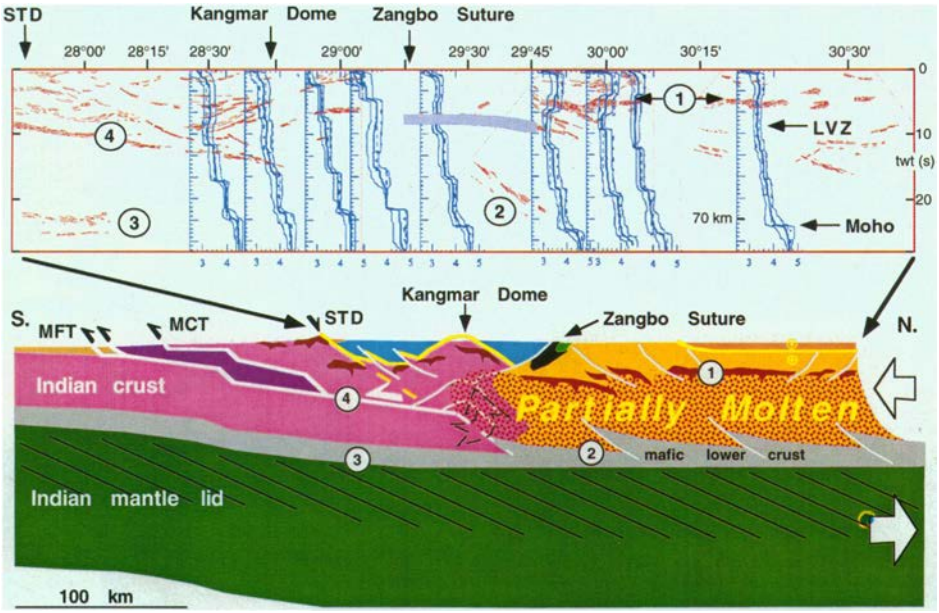

Figure 2.8: Composite results of INDEPTH reflection profiles extending from 27°43' to the 30°35'. The Figure highlights reflections (two way travel-time plotted against latitude) of the MHT (4) and the Moho (3) in southern Tibet. The profile is inset into the cross-section below it showing the interpreted location and geometry of the MHT and Moho. From Nelson et al., 1996.

2.4.1 - Seismicity and GPS data

Seismic data show activity clustered around the MBT within the study area. De and Kayal (2003) compiled hypocenters for modern earthquakes produced by thrusting along a N-S transect in the Sikkim Himalaya and produced a cross-section to compare to the location of major structures (Figures 2.6 & 2.9). They found that most of active

seismicity is confined to a zone located between the MBT and the MCT and are produced by a thrust mechanism, leading them to conclude that the MCT is inactive and the MBT is the currently active structure (Figure 2.9). The depths of these earthquakes, which are continuous from the surface down to 45 km, have led these authors to suggest that the MBT may cross-cut the MHT and extend below it into the lower crust. Other geophysical evidence, however, does not support this interpretation.

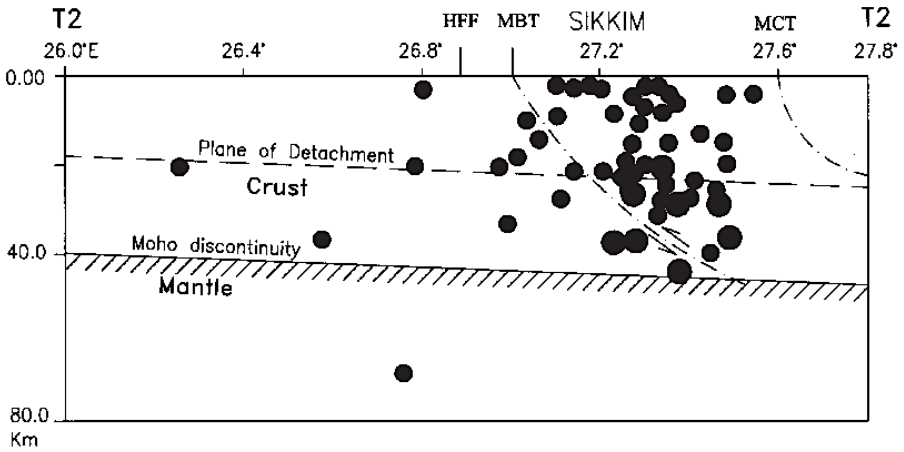

Figure 2.9: North-south section across Sikkim (at ~88.6 °E) showing the depths of the epicenters of major modern earthquakes of magnitude > 3.5 (black circles) with respect to the location of major structures (from De and Kayal, 2003). Epicenters located 30 km on either side of the profile were included. The acronym HFF (Himalayan Frontal Fault) on this Figure corresponds to the MFT

Jade (2004) used GPS measurements and found that the modern convergence rate in Sikkim, in the reference frame of a fixed Indian plate, is ~10 - 20 ± 1 - 3 mm/yr in a NE direction of 44 °. Mukul et al. (2009; 2010) used GPS data to calculate the convergence rate of an area of the Gangetic Plains south of Sikkim, relative to Tibet (fixed to the Lhasa block), at ~12 - 13 mm/yr (Figure 2.10). When they converted this value to an arc-perpendicular orientation, they estimated a relative convergence rate of

~16 mm/yr; however, they noted that this arc-perpendicular value is not directly validated by GPS measurements (i.e. the rate was extrapolated and not directly measured).

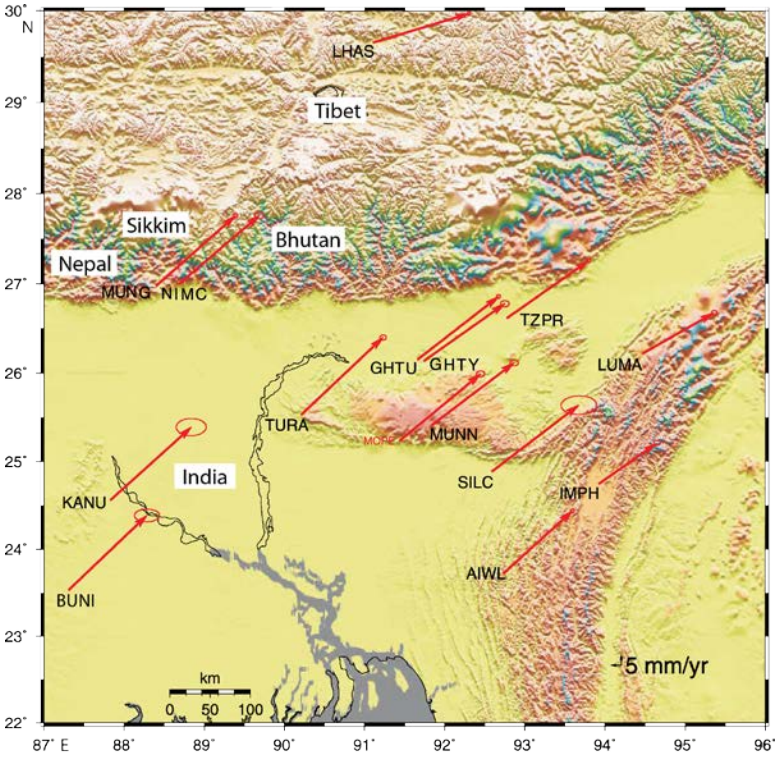

Figure 2.10: Map of northern India, the eastern Himalaya and Tibet showing GPS velocity vectors in the ITRF (International Terrestrial Reference Frame) 2000 frame of reference. Red arrows show velocity vectors from each GPS ground station. From Mukul et al., 2010.

Studies involving thermokinematic models elsewhere in the Himalaya, similar to models constructed for this thesis, have assumed convergence rates of 20 - 25 mm/yr both in Nepal (e.g., Whipp et al., 2007; Herman et al., 2010; Robert et al., 2011) and in Bhutan (Robert et al., 2011; Coutand et al., 2014) based on GPS displacement measurements along the Himalayan arc (Bilham et al., 1997; Larson et al., 1999; Wanget al., 2001; Jouanne et al., 2004; Bettinelli et al., 2006; Banerjee et al., 2008).

2.5 – Topographic Data

Topographically, Nepal and Sikkim are similar while Bhutan displays a different topographic profile. Robert et al. (2011) constructed topographic profiles (Figures 2.11 & 2.12) along swaths in both Nepal and Bhutan.

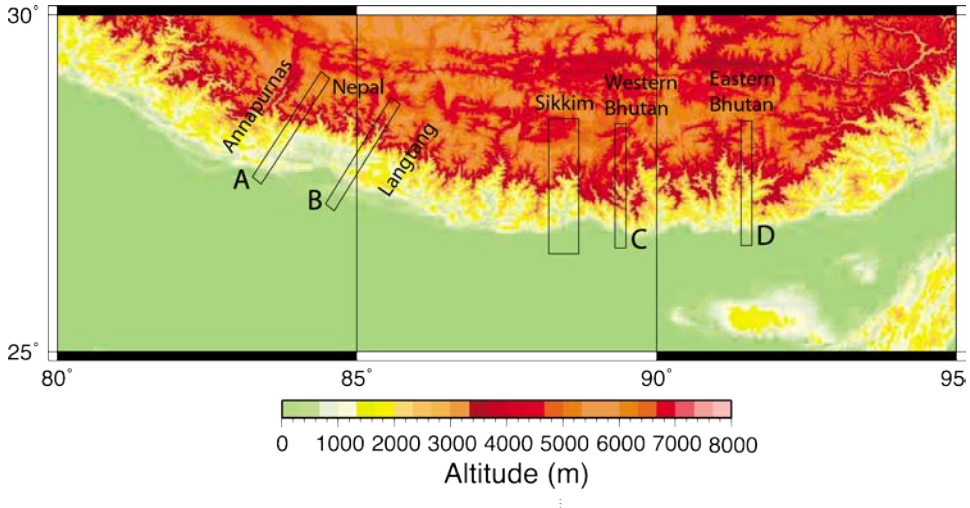

Figure 2.11: Topographic map of Nepal, Sikkim and Bhutan showing the location of four 20 km wide topographic profiles, from Robert et al., 2011, shown in Figure 2.12 and a 50 km wide topographic profile constructed for Sikkim shown in Figure 2.13. Topographic data are from SRTM-90 m (Shuttle Radar Topography Mission). Figure modified from Robert et al., 2011.

In Nepal, the mean elevation profile of the orogenic front is characterized by a two-step morphology, whereas in Bhutan the profile is relatively straight showing a nearly constant, gradual gain in elevation from the foreland to the plateau (Duncan et al., 2003; Robert et al., 2011; Figure 2.12). Mean elevation increases gradually from the foreland from <100 m to ~1000-1500 m for ~30-40 km along the profiles. Beyond that the profile flattens and slowly gains elevation until 80-100 km where elevation increases rapidly into the GHS in the higher Himalaya and finally flattens again toward the Tibetan Plateau at 4000-5000 m (Figure 2.12 A & B). Duncan et al (2003) showed that in Nepal,

areas with high topography and significant relief correlate with the surface exposure of the GHS thrust sheet. In Nepal, the GHS is exposed in two bands: one ~20 km wide band in northern Nepal at approximately 120-140 km along the profile (Figure 2.12 A & B) and a narrower ~10 km wide band to the south that coincides with a southern zone of moderate relief at ~30-40 km (2.12 B).

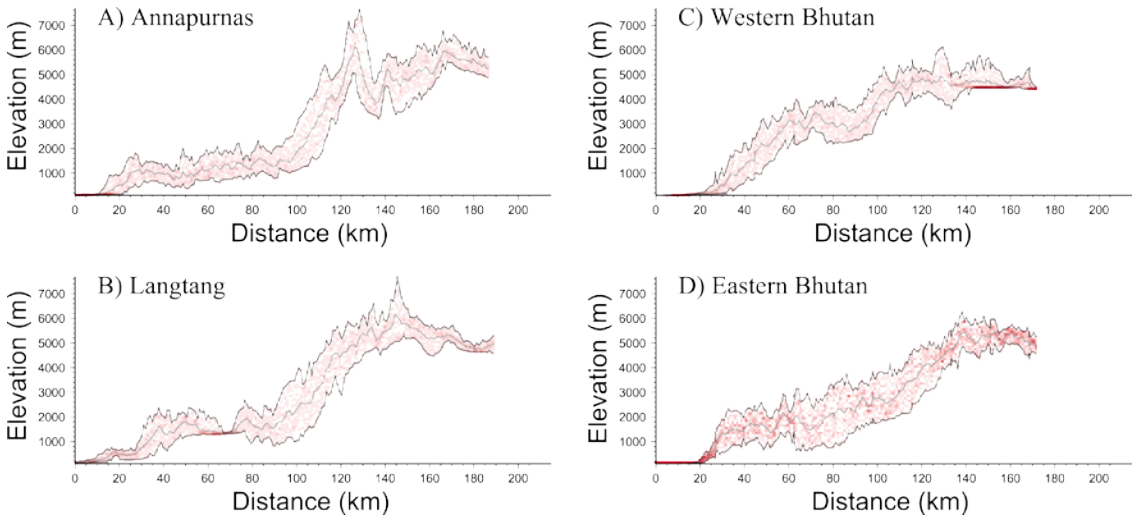

Figure 2.12: Four topographic profiles showing the minimum and maximum elevations (upper and lower boundaries) and 20 km width average elevation (central dark line) from the foreland to the high Himalaya in Nepal ((A) Annapurna and (B) Langtang) and (C) Western and (D) Eastern Bhutan. The red dotted fill corresponds to the probability density for the most likely elevations within the 20 km swaths. From Robert et al., 2011.

The elevation trends in the northern regions show a clear concave-up profile. In contrast, the profiles for both eastern and western Bhutan show a relatively straight profile with continually increasing elevation from the foreland to the plateau (Figure 2.12 C & D) especially in eastern Bhutan. In western Bhutan there appears to be a small break in slope between 80 and 90 km, this has been interpreted to be evidence of relict landscape from a previous topography that has yet to be eroded away; knickpoints within this relict topography suggests that it was formed in the past at a lower elevation

and was then subsequently uplifted to its current position (Duncan et al., 2003; Grujic et al., 2006). Bhutan profiles appear somewhat concave-up in the west and nearly straight in the east, suggesting a more consistent gradual increase in elevation compared to the sharp topographic break observed in Nepal. In addition, the GHS in Bhutan extends further south and is composed of a much larger contiguous package, unbroken by windows of LHS, compared to the two major bands of GHS in Nepal. The Bhutan range shows a more consistent pattern of higher relief which correlates well with the location of the GHS (Duncan et al., 2003).

In Sikkim (Figure 2.13), the DEM shows very clearly that the Rangit and Tista windows coincide with low elevations flanking the major valleys of the Rangit and Tista rivers. Elevations above 4 km appear to correlate generally with the boundaries of the Tista window and the exposure of the GHS. The swath profile (Figure 2.14) indicates that Sikkim also shows a poorly defined two-step north-south topographic profile with isolated patches of high relief. Average elevation increases slowly from the foreland to a first peak at ~27 °N and an elevation of ~1200-1300 m, and then declines in the area of the Rangit Window into a slight ~ 100 m depression. Towards the northern edge of the Tista Window, average elevation increases steadily up into the GHS to ~3000 m. Another decrease in average elevation appears just to the north of the Tista Window, where the Tista River is fed by two smaller rivers with valleys oriented in an east-west direction (Figure 2.13). Then, elevation continues to increase steadily northward to an average elevation of 5000-6000 m.

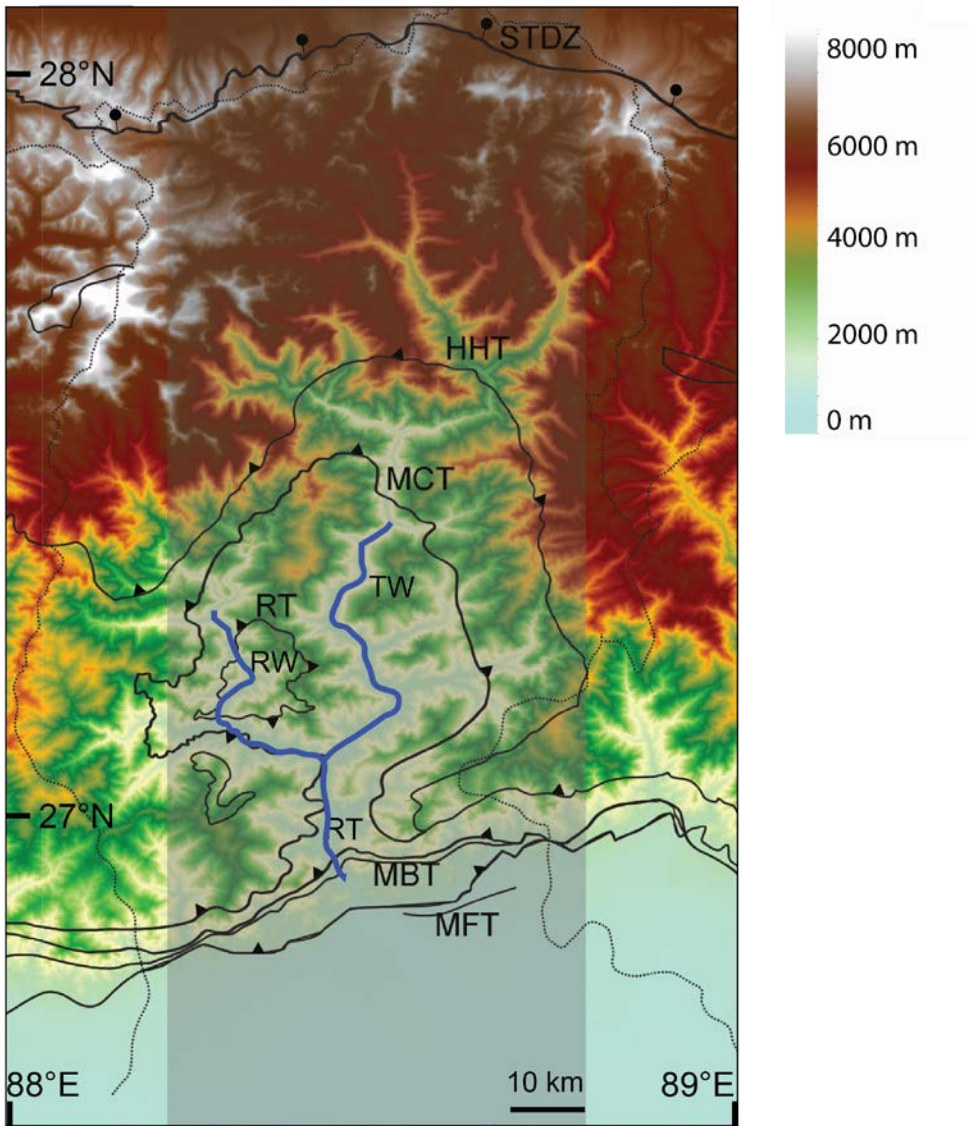

Figure 2.13: Digital Elevation Model of Sikkim between 26.5 °N - 28 °N and 88 °E - 89 °E constructed from SRTM (Shuttle Radar Topography Mission) 90 m data (http://srtm.csi.cgiar.org/). Structures are from Grujic et al., 2011 (same legend and abbreviations as in Figure 2.1). The shade grey rectangle shows the locations of a 50 km wide swath profile where elevation data were extracted and are presented in Figure 2.14. Blue lines indicate the location of the Rangit and Tista rivers.

The minimum elevation curve shows a clear topographic break between 27.5 - 27.6 °N which is the approximate location of the northern boundary of the Tista Window

and the first appearance of the GHS. The overall topographic pattern of Sikkim seems to be similar to the two-step morphology observed in Nepal.

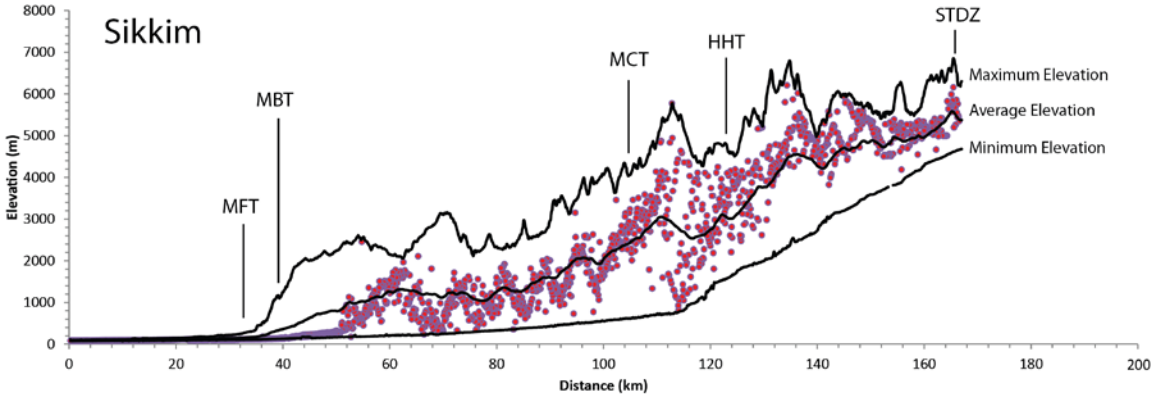

Figure 2.14: A swath profile constructed along the profile indicated in Figure 2.10. Average elevation (center), maximum elevation (top) and minimum elevation (bottom) over the 50 km wide zone are plotted against distance north along the profile shown in Figure 2.11 at a ~93 m DEM sample interval. Red dots show the most common elevation at each point along the profile. Constructed from SRTM (Shuttle Radar Topography Mission) 90 m data (http://srtm.csi.cgiar.org/).

Chapter 3 - Thermochronology Methods and Results

3.1 - Introduction

To quantify late Tertiary upper crustal exhumation rates and constrain the processes driving them along the Himalayan range front in Sikkim (India), a multidisciplinary approach is used involving: 1) (U-Th)/He thermochronology on zircon (e.g., Reiners, 2005), and 2) three-dimensional, forward and inverse thermokinematic modelling using the software *Pecube* (Braun, 2003; Braun et al., 2012).

Eighteen *in situ* bedrock samples were collected along a NW-SE transect across the main Himalayan structures, perpendicular to the range front and across the Rangit window (Figure 3.1; see Appendix A for sample details). Zircons extracted from these samples were analyzed using the (U-Th)/He method to produce single-grain cooling ages. These cooling ages were then used as input, along with other thermal and material properties and kinematic parameters, to construct forward and inverse models in order to test different tectonic hypotheses and define a tectonic model that is the most compatible with the data. This chapter will describe the (U-Th/He) methodology and the cooling ages that were obtained from the samples. The model is described in Chapter 4.

3.2 - Zircon (U-Th)/He Thermochronology: Principles of the Method

Thermochronology is used to constrain the thermal histories of crustal rocks. Many thermochronological methods (such as U-Th/He and $^{40}Ar/^{39}Ar$) are based on the radioactive decay of different parent radioisotopes into daughter products at predictable rates. The daughter products are retained within a given mineral when it has

cooled below an effective closure temperature specific to a thermochronometer (e.g., Reiners and Brandon, 2006).

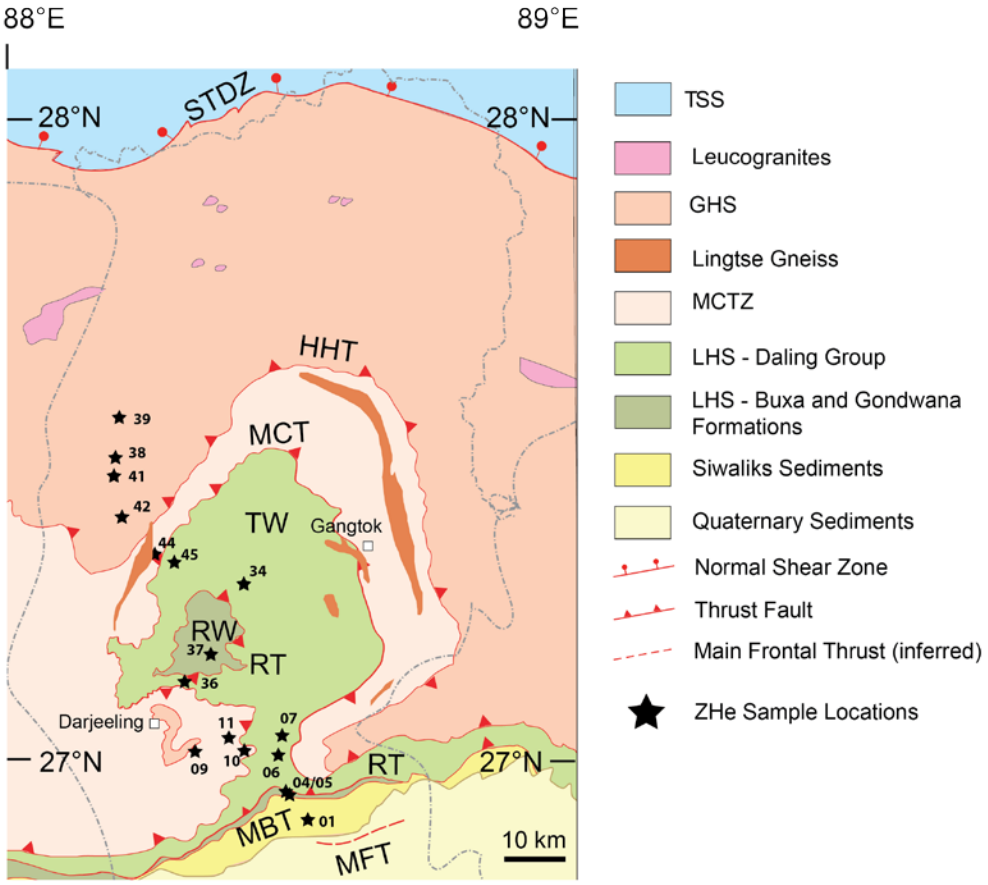

Figure 3.1: Geologic map of Sikkim showing the geographical and geological location of the samples (ISIK-08-##). Modified from Grujic et al, 2011.

The (U-Th)/He dating method is based on the radiogenic decay of ^{238}U, ^{235}U and ^{232}Th and production and retention of α-particles (^{4}He) within a mineral. The amount of daughter product increases predictably with time, as a function of the half-lives of the various parent isotopes (Strutt, 1908). The ratio of daughter products retained within a crystal is based on thermally-controlled diffusion properties specific to the mineral in question (e.g., Reiners, 2005). The final ratio of parent to daughter isotopes is used to calculate single-grain cooling ages that provide information about the cooling history of

a mineral. Because they contain U and Th, zircon and apatite crystals are commonly used in the (U-Th)/He technique (ZHe and AHe, respectively; Farley, 2002).

3.2.1 - Thermochronology

(U-Th)/He thermochronology is primarily used to constrain the thermal histories of rocks residing in the upper crust by extracting cooling ages from certain minerals (e.g., apatite, zircon). Cooling ages represent the amount of time taken for a rock particle to cool from its closure temperature along its exhumation pathway to the surface (Reiners, 2005). These cooling ages can be used, along with known or hypothesized thermal and kinematic properties of the crust such as the radiogenic heat production rate and the slip rate along faults, as constraints for reconstructing the time-temperature path of a sample using thermo-kinematic Modelling.

In contractional settings, material in the hanging wall of a thrust fault is uplifted on top of the footwall, generating stacks of crustal material (Figure 3.2; Stüwe and Barr, 1998). In order for any point in the thrust sheet to be exposed at the surface (and become exhumed), erosion needs to remove the overlying material. The vertical component of the particle path to the surface is known as exhumation. England and Molnar (1990) defined the rate of crustal exhumation as being equal to the rate of surface uplift subtracted from the rate of vertical rock uplift. In an orogenic setting where thrust faulting is the primary tectonic control on the transport of crustal material, the rate of exhumation is effectively equal to the rate of erosion.

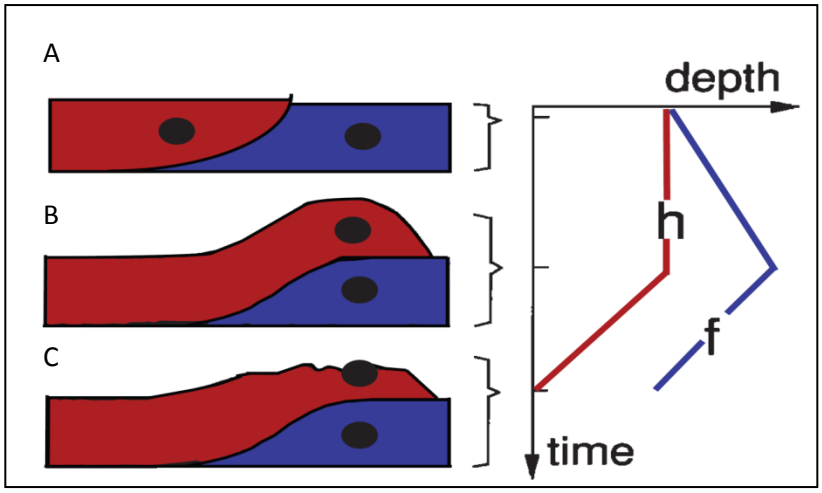

Figure 3.2: Particle trajectory during thrust-faulting shown in 3 stages. A) Initially, two points (black circles) in the hanging wall (h) and footwall (f) of a thrust fault are at the same depth. B) The hanging wall is then thrust on top of the footwall, burying the point in the footwall. The hanging wall sample has been uplifted, with respect to a fixed reference (geoid or sea-level) but not exhumed since the point is no closer to the surface (rock uplift is equal to surface uplift). C) Exhumation of both points occurs where the surface is eroded thereby exposing the rocks beneath (rock uplift is zero but the surface lowered). The chart to the left shows the depth of the two points over the 3 stages. Modified from Stüwe and Barr, 1998.

To quantify Neogene upper crustal exhumation across the study area, 18 samples were collected along a NW-SE transect across the Rangit and Tista windows defined by the Main Central Thrust (MCT) in Sikkim, India (Figure 3.1). The largest group of samples (eight of them) were from LHS rocks. Seven of them are located within the Tista window and the final one is located to the south, just north of the MBT. Four samples were collected within the MCTZ; one located north of the windows and the other three located below the south-western edge of the windows, near the Darjeeling klippen. Four samples were located within the GHS, all at the northern end of the transect. The final two samples were located within the Siwaliks south of the MBT. Zircon crystals, which are abundant in the GHS and LHS units, were extracted from bedrock samples using

generic mineral separation procedures (described below) and processed for the (U-Th)/He method to produce ZHe cooling ages. The following sections outline the methodology for the ZHe dating system.

3.2.2 - Isotopic Decay and Effective Closure Temperature

In the (U-Th)/He system, the parent isotopes (^{238}U, ^{235}U and ^{232}Th) undergo α-decay producing among other intermediate radioisotopes, α-particles, which are stable ^{4}He nuclides (Reiners, 2005). Radiogenically produced ^{4}He diffuses within and outside the crystal lattice as a function of the diffusivity properties of the mineral and its temperature history (Reiners and Brandon, 2006).

The closure temperature (T_c) is the temperature at the time corresponding to the apparent age of the system (e.g. a mineral) (Dodson, 1973). At this temperature the crystal lattice of a particular mineral closes to the loss of parent and daughter isotopes by thermally activated diffusion (Braun et al., 2006). T_c of a particular mineral system can be approximated using the Dodson equation (1973):

$$T_c = \frac{R}{\left\{E_a \times ln\left(\frac{A\tau D_0}{a^2}\right)\right\}} \qquad \text{(Eq. 3.1)}$$

where E_a is the activation energy of the daughter product within the mineral (J/mol), a is the size of the diffusion domain (cm), A is a dimensionless constant based on the geometries and decay constants associated with the mineral (ranging from 55 for a sphere to 8.7 for a plane sheet), D_0 is a frequency factor of thermally activated diffusion (cm^2/s), R is the ideal gas constant (~8.314 J/(K*mol)), and τ is a time constant (s) that is related to the cooling rate of the sample.

Using equation 3.1, Reiners et al. (2004) calculated the effective closure temperature of the ZHe system to range between 171 °C – 196 °C, with an average of 183 °C, at a constant cooling rate of 10°C/Ma and a diffusion domain size of 60 μm. Although the above equation yields a single solution for T_c, known as the effective closure temperature, in reality the closure of a crystal lattice to the diffusion of ^{4}He occurs over a range of temperatures known as the helium Partial Retention Zone (HePRZ) (Wolf et al., 1998).

3.2.3 - The Helium Partial Retention Zone

At temperatures higher than the effective closure temperature, ^{4}He is able to diffuse completely outside the crystal lattice of a mineral and be lost to the environment. Within the HePRZ, the ^{4}He is only partially retained within the crystal lattice, the degree of retention depending on the temperature; once the mineral cools below the HePRZ, most of the ^{4}He produced is retained (Reiners and Brandon, 2006). The upper and lower boundaries of the HePRZ correspond to the temperatures at which 10% and 90%, respectively, of ^{4}He is retained within the crystal lattice (Figure 3.3). These temperatures depend on the holding time of the mineral, which depends on the cooling rate and the size of the diffusion domain, which scales with grain size (Reiners and Brandon, 2006). The amount of time a sample may have spent within the HePRZ needs to be taken into account when interpreting cooling ages.

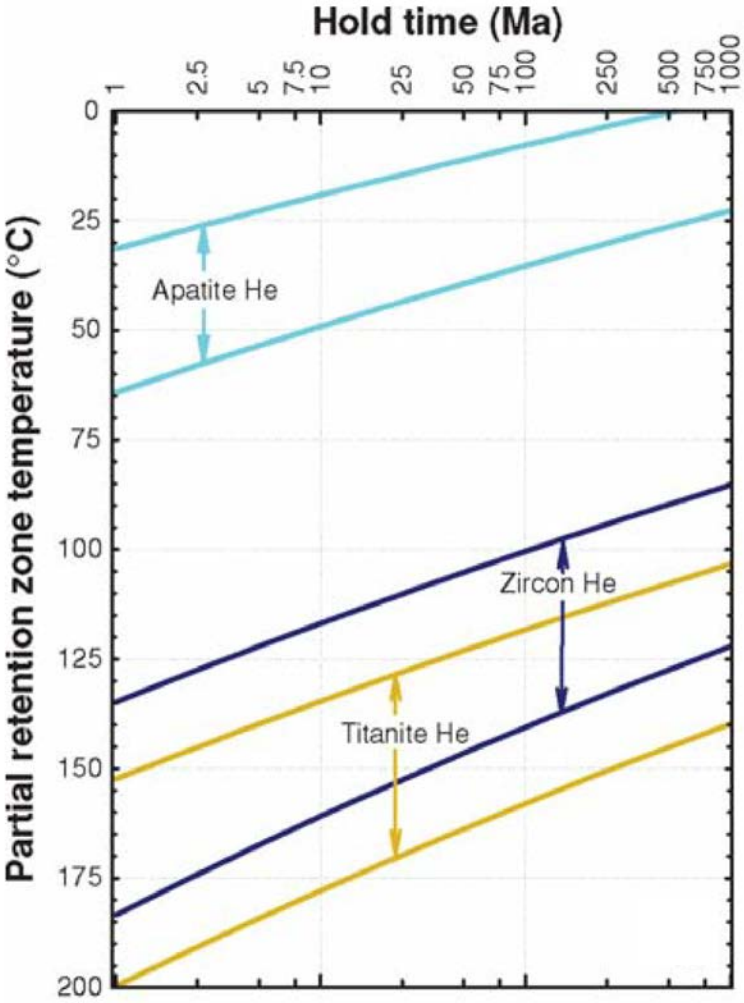

Figure 3.3: Temperature range of the HePRZ for the apatite, zircon and titanite (U-Th)/He systems based on the length of cooling time (or hold time). The slower the samples cool, the lower the closure (and PRZ) temperatures are. From Reiners and Brandon, 2006.

3.3 - Analytical procedure

The ZHe analytical procedure can be broken down into three major steps: 1) crystal isolation, 2) grain selection, measurement and packing, 3) isotope extraction and measurement. Each of these steps is described below.

3.3.1 - Crystal Isolation

The rock samples were each processed through a jaw crusher and then a disk mill to a grain size of < 425 μm. The fractions were then taken to the Wilfley table where a first relative density-based separation was done. The densest fractions containing the mineral of interest were then immersed in sodium polytungstate (SPT), a heavy liquid with a density of ~2.8 g/cm^3, in order to separate the heavier minerals, such as zircon (ρ~4.6 g/cm^3) and apatite (ρ~3.2 g/cm^3), from lighter constituents such as quartz and feldspars (ρ≤2.7 g/cm^3). The SPT heavy fractions were then processed through a Frantz magnetic separator in order to remove magnetically susceptible minerals such as metallic oxides and some micas (e.g., biotite). The final step involved immersion in a second heavy liquid, diiodomethane (MI, ρ~3.2 g/cm^3) in order to separate out minerals such as apatite and concentrate the zircons. The heavy fractions were then inspected under a stereoscopic microscope in order to select the zircons suitable for (U-Th)/He dating.

3.3.2 - Grain Selection

Zircon grains were selected on the basis of size and crystal geometry with a preference for grains that were large (see specifics below), euhedral, and free of mineral inclusions (Reiners, 2005). Grain selection is a critical step in (U-Th)/He dating as the size and geometry of the grains are directly related to the magnitude of the α-particle ejection correction, explained below in section 3.5.2. Grains were examined using a transmitted light stereoscopic microscope at magnification of x106 under both plane-polarized light, for general selection, and cross-polarized light, for identification of

inclusions and/or fractures. Inclusions are undesirable as they may be composed of solid radiogenic minerals that may contaminate the main crystal and bias the final ZHe cooling age. Fluid inclusions are also undesirable as they represent areas contained within the volume of the crystal that likely do not produce alpha particles (if the fluid is water). Fractures are undesirable as they may have acted as escape pathways for helium during cooling of the host crystal, and it is difficult to determine when a particular fracture was created. Generally, the zircon grains selected for this study range from ~65-150 µm in width (e.g., Figure 3.4). Larger grains tended to be less euhedral (rectangular prisms with two pyramidal terminations) or contained more inclusions, whereas smaller grains would require very large α-corrections. Euhedral zircons were preferentially selected as they allow a more accurate α-correction (e.g., Reiners, 2005). For each sample analyzed (18 in total) five acceptable grains were selected for dating, except for one sample where only three suitable grains were found. A total of 88 aliquots were dated in this study.

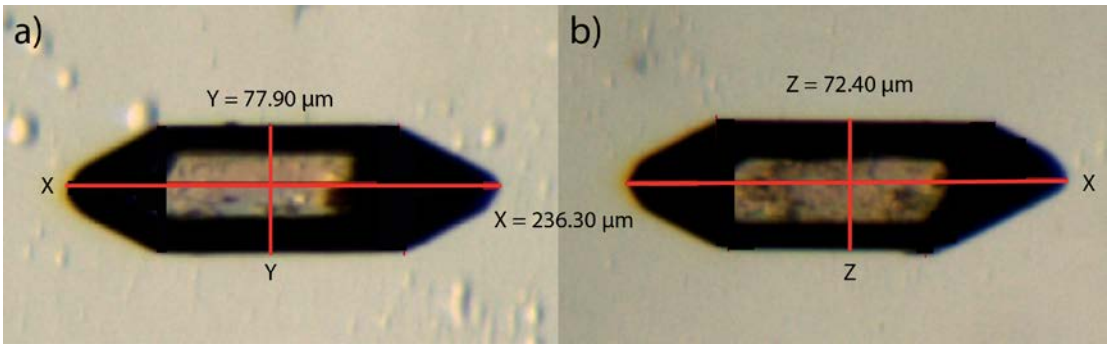

Figure 3.4: Grain ISIK-08-38-1, a euhedral zircon typical in dimensions of the grains that were selected. Each grain is photographed twice: first to measure the two longest axes, X and Y in photo a) and a second time, rotated 90 degrees along the x-axis, in order to measure the 3rd axis, Z in photo b). The lengths of the pyramidal terminations were also measured.

Each zircon crystal was photographed and measured before being wrapped in a 1 mm x 1 mm piece of platinum (Pt) foil. The measurements allow calculation of the volume and surface area of each crystal, which are required to correct for loss of α-particles due to crystal geometry. The Pt foil shields the grain from direct laser contact and prevents shattering and/or uneven heating during ^{4}He extraction.

3.4 - Isotope Extraction and Measurement

Extraction of parent and daughter isotopes was completed in two separate phases, 1) non-destructive extraction of ^{4}He at the Dalhousie Noble Gas Extraction Laboratory and the Keck Isotope Laboratory at the University of California Santa Cruz (UCSC) and 2) destructive ^{238}U, ^{235}U and ^{232}Th measurement at UCSC.

3.4.1 - Laser Extraction and Measurement of Helium

^{4}He extraction was completed for two sets of grains. The first set of 25 grains (corresponding to five samples) was analyzed at Dalhousie while the remaining samples were analyzed at UCSC due to time constraints. The samples, enclosed within Pt foil and placed on a small planchet within a vacuum sealed chamber, were heated in sequence at 1300 °C for 30 minutes at the Dalhousie line and 1250 °C in several 10 minute intervals at UCSC, in order to extract all the helium trapped within each grain. This difference in procedure is due to the different metals used to wrap the grains at each lab. Platinum is the standard at Dalhousie while niobium is used at UCSC. Since platinum had already been used to cover all the samples in this case, the laser at UCSC was calibrated to compensate for the use of Pt foil. Meanwhile a pressure line attached to the planchet was voided to a high vacuum (~10^{-8} torr) and then injected with a

manometrically calibrated amount of ^{3}He spike (0.1 - 1 pmol), which was allowed to equilibrate within the line. In our procedure, a spike is a liquid solution that carries a known amount of two isotopes, one of which is a radioactive isotope that is being analysed and the other a stable isotope of the same element that is enriched in proportion to the other. The ^{4}He extracted from the sample was then introduced to the pressure line where it equilibrated with the spike and was then introduced into the mass spectrometer for measurement. For each grain, ^{4}He/^{3}He ratios were measured over 30 cycles in order to obtain a mean ratio. The process was then repeated a second time to extract any remaining ^{4}He within the grain. If the re-extracted quantity of gas was > 2.5 % of the gas extracted during the initial extraction, then the crystal had to be heated and analyzed a third time to release any remaining ^{4}He that was not extracted from the grain during the initial run. The procedure was repeated until the amount of gas extracted was less than 2.5% of the total ratio. For most samples, a single re-extraction run was sufficient. At UCSC, to test analytical precision, a line blank, cold blank, hot blank and ^{4}He standard were analyzed between every five extractions. A line blank is a measurement taken with no sample or spiked gases added to the He line and with the extraction laser off. This is to ensure that no helium or other anomalous gases are initially present within the line. A cold blank uses a similar process but in addition, an empty platinum foil is placed on the sample planchet. A hot blank uses an empty platinum foil but in this case, the foil is heated using the extraction laser in order to confirm that no appreciable amount of helium is extracted from the foils. Both the cold and hot blanks should produce little or no helium above the level found in the line blank.

For a properly functioning helium line, the amount of gas extracted during these blank runs should be several orders of magnitude less than would be extracted from a sample. Using the analyzed $^{4}He/^{3}He$ ratio, the amount of spike added and the ratio of $^{4}He/^{3}He$ with a calibrated ^{4}He standard, the amount of ^{4}He extracted from each single grain was calculated. This is explained below in Section 3.4.4.

3.4.2 - Extraction of U and Th Isotopes

Parent isotope extraction was achieved through sample dissolution and introduction to an inductively coupled plasma mass spectrometer (ICP-MS). After ^{4}He extraction and measurement, the zircons were removed from the Pt foils because dissolved Pt and the argon plasma used within the ICP-MS may interfere with isotope measurement by producing PtAr molecules that have an atomic weight of ~235 amu, nearly identical to that of ^{235}U, one of the parent isotopes. The ICP-MS is unable to discriminate between ^{235}U and PtAr so the U concentration measured may be biased. Once removed from their foils, the zircons were placed into Teflon tubes and mixed with 50 µm of spike solution comprising 7.55 ± 0.10 ng/ml ^{236}U and 12.3 ± 0.10 ng/ml ^{229}Th.

3.4.3 - Dissolution of the Zircons

Finally, a 1:8 ratio of hydrofluoric acid (HF) and nitric acid (HNO_3) was added to each tube. Dissolution of the samples was aided by the use of high-pressure digestion vessels (also known as Parr bombs) which were placed in an oven at ~220 °C for ~72 hours to ensure full dissolution. Once removed from the bombs, the contents of each Teflon vial were transferred to a larger vial and introduced to a high-resolution (single-collector) Element-2 ICP-MS, which measured the ratios of natural isotopes (^{238}U and

^{232}Th) to spike isotopes (^{236}U and ^{229}Th). The ratios were used to calculate the concentration of natural isotopes using the isotope dilution technique (see section 2.5.4 below). Several spiked and acid blanks were analyzed concurrently with the samples in order to test the analytical precision.

3.4.4 - Isotope Dilution Technique and Calculations

Isotope dilution is a technique used to calculate the amount of a specific radioisotope in a sample based on the natural isotope ratio (e.g., ^{238}U/^{235}U) and a known isotope ratio contained in a spike solution (e.g., ^{238}U/^{236}U), which is dissolved within and mixed with the sample prior to ICP-MS analysis. The mass of a specific radioisotope in a spiked solution can be calculated according to Atterdorn and Bowen (1998):

$$N_W = S_W \left(\frac{W_N}{W_S}\right)\left(\frac{Ab_S^A - R_M * Ab_S^B}{R_M * Ab_N^B - Ab_N^A}\right) \quad \text{(Eq. 3.2)}$$

where N_w and S_w are the masses of the natural isotope A (e.g., ^{238}U) and spike isotope B (e.g., ^{236}U), respectively, W_N and W_s are the isotopic weights of the natural isotope and spike isotope, Ab_S^A, Ab_S^B, Ab_N^B and Ab_N^A are the relative abundances of isotopes A and B in the spike and in nature, and R_M is the ratio of isotopes A and B obtained through ICP-MS analysis. Solving for N_w yields a mass of the isotope of interest, which can then be converted into a concentration by dividing N_w by the mass of the zircon grain being analyzed. To solve the age equations, the number of moles of the isotope(s) of interest is needed, and so N_w is divided by the molar mass of the specific isotope to obtain its molar concentration.

3.5 - Age Calculation and Alpha-Ejection Correction

3.5.1 - U-Th/He Age Calculation

Once the concentrations of parent and daughter isotopes are known, the values are used to calculate the cooling age of the sample. The cooling age, t, is calculated using the following helium ingrowth equation (Farley, 2002):

$$^{4}He = 8[^{238}U]\left(e^{(\lambda_{238}t)} - 1\right) + 7[^{238}U]\left(\frac{1}{137.88}\right)\left(e^{(\lambda_{235}t)} - 1\right) + 6[^{232}Th]\left(e^{(\lambda_{232}t)}1\right) \quad \text{(Eq. 3.3)}$$

where [x] represents the concentration of a particular isotope (^{4}He, ^{238}U, ^{235}U or ^{232}Th), λ is the decay constant of a particular isotope and t is the uncorrected cooling age. ^{4}He is the product of the decay of several different isotopes. For each atom of ^{238}U ($\lambda=1.55e^{-10}$ years), ^{235}U ($\lambda=9.85e^{-10}$ years) and ^{232}Th ($\lambda=4.95e^{-11}$ years) that undergoes decay, eight, seven and six ^{4}He atoms are produced respectively. The cooling age cannot, however, be calculated directly using this equation since the variable t is present a number of times within the equation and cannot be isolated. There are several solutions to this problem; three of these are outlined below and their results for a single ZHe sample compared.

Linear Approximation

The simplest solution is a linear approximation of the cooling age of the sample, which is reasonably accurate when cooling ages are young ($t<<1/\lambda^{235}U$) (Veermesch, 2008). For this solution, the present day ^{4}He production rate (P) is calculated according to (Veermesch, 2008):

$$P = 8[^{238}U]\left(\frac{137.88}{138.88}\right)\lambda_{238} + 7[^{238}U]\left(\frac{1}{138.88}\right)\lambda_{235} + 6[^{232}Th]\lambda_{232} \quad \text{(Eq. 3.4)}$$

Once P is calculated, t can be calculated using the simple equation:

$$t = \frac{[^4He]}{P} \qquad \text{(Eq. 3.5)}$$

where t is an uncorrected approximation of the cooling age of the sample.

Indirect iterative method

The second solution is the most commonly used, but also the most complex. For this iterative solution the cooling age t is calculated using a Taylor Series approximation of equation 3.3. A Taylor Series approximates of a function as a sum of terms calculated from the values of its derivatives at a single point. To the first derivative, the solution is (M. G. Fellin, personal communication):

$$^4He \approx$$

$$\left\{8[^{238}U]\left(\frac{137.88}{138.88}\right)\left(e^{(\lambda_{238}t_0)}-1\right)+7\left(\frac{[^{238}U]}{138.88}\right)\left(e^{(\lambda_{235}t_0)}-1\right)+6[^{232}Th]\left(e^{(\lambda_{232}t_0)}-1\right)\right\}+\ (t_1-t_0)\left\{8[^{238}U]\left(\frac{137.88}{138.88}\right)\left(\lambda_{238}e^{(\lambda_{238}t_0)}\right)+7[^{238}U]\left(\frac{1}{138.88}\right)\left(\lambda_{235}e^{(\lambda_{235}t_0)}\right)+6[^{232}Th]\left(\lambda_{232}e^{(\lambda_{232}t_0)}\right)\right\} \qquad \text{(Eq.3.6)}$$

where the first term is approximated to be $f(t_0)$ and the third term to be $f'(t_0)$. Rearranging the equation to solve for t_1, the equation reduces to:

$$t_1 \approx \frac{^4He - f(t_0) + t_0 f'(t_0)}{f'(t_0)} \qquad \text{(Eq. 3.7)}$$

where t_0 is an initial estimate of the age of the sample and t_1 is the approximate calculated age of the sample. To solve the equation for t_1, an estimate of the cooling age must be made and substituted to the variable t_0. To test whether t_1 is an accurate value for the sample cooling age, the relative error between t_1 and t_0 must be calculated according to:

$$E_a = \frac{t_1 - t_0}{t_1} \times 100 \quad \text{(Eq. 3.8)}$$

If the error is greater than ~5%, the equation must be re-iterated a second time. The new t_1 substitutes for the previously estimated t_0, and the equation is solved again for a t_2. The error is then re-calculated. This procedure is repeated until the relative error between t_n and t_{n+1} is < 5%. Once the error is sufficiently low, the t_n calculated is the uncorrected cooling age of the sample. This is likely the most accurate solution, but it is also the most computationally intensive.

Direct non-iterative method

The third solution is a non-iterative approximation from Meesters and Dunai (2005) that is less accurate within a small percentage of error when compared to the iterative solution but requires less calculation. The solution involves calculating a total cumulative ^{4}He production value, P, such that:

$$P1 = 8\lambda_{238}[^{238}U] \quad P2 = 7\lambda_{235}[^{235}U] \quad P3 = 6\lambda_{232}[^{232}Th] \quad \text{(Eq. 3.9)}$$

$$P = P1 + P2 + P3 \quad \text{(Eq. 3.10)}$$

A weighted mean decay rate, λ_{wm}, must also be calculated, using the various isotope production rates as a weighting mechanism:

$$\lambda_{\mathrm{wm}} = \sum_{\mathrm{j}} \frac{\mathrm{P_j}\lambda_{\mathrm{j}}}{\mathrm{P}} \quad \text{(Eq. 3.11)}$$

With this value, the approximate age, t_{app}, can be calculated according to:

$$t_{app} = \frac{1}{\lambda_{wm}} ln\left(\frac{\lambda_{wm}}{P}[^4He] + 1\right) \quad \text{(Eq. 3.12)}$$

All three solutions are compared below in Table 3.1 for a single ZHe sample, ISIK-08-03, showing the relative differences between the direct solution and linear approximation compared to the indirect solution.

Table 3.1: Comparison of Age Calculation Solutions

Sample and Grain #	Indirect Solution	Direct Solution	Relative % Difference	Linear Approximation	Relative % Difference
ISIK-08-03-1	17.73 Ma	17.60	0.70	18.44 Ma	4.02
ISIK-08-03-2	10.56 Ma	10.48	0.70	10.98 Ma	3.98
ISIK-08-03-3	12.26 Ma	12.18	0.71	12.76 Ma	4.01
ISIK-08-03-4	10.92 Ma	10.85	0.71	11.36 Ma	4.03
ISIK-08-03-5	11.65 Ma	11.57	0.68	12.10 Ma	3.87

To compare both the direct solution and linear approximation methods to the more commonly used indirect method the percent difference was calculated by subtracting the resulting age using the direct solution or linear approximation from the age acquired using the indirect solution, then dividing by the indirect solution. This results in a relative percentage showing how accurate the two less common solutions are compared to the indirect solution. The direct solution is accurate relative to the indirect solution. There is less than 1% difference between the cooling ages produced between these two methods, which suggest that the direct solution is a viable, accurate and less computationally intensive substitute for the indirect solution. The linear approximation method is not as accurate as the direct solution; it overestimates ages by ~4% when compared to the indirect solution. This suggests that the direct method is ~5 times more accurate than the linear approximation method, when compared to the indirect solution. The percentage difference between the cooling ages calculated by

direct and indirect methods results in a difference in age that is far less than the age uncertainty between grains from the same sample. For this study, the indirect method is used as it is the most accurate and accepted solution.

3.5.2 - Alpha-Ejection Correction

The cooling ages are a product of the ratio of parent and daughter isotopes measured within the samples; however, these values need to be corrected for the ejection of ^{4}He (α-particles) during nuclear decay (Farley et al., 1996). During α-decay, the parent isotopes (e.g., ^{238}U) release a certain amount of kinetic energy, ejecting the produced α-particles a certain distance from the site of decay (Figure 3.5), depending on the medium. In the case of zircon, this distance is ~17-20 μm, depending on which isotope is undergoing decay (Farley et al, 1996). Consequently, there is a proportion of α-particles produced within 20 μm of the edge of the zircon grain that will be ejected from the grain and subsequently lost to the environment. The probability of ejection depends on both the distance to the edge of the grain from the site of decay and the geometry of the grain itself. This process biases the final ^{4}He concentration in the grain because some of the ^{4}He that has been produced is lost to the environment, even though the parent isotopes are still present in the grain. This results in an underestimation of the "true" age of the sample. Depending on the size, shape and age of the grain, this underestimation can be significant and must be corrected for.

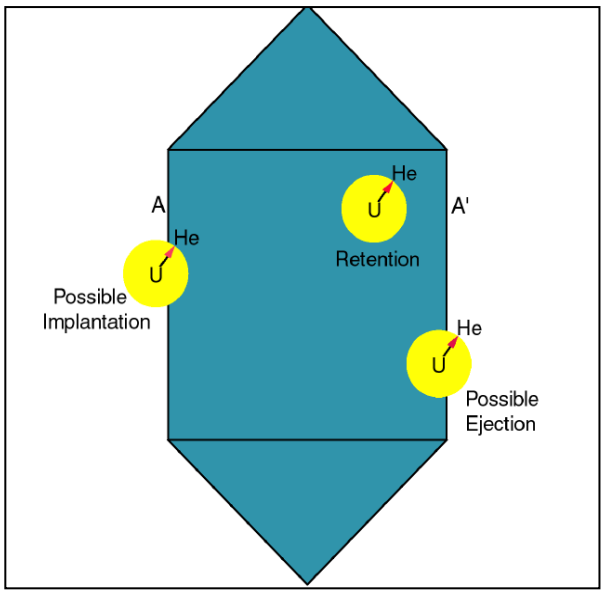

Figure 3.5: Ejection, retention, or implantation of α-particles within a euhedral zircon. If decay occurs within 20 µm of the edge of the grain, ejection or retention is possible depending on the direction (yellow circles) in which the particle moves. At a distance larger than 20 µm from the edge, all α-particles are retained within the grain. There is the possibility of implantation of α-particles from neighbouring grains but this is a rare event that requires zircon grains to be essentially in contact with each other during decay. Figure from Farley (2002).

The magnitude of the correction depends on the volume and shape of the crystal (Reiners, 2005). The volume of the grain is the most important factor as it controls the probability of ejection. The outer 20 µm of a grain represents a smaller percentage of the total volume of a larger grain, which results in a smaller percentage of ejections, and subsequently a smaller correction. Because of this, the smallest acceptable crystal size should be no less than ~60 µm (Reiners, 2005). Smaller grains involve an unreasonably large α-ejection correction and were not used in this study. Grain morphology is also important because α-particles have a higher probability of ejection at the corner of a crystal (>50%) than along a flat face (~50%). As a result, the largest corrections are associated with anhedral grains with high surface area to volume ratios (SA/V) while the smallest are associated with euhedral grains (Reiners, 2005). For zircons, the preferred

morphology is a euhedral rectangular prism with well-preserved pyramidal terminations. To calculate the α-correction, the following equation is used (Reiners, 2005):

$$F_{He} = 1 + A_1\beta + A_2\beta^2 \quad \text{(Eq. 3.13)}$$

where F_{He} is the correction factor, β is the surface-area-to-volume ratio of a particular grain, and A_1 and A_2 are isotope-mineral-and geometry-specific diffusion parameters; values for A_1 and A_2 were calculated for euhedral zircons by Hourigan et al. (2005). A correction factor is calculated for each isotope since U and Th have slightly different ejection distances and activities. These values are then combined to calculate a bulk correction value weighted by the ratio of U to Th (Reiners, 2005):

$$F_{BHe} = {a_{238}}^{^{238}U}F_{He} + (1 - a_{238})^{^{232}Th}F_{He} \quad \text{(Eq. 3.14)}$$

where

$$a_{238} = \left(1.04 + 0.245\left(\frac{[Th]}{[U]}\right)\right)^{-1} \quad \text{(Eq. 3.15)}$$

The bulk correction is then applied to the uncorrected age using Farley et al. (1996):

$$t_{corr} = \frac{t_{uncorr}}{F_{BHe}} \quad \text{(Eq. 3.16)}$$

This equation can be modified to correct the ^{4}He values instead of the ages in order to propagate the correction through the age equation (Min et al., 2003). This is the preferred method at the UCSC laboratory where the samples were processed and was therefore used in this study.

3.6. Other ZHe Considerations and Assumptions

The (U-Th)/He method requires a number of assumptions and parameters to be taken into account, to obtain geologically meaningful cooling ages.

3.6.1 - Presence of Pre-Existing Helium

Pre-existing ^{4}He in the crystals would bias the cooling ages by overestimating them. The method assumes that the crystals do not initially contain ^{4}He that would be derived from geologic or atmospheric sources. This assumption is most likely valid in the case of an atmospheric source because the concentration of ^{4}He present in the Earth's atmosphere (~5ppm) is insignificant, as is the amount produced within the Earth (Farley, 2002).

3.6.2 - Secular Equilibrium

Secular equilibrium is a state that occurs when the production and the decay rates of a particular radiogenic isotope become equal. It requires that the half-life of a parent isotope is much larger than the half-life of its daughter isotope, thereby limiting the radioactive decay of the daughter and eventually bringing the production rate of various daughter isotopes into equilibrium with that of the parent isotope; the amount of daughter isotope that undergoes decay is the same as the amount produced through decay of the parent isotope over geologic time. Secular equilibrium of parent isotopes is assumed so that the equation to calculate cooling age can be solved correctly (Farley, 2002). If equilibrium is not reached, Eq.3 becomes less accurate as the rate of decay of parent isotopes into the final daughter isotope will be affected. This assumption is likely valid as the half-lives of intermediate daughter products within the decay chains of parent isotopes are relatively small as compared to the half-lives of the initial parent. For example, ^{238}U has a half-life of ~4.47 Ga, while the intermediate isotope within the ^{238}U decay chain with the longest half-life is ^{230}Th with a half-life of ~77 ka; other

intermediate isotopes have half-lives on the scale of minutes to days. Thus, decay of intermediate isotopes is approximately synchronous with the decay of their initial parent. Farley (2002) pointed out that secular equilibrium is achieved (with respect to the U and Th decay chains) for crystals older than 0.35 Ma.

3.6.3 - Zonation of Parent Isotopes

The zonation of parent isotopes within analyzed crystals poses significant problems when applying the α-correction and may lead to over- or underestimates of actual cooling ages (Hourigan et al, 2005). For example, if the core of a zircon is enriched in parent isotopes as compared to its rim, fewer extra-crystal ejections of alpha particles will occur because the bulk of parent isotopes is located further than one stopping distance from the rim of the grain. It is assumed that the distribution of the parent isotopes is homogeneous within the grain. No significant zonation was observed during selection of the crystals used here, however this is based only on microscope inspection.

3.6.4 - Samarium (Sm)

In some cases, Sm may be a significant ^{4}He producing parent isotope, for example, for apatite crystals showing high Sm concentrations (e.g., the Durango apatite, Reiners and Nicolescu, 2006). However, Sm only produces a single ^{4}He particle through its short decay chain, compared to 8, 7, and 6 for ^{238}U, ^{235}U and ^{232}Th, respectively. In addition, the half-life of Sm (~1.06 Ga) is very long so very few decays are likely to take place unless the samples are very old. Despite this, the decay of Sm can contribute significantly to ^{4}He production in samples with a high Sm concentration. In contrast to apatites, zircons tend to have lower Sm concentrations, which does not significantly

affect the cooling age of the zircon crystals (Reiners, 2005). With this in mind, the contribution of Sm to α-particle production was not taken into account in this study. If Sm was present in some of the zircon grains, our ZHe ages would overestimate the cooling ages.

3.7 - ZHe Cooling Age Results

Eighteen samples of zircon were analyzed using U-Th/He thermochronology. For data reproducibility five aliquots per sample were processed, except for sample ISIK-08-36 where only three acceptable grains were found. Several samples contained outlier data that were discarded due to anomalous U, Th or He concentrations. Single-grain ages that were more than two standard deviations older or younger than the mean cooling age of the sample they belonged to were discarded and the sample mean recalculated with the remaining grains. The standard error was calculated for each sample by dividing the population standard deviation by the square root of the number of samples. Here we present the results of our ZHe thermochronology (Table 3.2).

3.7.1 - ZHe Cooling Age Descriptions

Of the 18 ZHe samples originally processed, 17 were selected for use in this study. The samples produced late Miocene-Pliocene cooling ages ranging from 1.30 ± 0.03 Ma to 12.94 ± 1.05 Ma (Figure 3.6). The omitted sample, ISIK-08-04, yielded single-grain ages ranging from 167 Ma to 355 Ma, indicating that this sample was not completely reset or possibly had an inclusion that was not detected. The results are shown in Table 3.2. Shown are the sample numbers, the amount of parent and daughter isotopes in moles, the grain dimensions, the α-correction factor, the single grain ^{4}He

corrected ages in Ma, mean sample age and the statistical error of this mean age. Data shown in red were discarded.

Several aliquots were discarded on the basis of anomalous isotope values and several others because of significantly too young or old ages compared to the rest of the grains in their respective samples. A single aliquot was also lost during processing and another did not contain helium and was discarded (ISIK-08-01-1). These aliquots are shown in red in Table 3.2. Two Fish Canyon Tuff zircon standards were also analyzed at UCSC for precision and returned uncorrected ages of 26.31±0.92 and 20.83±0.33. The first standard returned an age slightly too old but the second was within error of the ~21 Ma (average) uncorrected age obtained by Reiners et al. (2004) using the (U-Th)/He system.

Table 3.2: Zircon (U-Th)/He results.

Sample Number	^{4}He (mol)	^{238}U (mol)	^{235}U (mol)	^{232}Th (mol)	Mean L (μm)	Mean R (μm)	Uncorrected Age (Ma)	Age Correction	Corrected Age (Ma)	Mean Age (Ma)	Error (Ma)
ISIK-08-01-1	2.26E-13	N/A	N/A	N/A	3.56E+02	9.24E+01	N/A	0.77	N/A	12.94	1.05
ISIK-08-01-2	5.03E-13	3.60E-11	2.61E-13	5.80E-12	3.17E+02	1.11E+02	10.44	0.80	12.83		
ISIK-08-01-3	1.59E-13	1.55E-11	1.13E-13	2.35E-12	2.67E+02	7.52E+01	7.63	0.72	10.25		
ISIK-08-01-4	1.65E-13	1.06E-11	7.71E-14	6.04E-13	2.21E+02	7.34E+01	11.89	0.71	16.16		
ISIK-08-01-5	6.30E-13	4.82E-11	3.49E-13	8.00E-13	2.91E+02	1.05E+02	10.08	0.79	12.50		
ISIK-08-03-1	1.19E-13	7.48E-12	5.42E-14	7.57E-13	2.12E+02	6.75E+01	12.02	0.68	16.89	10.90	1.10
ISIK-08-03-2	6.72E-13	6.55E-11	4.75E-13	6.21E-12	2.51E+02	8.46E+01	7.77	0.74	10.07		
ISIK-08-03-3	2.93E-13	2.56E-11	1.86E-13	1.92E-12	2.05E+02	7.83E+01	8.71	0.72	11.70		
ISIK-08-03-4	7.44E-13	6.97E-11	5.05E-13	3.60E-12	2.99E+02	8.64E+01	8.17	0.75	10.52		
ISIK-08-03-5	9.79E-14	8.69E-12	6.31E-14	1.98E-12	2.02E+02	8.04E+01	8.28	0.72	11.32		

Table 3.2: Continued

Sample Number	^{4}He (mol)	^{238}U (mol)	^{235}U (mol)	^{232}Th (mol)	Mean L (µm)	Mean R (µm)	Uncorrected Age (Ma)	Age Correction	Corrected Age (Ma)	Mean Age (Ma)	Error (Ma)
ISIK-08-04-1	3.01E-12	6.75E-12	4.89E-14	7.45E-12	2.62E+02	8.10E+01	269.31	0.72	371.97	273.59	29.80
ISIK-08-04-2	6.78E-13	1.93E-12	1.40E-14	1.61E-12	2.30E+02	7.47E+01	223.78	0.71	314.29		
ISIK-08-04-3	1.51E-12	8.44E-12	6.12E-14	4.79E-12	1.98E+02	7.20E+01	121.12	0.70	174.28		
ISIK-08-04-4	9.86E-13	3.41E-12	2.47E-14	3.01E-12	1.91E+02	7.29E+01	183.43	0.70	263.93		
ISIK-08-04-5	1.49E-12	6.17E-12	4.47E-14	1.64E-12	2.44E+02	7.47E+01	173.84	0.71	243.47		
ISIK-08-05-1	6.95E-13	3.33E-11	2.41E-13	2.04E-12	2.14E+02	9.81E+01	15.93	0.76	20.30	11.87	0.49
ISIK-08-05-2	2.98E-13	2.59E-11	1.88E-13	1.93E-12	2.53E+02	1.01E+02	8.75	0.77	10.95		
ISIK-08-05-3	3.57E-13	2.62E-11	1.90E-13	9.29E-12	2.50E+02	7.74E+01	9.76	0.72	13.02		
ISIK-08-05-4	4.15E-13	3.55E-11	2.57E-13	1.27E-11	2.60E+02	8.82E+01	8.37	0.75	10.82		
ISIK-08-05-5	2.75E-13	2.22E-11	1.61E-13	2.36E-12	1.89E+02	7.56E+01	9.39	0.70	12.67		
ISIK-08-07-1	5.96E-14	6.55E-12	4.75E-14	6.63E-13	2.20E+02	7.48E+01	6.89	0.71	9.39	8.33	1.05
ISIK-08-07-2	7.99E-14	6.67E-12	4.84E-14	8.83E-13	1.99E+02	7.47E+01	9.00	0.70	12.24		
ISIK-08-07-3	4.99E-14	6.62E-12	4.80E-14	9.17E-13	2.07E+02	6.66E+01	5.66	0.68	7.92		
ISIK-08-07-4	7.23E-14	1.12E-11	8.16E-14	9.24E-13	2.80E+02	7.29E+01	4.88	0.71	6.56		
ISIK-08-07-5	6.85E-14	1.24E-11	8.98E-14	1.47E-12	2.44E+02	8.01E+01	4.17	0.73	5.52		
ISIK-08-08-1	8.85E-14	1.57E-11	1.14E-13	1.94E-12	1.91E+02	1.14E+02	4.24	0.77	5.29	6.62	0.48
ISIK-08-08-2	5.07E-14	6.16E-12	4.47E-14	3.10E-12	2.34E+02	8.82E+01	5.71	0.74	7.40		
ISIK-08-08-3	1.04E-13	1.50E-11	1.09E-13	1.01E-11	2.33E+02	8.91E+01	4.65	0.75	6.03		
ISIK-08-08-4	2.16E-14	2.62E-12	1.90E-14	9.28E-13	1.53E+02	7.11E+01	5.91	0.67	8.30		
ISIK-08-08-5	2.98E-13	4.87E-11	3.53E-13	3.51E-12	2.03E+02	8.73E+01	4.66	0.73	6.10		
ISIK-08-09-1	4.84E-14	5.76E-12	4.18E-14	1.09E-12	2.86E+02	9.00E+01	6.23	0.76	8.03	8.89	0.25
ISIK-08-09-2	7.75E-14	8.87E-12	6.43E-14	6.15E-13	1.93E+02	7.74E+01	6.66	0.71	9.07		
ISIK-08-09-3	7.37E-14	8.74E-12	6.34E-14	7.14E-13	1.74E+02	6.57E+01	6.41	0.67	9.18		
ISIK-08-09-4	7.23E-14	8.22E-12	5.96E-14	8.42E-13	2.12E+02	6.84E+01	6.65	0.69	9.28		
ISIK-08-09-5	5.76E-14	2.31E-11	1.67E-13	3.35E-12	1.91E+02	7.65E+01	1.87	0.71	2.53		
ISIK-08-10-1	2.62E-13	3.20E-11	2.32E-13	2.21E-12	2.55E+02	8.04E+01	6.25	0.73	8.31	9.34	0.36
ISIK-08-10-2	3.64E-13	3.95E-11	2.87E-13	3.82E-12	2.91E+02	9.87E+01	6.98	0.78	8.72		
ISIK-08-10-3	7.99E-14	8.57E-12	6.22E-14	2.39E-12	2.36E+02	6.75E+01	6.79	0.69	9.46		
ISIK-08-10-4	1.21E-13	1.29E-11	9.39E-14	1.91E-12	2.03E+02	7.74E+01	7.01	0.70	9.52		
ISIK-08-10-5	5.29E-14	4.97E-12	3.61E-14	2.19E-12	1.94E+02	6.48E+01	7.48	0.67	10.68		
ISIK-08-11-1	1.28E-13	1.24E-11	9.03E-14	3.98E-12	2.50E+02	7.56E+01	7.40	0.72	9.94	10.41	0.78
ISIK-08-11-2	3.83E-14	3.15E-12	2.28E-14	7.82E-13	2.07E+02	7.11E+01	8.92	0.69	12.25		
ISIK-08-11-3	4.22E-14	2.10E-12	1.52E-14	3.48E-13	1.85E+02	6.31E+01	14.98	0.66	21.43		
ISIK-08-11-4	4.92E-14	6.07E-12	4.40E-14	4.84E-13	1.61E+02	6.12E+01	6.16	0.64	9.05		
ISIK-08-11-5	8.26E-14	2.25E-11	1.63E-13	5.99E-12	2.04E+02	8.82E+01	2.68	0.74	3.49		
ISIK-08-34-1	1.91E-13	8.53E-11	6.19E-13	3.06E-12	3.38E+02	1.09E+02	1.72	0.80	2.11	1.99	0.08
ISIK-08-34-2	6.00E-14	2.69E-11	1.95E-13	8.48E-12	2.53E+02	1.30E+02	1.61	0.81	1.94		
ISIK-08-34-3	3.12E-14	1.70E-11	1.23E-13	1.63E-12	2.31E+02	9.27E+01	1.39	0.75	1.79		
ISIK-08-34-4	1.47E-13	6.10E-11	4.42E-13	1.37E-12	3.13E+02	1.14E+02	1.85	0.80	2.27		
ISIK-08-34-5	1.76E-14	9.06E-12	6.57E-14	2.57E-12	2.83E+02	8.46E+01	1.41	0.75	1.82		
ISIK-08-36-1	3.36E-14	8.34E-12	6.05E-14	1.95E-12	2.09E+02	8.91E+01	2.96	0.74	3.86	3.50	0.25
ISIK-08-36-2	2.33E-14	7.22E-12	5.24E-14	2.03E-12	3.52E+02	7.48E+01	2.35	0.72	3.14		
ISIK-08-36-3	1.22E-13	7.00E-12	5.07E-14	5.89E-12	2.47E+02	8.73E+01	11.32	0.75	14.65		

Table 3.2: Continued

Sample Number	^{4}He (mol)	^{238}U (mol)	^{235}U (mol)	^{232}Th (mol)	Mean L (μm)	Mean R (μm)	Uncorrected Age (Ma)	Age Correction	Corrected Age (Ma)	Mean Age (Ma)	Error (Ma)
ISIK-08-37-1	1.31E-13	2.10E-11	1.52E-13	1.15E-11	3.35E+02	9.00E+01	4.29	0.77	5.45	3.90	0.25
ISIK-08-37-2	2.79E-14	6.26E-12	4.54E-14	2.95E-12	2.33E+02	1.02E+02	3.11	0.77	3.92		
ISIK-08-37-3	4.00E-14	8.53E-12	6.19E-14	3.68E-12	2.38E+02	7.47E+01	3.30	0.71	4.46		
ISIK-08-37-4	5.57E-14	1.61E-11	1.16E-13	6.70E-12	2.58E+02	8.73E+01	2.45	0.75	3.17		
ISIK-08-37-5	3.80E-14	1.39E-11	1.01E-13	4.55E-12	2.72E+02	9.00E+01	1.96	0.76	2.53		
ISIK-08-38-1	1.40E-13	3.81E-11	2.76E-13	6.73E-12	4.11E+02	1.19E+02	2.73	0.82	3.29	2.81	0.27
ISIK-08-38-2	3.52E-13	1.01E-10	7.35E-13	1.06E-10	5.83E+02	1.43E+02	2.17	0.85	2.52		
ISIK-08-38-3	6.97E-14	1.99E-11	1.44E-13	5.12E-12	2.91E+02	1.29E+02	2.56	0.82	3.08		
ISIK-08-38-4	N/A	6.24E-11	4.52E-13	2.39E-12	2.74E+02	1.06E+02	N/A	0.78	N/A		
ISIK-08-38-5	2.61E-13	9.62E-11	6.98E-13	2.83E-11	3.83E+02	1.26E+02	1.97	0.82	2.34		
ISIK-08-39-1	1.98E-13	3.91E-11	2.84E-13	2.20E-11	3.79E+02	1.15E+02	3.46	0.81	4.18	3.29	0.25
ISIK-08-39-2	2.13E-13	1.54E-11	1.11E-13	1.67E-11	2.54E+02	9.00E+01	8.58	0.75	11.03		
ISIK-08-39-3	1.39E-12	3.45E-10	2.50E-12	3.60E-12	2.62E+02	9.45E+01	3.11	0.76	3.93		
ISIK-08-39-4	1.24E-13	3.55E-11	2.57E-13	1.41E-11	3.78E+02	8.55E+01	2.48	0.76	3.17		
ISIK-08-39-5	4.85E-14	2.46E-11	1.78E-13	1.19E-11	2.01E+02	7.21E+01	1.37	0.69	1.89		
ISIK-08-41-1	2.89E-13	4.85E-11	3.52E-13	6.95E-12	2.96E+02	9.87E+01	4.46	0.78	5.58	2.07	0.16
ISIK-08-41-2	2.15E-13	9.04E-11	6.56E-13	8.41E-12	3.26E+02	1.08E+02	1.80	0.80	2.21		
ISIK-08-41-3	2.11E-13	9.59E-11	6.95E-13	1.13E-11	3.57E+02	1.19E+02	1.66	0.81	2.00		
ISIK-08-41-4	1.58E-13	9.46E-11	6.86E-13	7.82E-12	2.35E+02	9.90E+01	1.27	0.77	1.60		
ISIK-08-41-5	1.98E-13	7.22E-11	5.24E-13	1.73E-11	3.74E+02	1.04E+02	2.02	0.79	2.47		
ISIK-08-42-1	5.93E-14	4.18E-11	3.03E-13	9.13E-13	2.20E+02	7.65E+01	1.09	0.71	1.47	1.30	0.07
ISIK-08-42-2	1.18E-13	1.63E-12	1.18E-14	8.17E-14	3.30E+02	9.45E+01	55.12	0.77	69.67		
ISIK-08-42-3	3.71E-14	2.86E-11	2.07E-13	2.18E-12	3.03E+02	7.74E+01	0.99	0.73	1.31		
ISIK-08-42-4	1.82E-14	1.66E-11	1.21E-13	2.01E-12	2.30E+02	7.47E+01	0.82	0.71	1.12		
ISIK-08-42-5	1.02E-17	2.29E-11	1.66E-13	1.15E-12	2.52E+02	6.66E+01	0.00	0.69	0.00		
ISIK-08-44-1	5.27E-14	3.27E-11	2.37E-13	3.94E-12	3.10E+02	9.99E+01	1.21	0.78	1.52	1.45	0.19
ISIK-08-44-2	7.17E-15	8.99E-12	6.52E-14	1.15E-12	2.27E+02	7.38E+01	0.60	0.71	0.82		
ISIK-08-44-3	9.83E-15	6.69E-12	4.85E-14	7.50E-13	2.38E+02	7.92E+01	1.11	0.72	1.49		
ISIK-08-44-4	1.10E-14	9.20E-12	6.67E-14	3.65E-13	2.22E+02	6.84E+01	0.92	0.69	1.28		
ISIK-08-44-5	4.13E-14	2.01E-11	1.46E-13	2.12E-13	2.13E+02	7.29E+01	1.59	0.70	2.16		
ISIK-08-45-1	1.21E-14	4.50E-12	3.26E-14	1.01E-12	1.68E+02	7.20E+01	1.99	0.68	2.75	1.80	0.30
ISIK-08-45-2	7.79E-15	4.03E-12	2.92E-14	3.01E-12	1.29E+02	6.84E+01	1.28	0.65	1.86		
ISIK-08-45-3	3.77E-14	2.49E-11	1.81E-13	3.71E-12	2.76E+02	1.06E+02	1.13	0.79	1.42		
ISIK-08-45-4	7.93E-15	6.85E-12	4.97E-14	6.90E-13	1.95E+02	7.65E+01	0.88	0.71	1.18		
ISIK-08-45-5	7.25E-15	1.61E-10	1.17E-12	8.91E-13	2.28E+02	8.64E+01	0.03	0.74	0.05		

The age distribution obtained along the transect (Figure 3.6A) is well defined and shows little scatter (Figure 3.6B). The oldest ages (6.62 Ma - 11.87 Ma) represented by six samples are concentrated within the Siwalik foothills, southern LHS, and near the

Darjeeling Klippe. Cooling ages are considerably younger northwards across the Rangit Window based on two samples (3.50 Ma – 3.90 Ma). Within the northern part of the Tista and into the MCTZ/GHS, cooling ages become slightly younger towards the north (1.30 Ma – 1.99 Ma) with the youngest age being reached north of the MCT/HHT in the southernmost GHS. The final three samples increase in age marginally (2.07 Ma – 3.29 Ma) towards the north within the GHS.

As the profile crosses the MCT/HHT, no significant change in the age pattern is observed which is expected across a fault zone that was not active during the age range of the samples. It is likely that these young ages however, are the product of high rock uplift rates associated with slip along the deep ramp of the MHT. The southern boundary of this ramp correlates to a surface position just north of the HHT and marks a boundary where the kinematic velocity field of particle field changes from nearly horizontal (above a flat) to having a large vertical component (above a ramp). The most southern, and also oldest, samples are all located north of the MFT/MBT, the current active thrust fault. This would usually result younger ages in the hanging wall of the active structure but the southernmost samples are the oldest in the dataset. These samples were taken in the MCTZ and LHS near the Darjeeling klippen which is an uneroded remnant of the GHS from before the overlying nappe was eroded away. The cooling ages from samples taken near the klippen may represent previous thrusting of the hot GHS on top of the LHS.

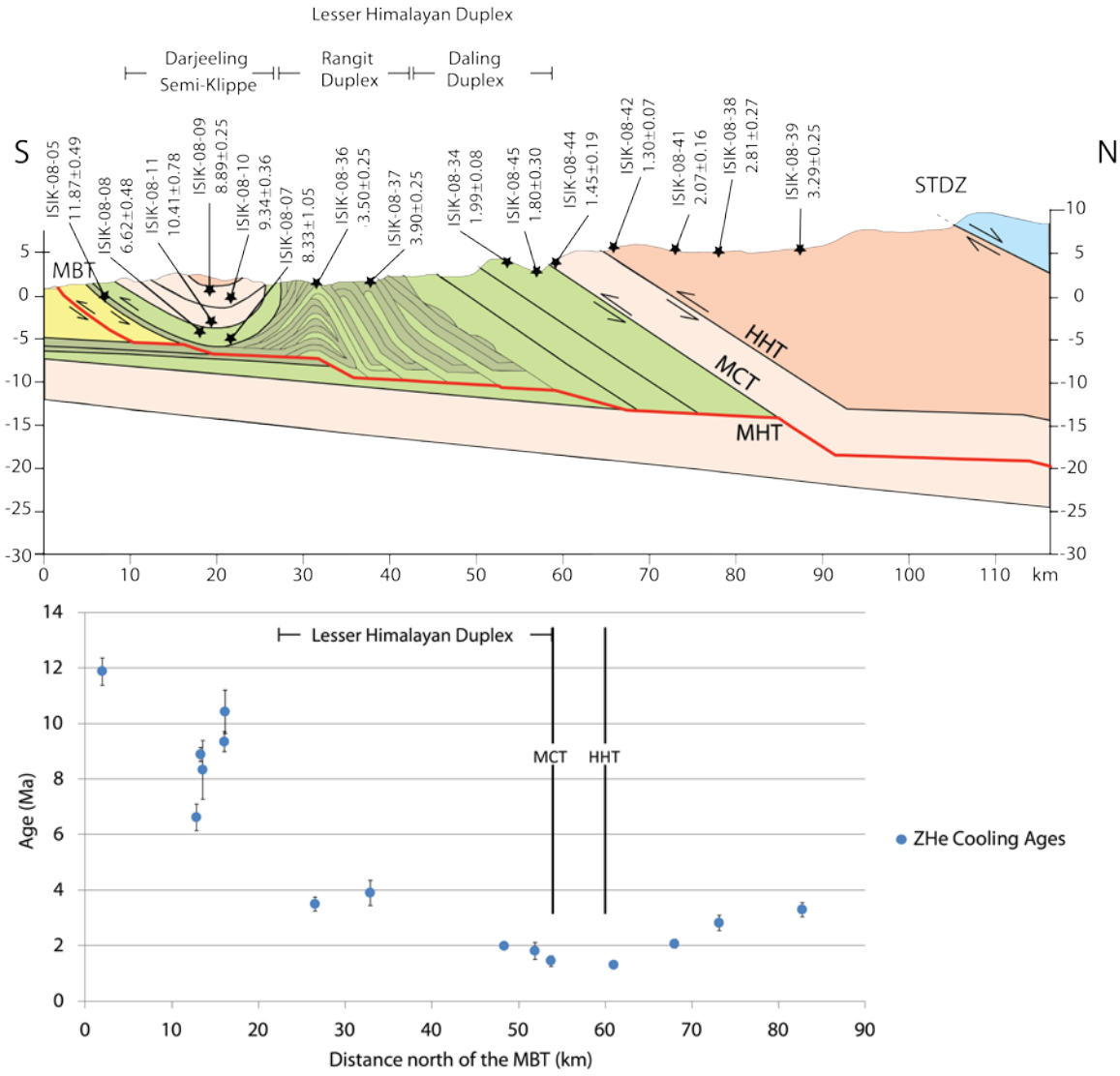

Figure 3.6: a) Schematic cross section through Sikkim showing sample cooling ages in relation to the major geological units and structures. Legend is the same as Figure 2.2. Modified from Mitra et al., 2010. b) Distribution of cooling ages with statistical error bars plotted against their distance north of the MBT.

The cooling ages were also plotted with respect to elevation in order to determine if any age-elevation patterns exist (Figure 3.7). There does not appear to be any clear pattern of cooling ages with elevation as samples with similar ages are found at different elevations. The only consistent observation is that all samples above 2500 m have cooling ages between 2-4 Ma but other samples within the same age range are also

found at lower elevations. This lack of an age-elevation pattern suggests that the cooling age pattern is, for the most part, not controlled by the current topography.

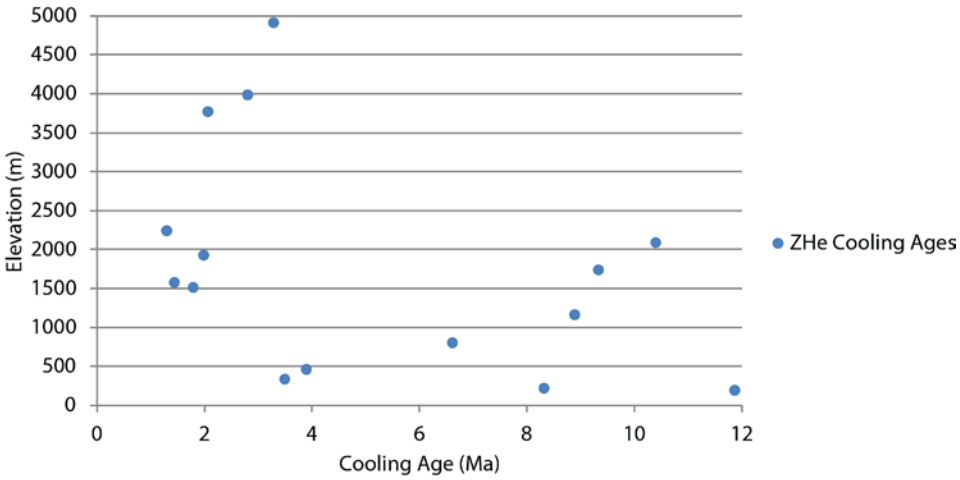

Figure 3.7: Distribution of cooling ages with respect to elevation.

Chapter 4 - Interpretation of ZHe Ages and Numerical Modelling Results

This section introduces the thermal model used in this study and provides justification for the use of thermo-kinematic modelling for interpreting thermochronological data in continental areas where the thermal state of the crust is perturbed by active tectonics.

4.1 - Thermal Field in the Continental Crust

A cooling age depends both on the spatial and temporal evolution of the thermal field and on the rock particle pathway as material travels through the crust during exhumation. Consequently, the way heat is produced, diffused and advected within the crust is integral to the interpretation of thermochronological data. The following section briefly outlines the characteristics of the crustal thermal field and how it is perturbed by geological processes.

It has long been recognised that the temperature beneath the surface increases with depth with typical values of the geothermal gradient, the rate at which the subsurface temperature changes with depth, of 20-30 °C/km measured in mines and deep drill holes (Beardsmore and Cull, 2001). Within the upper crust, the geothermal gradient depends on the heat flux into the base of the crust, the heat production within the crust, the thermal properties of the rocks, and the effects of topography, faulting, erosion and sedimentation, which affect the spacing and shape of isotherms (e.g., Mancktelow and Grasemann, 1997; Ehlers, 2005). In one dimension, the heat flux within the earth can be calculated using Fourier's Law (e.g., Beardsmore and Cull, 2001):

$$q = -k\frac{dT}{dz} \qquad \text{(Eq. 4.1)}$$

where q is the heat flow, k is the thermal conductivity and dT/dz is the geothermal gradient. There is significant variability in surface heat flow at both regional and global scale (Ehlers, 2005). The thermal conductivity of rocks near the surface generally ranges between 2-3 W/m*k (Beardsmore and Cull, 2001) measured through laboratory tests. Thermal conductivity measurements of GHS gneisses from Nepal show a range of 2-3 W/m*k perpendicular to the foliation and a much greater range of 2.4-5 W/m*k parallel to the foliation (Whipp et al., 2007).

Within the earth, significant quantities of crustal heat are produced *in situ* through radioactive decay of ^{238}U, ^{235}U, ^{232}Th and ^{40}K (e.g., Urey et al., 1955), accounting for up to 80% of the heat flux emanating from the crust at the surface today (Beardsmore and Cull, 2001). The value of heat production varies both horizontally and vertically due to changing rock types (Ehlers, 2005) and concentrations of heat-producing elements, and hence contributes to spatial variation in the geothermal gradient. Data from the GHS in Nepal suggests an average range of radiogenic heat production of ~1-3 $\mu W/m^3$ (England et al., 1992; Whipp et al., 2007).

4.1.1 - The Effects of Thrust Faulting on the Crustal Thermal Field

Within the crust, heat is transferred by two processes: conduction and advection (Beardsmore and Cull, 2001). Conductive heat transfer in the presence of a temperature gradient results from molecular interactions without any net movement of rock. Advection, on the other hand, involves the movement of heat by physical displacement of rock, magma or fluid. In large convergent orogens, thrust faults transport not only crustal material but also the heat associated with that material (Ehlers and Farley, 2003

and references therein). Hence, tectonic displacements affect the local thermal structure by advecting heat and deforming isotherms (Figure 4.1). The upward displacement of hotter material in the hanging wall of a thrust fault relative to cooler rocks in the footwall may also create a temperature gradient across the fault generating significant lateral heat flow (Ehlers 2005).

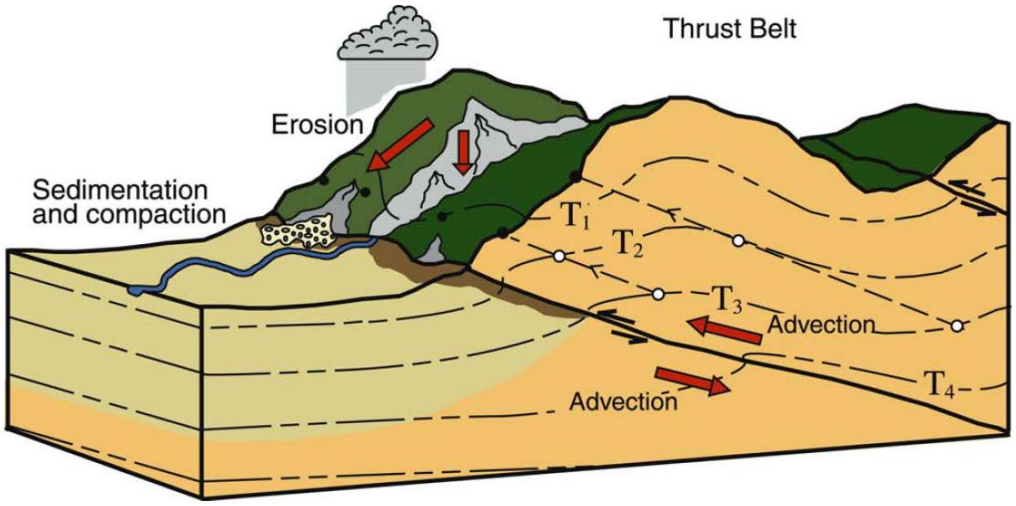

Figure 4.1: Effects of topography and thrust faulting on the thermal structure of the upper crust. The exhumation path of surface rock samples (white dots) and the advection of the isotherms (dashed black lines) are controlled by the underlying thrust fault kinematics and geometry. Topography further perturbs the temperature field such that the near-surface isotherms tend to mimic topography at first order. The degree to which the isotherm will be deformed in response to topography, depends on 1) the wavelength and amplitude of surface topography and 2) the temperature/depth of the isotherm. The closer the isotherms are to the surface, the more they are influenced by lateral topographic gradients (see Braun, 2002). Consequently, the cooling histories of two samples starting from the same temperature at depth (white circles on the T_3 isotherm) and collected at the surface of the modern landscape (black dots) can be significantly different. Erosion and subsequent deposition of the detrital material from the surface and into adjacent sedimentary basins also contributes to altering the thermal field. (From Ehlers and Farley, 2003).

Furthermore, thrusting may reorganize radiogenic heat-producing material, moving lower heat-producing material towards the surface and burying higher heat-producing

material originally located near the surface, adding to the effects of heat advection and further perturbing the subsurface thermal field (Ehlers, 2005).

4.1.2 - Topographic Effects on the Thermal Structure

Analytical solutions and numerical models from Mancktelow and Grasemann (1997) show that the amplitude and wavelength of topography are also important parameters controlling the subsurface thermal structure. The temperature at the surface represents a thermal boundary for the rocks in the subsurface so that the temperature of the rocks just below the surface is effectively the same as that of the air above the surface. This thermal boundary forces the subsurface thermal field to deform in response to changes in topography at the surface. In tectonically active areas the near-surface isotherms roughly mimic the shape of the overlying topography. The wavelength of the topography and the local exhumation rate are the major controls on the depth of penetration of the topographic disturbance; the disturbance decays exponentially with depth proportionally with the wavelength of the topography (Beardsmore and Cull, 2001; Braun, 2002). Because of this, thermochronometric systems with lower closure temperatures (e.g., AHe) are more influenced by topography than systems with higher closure temperatures (e.g., ZHe or muscovite Ar/Ar) (Figure 4.2).

As represented in Figures 4.1 and 4.2, topography in areas of high relief can dramatically perturb sub-surface isotherms by decreasing the geothermal gradient beneath topographic highs, and increasing it under the valleys. Assuming a vertical particle trajectory, the thermochronological ages in these locations will be older and younger, respectively, than if topography were flat (Ehlers and Farley, 2003). Braun

(2005; and references therein) showed that the thermal effects of topography can lead to a larger uncertainty on thermochronological ages than the analytical error of age determination itself, suggesting a significant thermal influence that can be detected in thermochronological data.

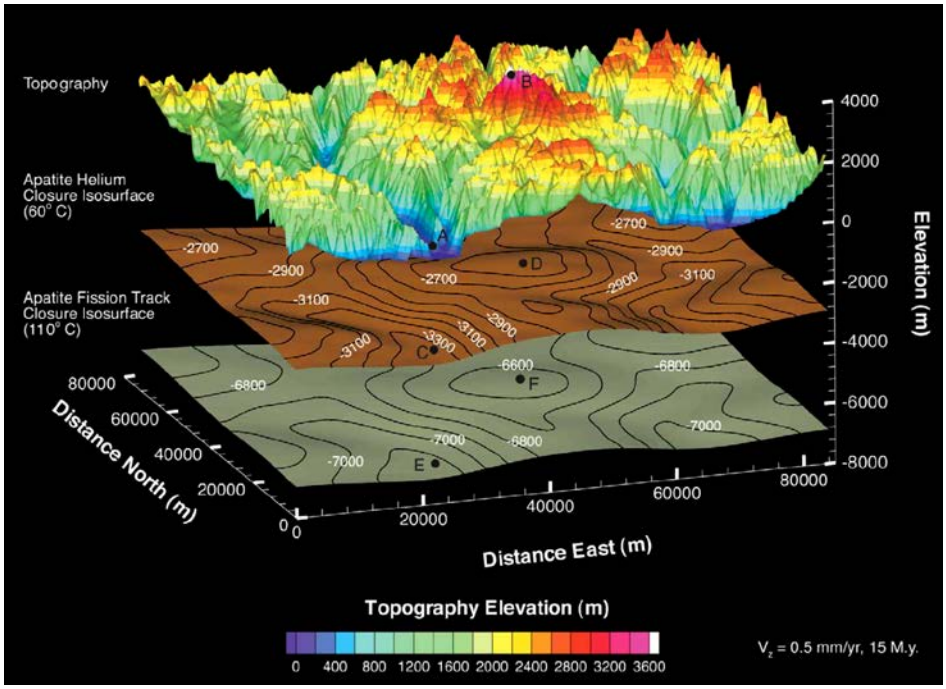

Figure 4.2: Modelled effects of surface topography in three-dimensions on the apatite helium (60°C) and apatite fission track (110° C) closure isotherms at Mt. Waddington, BC, Canada. The upper layer represents surface topography. The two underlying layers represent the subsurface topography of the 60°C and 110°C isotherms, respectively. Mountain ridges and river valleys at the surface are mimicked to some degree by the underlying thermal structure due to the conduction of heat. Deeper isotherms are less perturbed than shallower ones. This thermal model ran for 15 Ma under steady-state topography with a uniform exhumation rate of 0.5 mm/yr. (From Ehlers and Farley, 2003).

4.1.3 - Erosion and Sedimentation

Erosion and sedimentation also have a large effect on the crustal thermal structure, which is combined with the effects of topography and faulting in nature (Figure 4.3 & 4.4). Erosion results in the upward advection of relatively warm rock

toward the surface, thereby increasing the geothermal gradient and producing relatively younger cooling ages. At low rates of erosion (<1 km/Ma) the rate of change of affected cooling ages is nearly 1:1 (on a log-log scale) with the rate of erosion, and the majority of heat is transferred by conduction (Reiners and Brandon, 2006; Figure 4.3). At higher rates of erosion, material is removed fast enough for advection of heat to play a major role. In this case, as the rate of erosion increases, affected cooling ages decrease at a much higher rate (Reiners and Brandon, 2006; Figure 4.3).

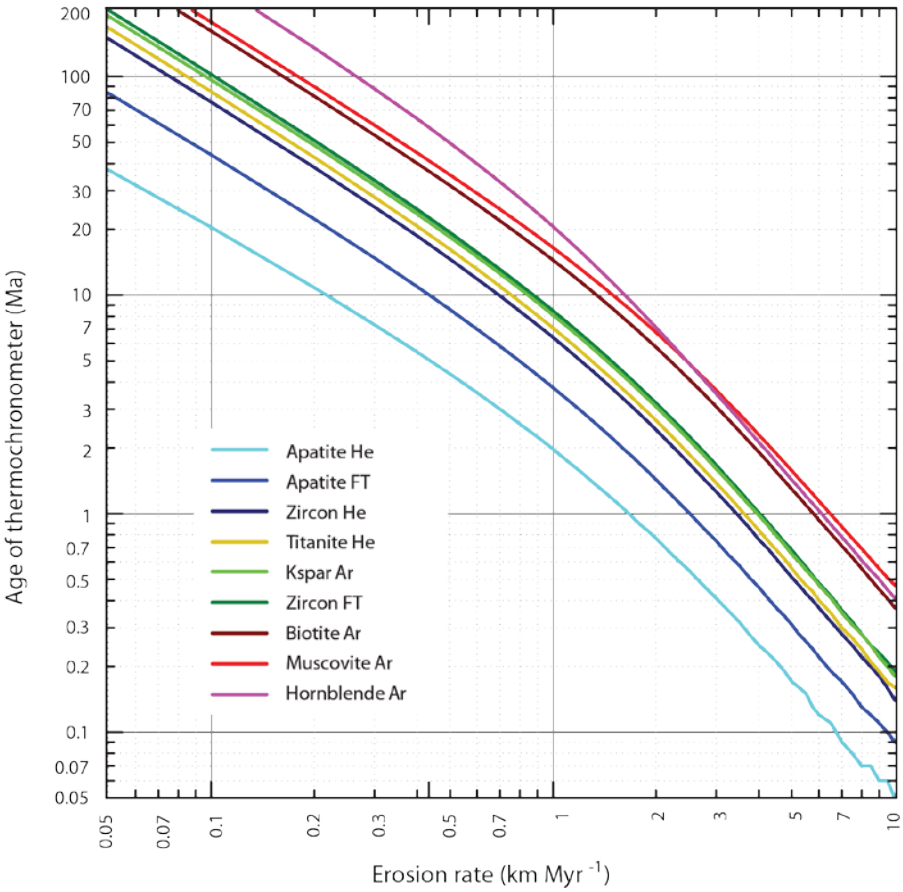

Figure 4.3: Effects of erosion rate on cooling ages of different thermochronometers from low temperature (apatite helium) to high temperature (hornblende argon). Scale is in log-log format. Cooling ages were calculated for each thermochronometer using a 1-D thermal model with a steady erosion rate. From Reiners and Brandon 2006.

This relationship can also be expressed in terms of geothermal gradient(Figure 4.4). Both erosion of surface material and re-deposition of this material elsewhere on the surface will perturb the geothermal gradient (Ehlers et al, 2005; Figure 4.4).

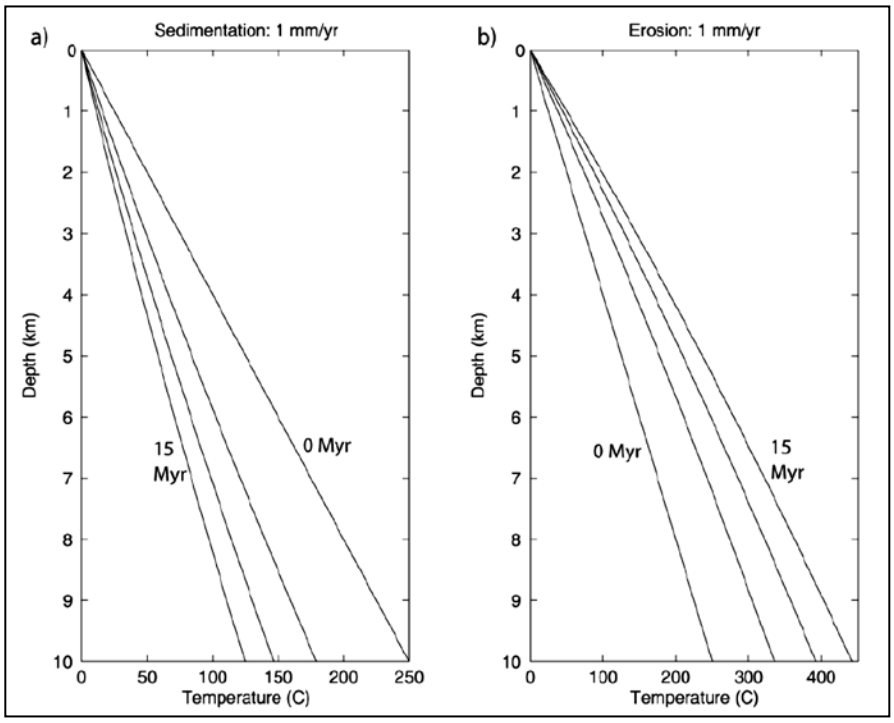

Figure 4.4: Depth-temperature plots showing how the geothermal gradient changes over time during sedimentation and erosion at a constant rate of 1 mm/yr. Sedimentation over time results in a lower geothermal gradient due to the addition of colder material (equilibrated to surface temperatures) at the surface, increasing the depth that the same temperature range must occupy. Conversely, the same rate of erosion will result in a higher geothermal gradient due to the removal of material and exposure of warmer rocks at the surface. (From Ehlers et al, 2005).

4.2 - Three-Dimensional Thermokinematic Modelling to Interpret Thermochronometer Ages

The heat transfer processes mentioned above do not modify the subsurface thermal field independently, but they interact with each other with feedbacks reaching equilibrium at a topographic and thermal steady state (Willett and Brandon, 2002). For example, an increase in rock uplift rate may result in the creation of topography, which

in turn enhances localized erosion, which may help sustain local rock uplift, all of which will modify the thermal field. The complex interactions between heat transfer processes modify the sub-surface thermal field in active convergent orogens and cannot be accounted for using simple analytical solutions and/or 1D thermal models. Instead, low-temperature thermochronometer data from these regions should be interpreted using 3D thermal and age prediction models, capable of predicting the evolution of the thermal field and taking into account complex (i.e., non-vertical) rock exhumation paths.

The set of cooling ages presented in Chapter 3 contains a record of crustal cooling that is sensitive to the major tectonic structures controlling exhumation of the samples. However, the cooling history recorded in rock samples results from a combination of kinematic and thermal effects and is therefore non-unique. To address the issue of non-unique mineral cooling histories, I use a modified version of the thermokinematic model *Pecube* (Braun, 2003; Braun et al., 2012) in combination with a formal inversion software package (Neighbourhood Algorithm; Sambridge 1999a & b) that can define the range of model parameters that is consistent with the observed cooling age data. The inversion involves two steps: sampling of the input parameter ranges for multiple variables to identify combinations that provide a good fit to the observed cooling age data; and then appraising the search results to place statistical bounds on the parameter values that provide a good fit.

4.2.1 - The *Pecube* Software

The *Pecube* software (Braun, 2003; Braun et al., 2012) calculates the 3D thermal field and predicted mineral cooling age distributions over a set period of geologic time in

a model domain using input thermal and material parameters, topography and fault kinematic data. The predicted cooling ages, and age distributions, can then be compared to the observed cooling ages in order to determine a misfit to the data, and model parameters can be varied over defined parameter ranges in order to minimize the goodness-of-fit. *Pecube* and similar software packages have been used to study exhumation in the Himalaya in several previous studies (e.g., Whipp et al., 2007; Herman et al., 2010; Robert et al., 2011; Adlakha et al., 2013; Coutand et al., 2014).

Pecube consists of three major model components: 1) a kinematic model that calculates rock exhumation paths in three dimensions based on the specified slip rate and geometry of faults, 2) a thermal model that calculates the crustal thermal field based on input thermal parameters of the crust, fault motion, surface topography, surface erosion and/or sedimentation and thermal boundary conditions at the base, sides and surface of the model, and 3) an age prediction model that predicts various thermochronologic ages from thermal histories defined by the first two components.

Kinematic Component

Rock transport in *Pecube* is controlled by user-defined fault geometries and the convergence rate accommodated by the faults. The convergence rate is partitioned into overthrusting and underthrusting by a user-defined ratio of underthrusting to total convergence. Braun et al. (2012) included thermal advection in three dimensions in order to model the effects of faulting on thermochronological data sets and the thermal field properly. Faults in *Pecube* must be defined in a local coordinate system (r,s) different than the one used to define the model space itself (x, y, z). Each vertex

constructing the fault is defined by a pair of coordinates (r, s) where r represents the horizontal distance and s the vertical depth from the surface trace of the fault (Braun, 2003). The movement histories of the faults, in the case of our models a large thrust fault, are input into the model. Slip velocities along faults are controlled by a combination of the convergence between both sides of the model (i.e.,, the Indo-Tibetan convergence rate) and a partitioning factor that defines overthrusting and underthrusting slip velocities as the ratio of the rate of underthrusting of the footwall to the total convergence rate; the reciprocal of this ratio provides the ratio of overthrusting. Lateral advection of the model topography (Whipp et al., 2009; Coutand et al., 2014) is also included to ensure rock samples above a thrust fault move nearly vertically upward during exhumation. This is important because rock transport above shallow décollement faults can produce nonsensical rock exhumation pathways (where particles exit and then re-enter the ground) when topography is assumed to be in steady state (see Appendix F of Coutand et al., 2014).

Thermal Component

The thermal model uses the finite element method to solve the heat transport equation within a crustal block taking into account uplift and surface erosion of the block. The transient 3D heat-transport equation solves for temperature iteratively in three dimensions over time (Braun, 2003; Braun et al., 2012):

$$\frac{dT}{dt} + u\frac{dT}{dx} + v\frac{dT}{dy} + w\frac{dT}{dz} = \frac{d}{dx}k\frac{dT}{\partial x} + \frac{d}{dy}k\frac{dT}{dy} + \frac{d}{dz}k\frac{dT}{dz} + A \qquad \text{(Eq. 4.2)}$$

where T is temperature , t is time, x, y and z are the spatial coordinates, u, v and w are the advection velocity components, k is the thermal conductivity of the rocks and A is

the radiogenic heat production. An initial thermal field is calculated through a combination of the velocity field controlled by fault motion, input thermal parameters and thermal boundary conditions such as the temperature at the base of the model and at the surface. The model has a constant surface and basal temperature and the sides of the model require no heat flux. An option to consider the thermal influence of groundwater flow is not included in the current version of *Pecube* so it was not considered in these models as modifying the code to include this was beyond the scope of this study.

Age Prediction Component

Prediction of cooling ages relies on the user-defined fault-slip and temperature parameters used to construct the thermal and kinematic models. To do this, thermochronological samples are first positioned on the surface of the model at their sample locations and then the modelled velocity field is used in reverse to return the samples to their initial model locations at depth. From their starting positions at depth, particle thermal histories are generated as particles are transported to the surface using the prescribed kinematic model. The resulting thermal histories are then used for age prediction. The age-prediction model for the zircon (U-Th)/He system uses the numerical scheme of Wolf et al. (1998) and the kinetic parameters of Reiners et al. (2004), based on a 100 μm grain size (Braun et al., 2012). Cooling ages are predicted from the time-temperature paths recorded for surface sample locations at each time step specified (Braun et al., 2012).

4.2.2 - Forward Modelling

In order to model cooling ages, *Pecube* requires a certain number of input thermal/physical parameters, such as thermal diffusivity, radiogenic heat production, rock density and heat capacity. In addition, surface and basal temperatures, fault movement velocity, model simulation time, and topography must be defined. Topography can also be included using a DEM (digital elevation model). Model output includes,the 3-dimensional thermal distribution over the model domain at specific time steps, as well as the predicted cooling ages of rock particles that reach the surface of the model.

4.3 - Neighbourhood Algorithm (NA) Inversion

Combining *Pecube* with the Neighbourhood Algorithm (NA) (Sambridge, 1999a & b; Rickwood and Sambridge, 2006) provides the ability to perform inverse modelling of cooling age data sets (Braun et al., 2012). These inverse models are used to define the range of input parameters that produce predicted cooling ages consistent with the observed ages. Rather than testing model parameters randomly, the NA attempts to determine the parameter ranges that fit the observed ages in a guided search of the regions of the parameter space that provide a low misfit to the data. The misfit function calculated in *Pecube* (Braun et al., 2012) is:

$$\varphi = \frac{1}{n}\sqrt{\sum_{i=1}^{n}\frac{(PredAge_i - ObsAge_i)^2}{\sigma_i^2}} \qquad \text{(Eq.4.3)}$$

where n is the number of thermochronologic ages, σ is the 1-sigma uncertainty associated with the measured thermochronometer ages, PredAge is the predicted age and ObsAge is the observed age. First, the NA sampling stage assesses input

thermochronological data in order to constrain optimal values and combinations of the free parameters; second, the NA appraisal stage calculates the probability of these parameter values taking into account the uncertainty associated with the cooling ages and the sensitivity of the model parameters to these uncertainties. Braun et al. (2012) found that ~10000 models is generally enough to invert for 5-6 free parameters to converge on lowest misfit values, but this number increases with additional free parameters.

In order to guide the inversion to areas within the parameter space that have the lowest misfit values in the search stage, the parameter space is divided into a set of Voronoï cells (Sambridge, 1999). Each of these cells is assigned a calculated misfit value so that input values for proceeding models within the inversion will be taken from cells with the lowest misfit, thereby directing the inversion to parameter ranges most likely to yield a good fit to the data. A resample ratio can be specified that corresponds to the ratio of Voronoï cells resampled to the total number of cells in the NA iteration (Braun et al., 2012). The higher this ratio, the longer the inversion will take to converge. Conversely, a lower resampling ratio will converge more quickly but possibly miss parts of the parameter space that fit the data well. Satisfactory convergence on lowest misfit values has been achieved using resampling ratios from 50 to 90% (Braun et al., 2012). We use a 90% resampling ratio for our inversions, at the expense of longer model run times, as this reduces the chances of missing local minimum misfit values that may otherwise be overlooked. A misfit value of < 1 suggests that the modelled cooling ages fit the data within the analytical error of the samples (Braun et al., 2012).

4.4 - Numerical Model Design

The *Pecube* models extend from just south of the trace of the MBT at 26.5 °N to ~160 km north at 28.0 °N and from 88 to 89 °E, an area that contains nearly all of Sikkim (Figure 2.1). The base of the model was set at 50 km depth in order to model the MHT. The DEM used to define the model topography was constructed using data from SRTM-90 taken from the CGIAR-CSI (http://srtm.csi.cgiar.org/). In the models presented below, topography is assumed to be in steady state.

The model was set up so that a single basal thrust fault equivalent to the MHT-MBT/MFT is active during the model run. Available geophysical data were used to place constraints on the location and geometry of the MHT; the MHT in Sikkim is interpreted to have a ramp-and-flat morphology rather than descending at a constant angle into the subsurface (e.g., INDEPTH; Acton et al., 2011). This fault slips at a constant rate over a specified time interval (12 Ma) in order to model the movement along the MHT from the mid-Miocene to present. All models run from 12-0 Ma because this timeframe encompasses the range of our data. In addition, activity on the major thrust faults north of the MBT (MCTZ and STDZ) are suggested to have ceased by this time (e.g., Catlos et al., 2004; Harris et al., 2004) while subsequent India-Eurasia convergence has likely been accommodated through displacement on the MBT/MFT and structural duplexing within the LHS. The rate of fault slip is defined by the convergence rate and a partitioning ratio that defines the proportion of underthrusting of India to overthrusting of Eurasia:

$$\lambda = \frac{v_u}{v_{conv}} \qquad \text{(Eq. 4.4)}$$

where λ is the partitioning ratio, v_{conv} is the convergence velocity and v_u is the underthrusting velocity. The partitioning ratio is necessary in the model setup, because although only a single fault is being modelled, it must be input into *Pecube* as two separate faults occupying the same coordinates, one moving to the south representing motion on the hanging wall block and one moving north representing motion on the footwall block. Both the footwall and hanging wall blocks move with respect to the fault itself. The modelled MHT reaches the surface through the trace of the MBT. In Sikkim, the MBT and MFT are very close to one another (within 15 km), but the MBT was chosen because its position is more accurately mapped (Figure 2.1). In addition, the MFT is thought to have been active only after the Miocene (Mukul, 2007) and the MBT is likely to have been active since 12-10 Ma (Catlos et al., 2004; Harris et al., 2004; Coutand et al., 2014). A list of model input parameters common to all of the simulations can be found in Table 4.1. Of the 16 ZHe ages obtained (see Chapter 3), only 15 were used during modelling. Sample ISIK-08-01 was not used because it is assumed to be un-reset. This sample was taken from the sedimentary rocks of the Siwaliks to the south of the MBT. The sample has an average cooling age of 12.94±1.05 Ma, much older than the suggested quaternary activation of the MFT, which is the basal thrust of the thrust sheet the sample was taken from. Also, the Siwaliks are the product of syn-orogenic erosion of material washed down from further north into the foreland basin and any zircons present would be considered detrital. This suggests that the cooling age is likely recording a previous thermal event and that the sample did not cool from its closure temperature to the surface within the MFT thrust sheet.

The misfit function calculation depends on the error associated with the samples and since many of the cooling ages have very small standard errors (Figure 3.3; Table 3.2), these ages have a greater weight in the inversions. In order to allow each sample to have equal weight when calculating the misfit function, all cooling ages used were given a uniform 1 Ma error for the purposes modelling. The initial conditions of our thermokinematic model are shown in Figure 4.5.

Table 4.1: Model Input Parameters

Parameter	Value	Unit	Reference
Material Parameters			
Thermal diffusivity	35	km^2/Ma	Ray et al., 2007
Specific Heat Capacity	800	J/kg/K	Whipp et al., 2007
Crustal Density	2700	kg/m^3	
Radiogenic Heat Production	**0-30**	°C/Ma	
Pecube Model Parameters			
Average Foreland Surface Temperature	25	°C	NOAA
Atmospheric Lapse Rate	6	°C/km	Naito et al., 2006
Basal Temperature	**500-1000**	°C	
India-Eurasia Convergence Rate	**15-25**	mm/yr	Mukul et al., 2007
Paritioning of Convergence	**0.6-0.9**		
Model Run time	12	Ma	
Model Thickness	50	km	
Horizontal Model Domain	167 x 111	km	
Vertical Node Spacing (0-5 km)	0.9	km	
Vertical Node Spacing (5-15 km)	2.7	km	
Vertical Node Spacing (15-50 km)	8.1	km	

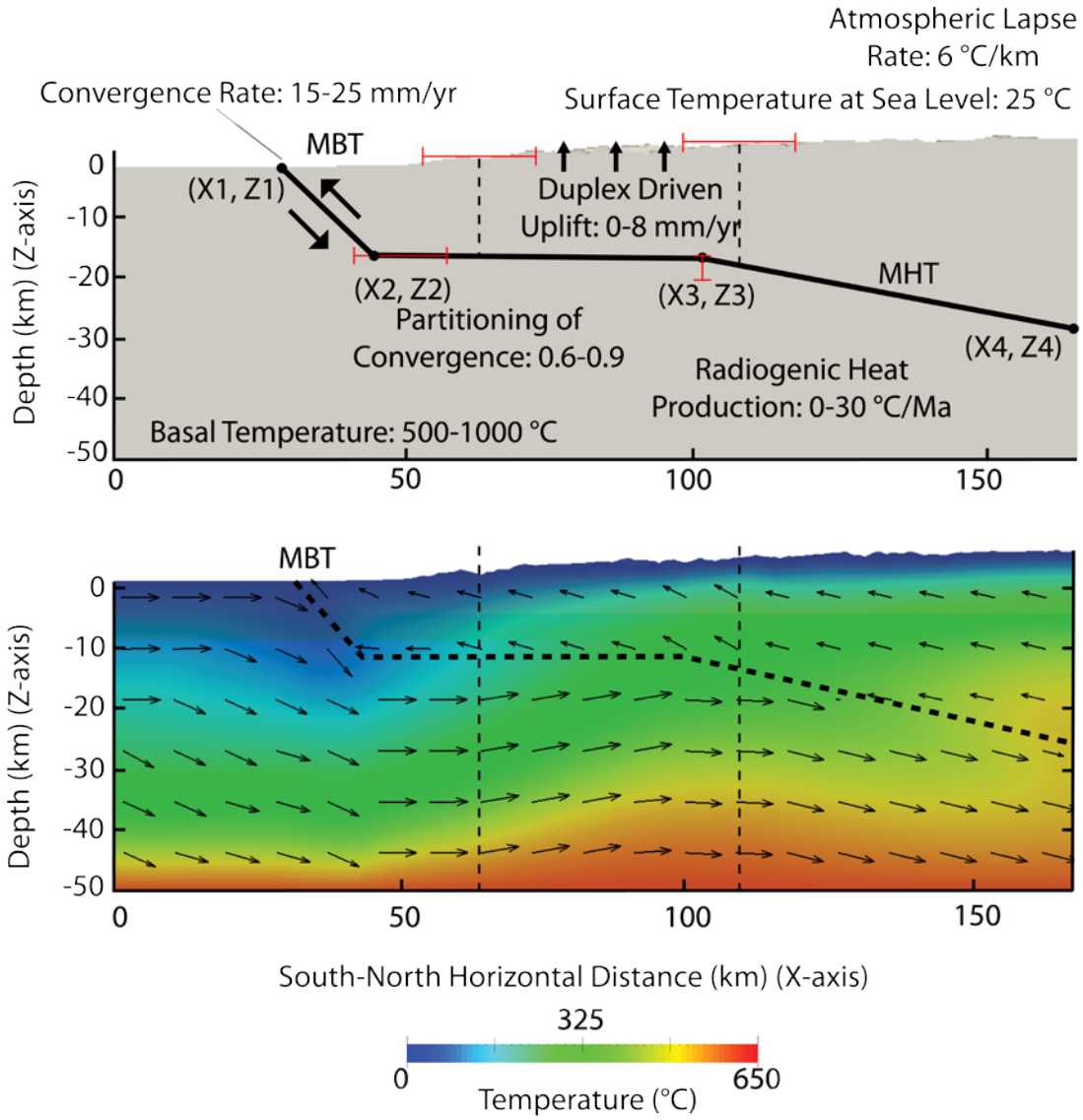

Figure 4.5: General set-up of thermokinematic models with relevant thermal and kinematic parameters and an example of the resulting thermal and velocity fields. a) Inverted values for each parameter show the total range explored over all models, individual inversion ranges are shown in Table 4.2. Red lines represent the inversion range of one vertical and one horizontal coordinate of the MHT (X2 and Z3) as well as the range of the foreland and hinterland boundaries of the duplex zone. b) Example thermokinematic solution showing the temperature and the velocity fields. The size of the arrows is proportional to the magnitude of the velocity vectors. The velocity vectors are controlled by slip along the fault (dashed line) with the vectors being parallel to the fault trace. A perturbation in the velocity field is caused by duplex driven uplift centered at ~80-90 km, introducing a larger vertical component to the vectors.

4.5 - Inversion Results

The results of four inversions are presented herein and inversion parameters are shown in Table 4.2. Values in parentheses show the range of free parameter values investigated during each inversion; values in bold are the best-fit value for each parameter in the inversion.

Table 4.2 - Inversion Parameter Table and Results

Inversion Name	SKI01	SKI02	SKI03	SKI04
Number of models	13452	16816	6168	8968
Best misfit	0.419	0.2358	0.4458	0.3228
Tb (°C)	**998.52** (500:1000)	**548.54** (500:1000)	650	650
A (°C/Myr)	**30** (0:30)	**12.68** (0:30)	15	15
Z1 (km)	0.5	0.5	0.5	0.5
X1 (km)	0	0	0	0
Z2 (km)	-11	-11	-11	-11
X2 (km)	**-13.23** (-10:-25)	-10	-10	-10
Z3 (km)	**-11.00** (-11:-15)	-11	-11	-11
X3 (km)	-73	-65	-65	-65
Z4 (km)	-35	-35	-35	-35
X4 (km)	-192	-163	-163	-163
Convergence rate (mm/yr)	**-18.80** (-15:-25)	**-21.77** (-15:-25)	**-21.38** (-20:-23)	**-22.34** (-20:-23)
Time step	1	1	1	1
Running time (Ma)	12	12	12	12
Partioning Ratio	**0.63** (0.6:0.9)	**0.61** (0.6:0.9)	**0.60** (0.6:0.7)	**0.63** (0.6:0.7)
Timing onset of duplexing	0	**11.97** (11.99:2)	11.99	11.99
Timing end of duplexing	0	0	**8.00** (8:10)	**4.00** (4:10)
Rate of duplex-driven uplift (mm/yr)	0	**2.51** (0:5)	**7.97** (0:8)	**7.00** (0:8)
Proximal location of Duplex (km)	0	**28.75** (20:40)	28.75	28.75
Distal location of Duplex (km)	0	**79.89** (60:80)	79.89	79.89

4.5.1. Scenario 1 (Inversion SKI01)

The first model scenario involves simulating slip on the basal thrust fault (MHT) at a constant rate between 12 and 0 Ma. The inversion comprises six free parameters (Table 4.2). The geometry of the MHT was allowed to be free at two points (X2 and Z3) within values defined by the geophysical data (INDEPTH; Acton et al., 2011) highlighted by the red lines on Figure 4.5. Radiogenic heat production and basal temperature were

left free between 0-30 °C/Ma and 500-1000 °C, respectively. The total Indo-Tibetan convergence rate was allowed to vary between 15-25 mm/yr which is within the estimates of 15-20 mm/yr in Sikkim (Mukul et al., 2010) and 21±1.5 mm/yr in Nepal (Lavé and Avouac, 2000). The partitioning rate was given a large range of 0.6-0.9, consistent with other kinematic modelling studies elsewhere in the Himalaya (Whipp et al., 2007; Herman et al., 2010; Robert et al., 2011; Coutand et al., 2014). The complete set of parameters used for this model is shown in Table 4.2.

SKI01 Inversion Results

A total of 13452 forward models were run using the NA module and the results are shown in Table 4.2 and Figure 4.6. The lowest misfit model produced a misfit of 0.419, which indicates an overall good fit to the dataset. In this inversion, the lowest misfit values for the thermal parameters are at the high end of the input ranges of the inputs, with a preferred basal temperature of ~1000 °C and a heat production of ~30 °C/Ma (Figure 4.6a). These thermal values produce an unrealistically high geothermal gradient which would result in the melting of most rocks near the base of the model suggesting that the best-fit modelled thermal field for this scenario is improbable. The best-fit convergence rate is near the lower end of the range given with a rate of 18.8 mm/yr as is the partitioning factor at 0.63 which suggests ~40% of the total convergence (~7 mm/yr) is accommodated through overthrusting (Figure 4.5b). These values reflect an attempt by the model to generate and match young ages observed in parts of the hanging wall by producing higher temperatures and a higher proportion of overthrusting which all result in more upward advection of heat, faster cooling, and younger ages. The

fault point Z3 yielded a lowest misfit value of 11 km, which results in a flat section of the MHT between two ramps; point X2 returned a value of ~13.2 km north of the MBT (Figure 4.6c). The resulting fault geometry matches the available geophysical data very well, resulting in a steep frontal ramp dipping at ~39° followed by a consistently flat section and finally a deeper but shallower angle ramp dipping at ~11°. The 1 and 2-D PDFs, illustrate how certain parameters are not well defined despite the low misfit value obtained for the best forward model. For example, the radiogenic heat production and partitioning ratio show normal distributions in the 1D Probability Density Functions (PDFs) (Figures 4.6a & b), while 2D PDFs show that basal temperature and convergence rates are poorly defined within 1σ error (Figures 4.6 a & b).

SKI01 Forward Model

Using the free parameter values determined by the lowest misfit model from the inversion, a single forward model was run at high resolution to compare the predicted and observed cooling ages (Figure 4.7).

The predicted ages fit the general pattern of the observed ages but quite a few samples show more than a 1 Ma difference. The six most southern ages do not match well, especially the oldest age north of the MBT where the predicted age is more than 3 Ma too young. North of the HHT the predicted ages change from being older than the observed ages to being younger towards the north, although the ages all match within error. In the central part of the section predicted ages are consistently older than the observed ages (Figure 4.7). The velocity field that controls this age pattern is shown in Figure 4.8.

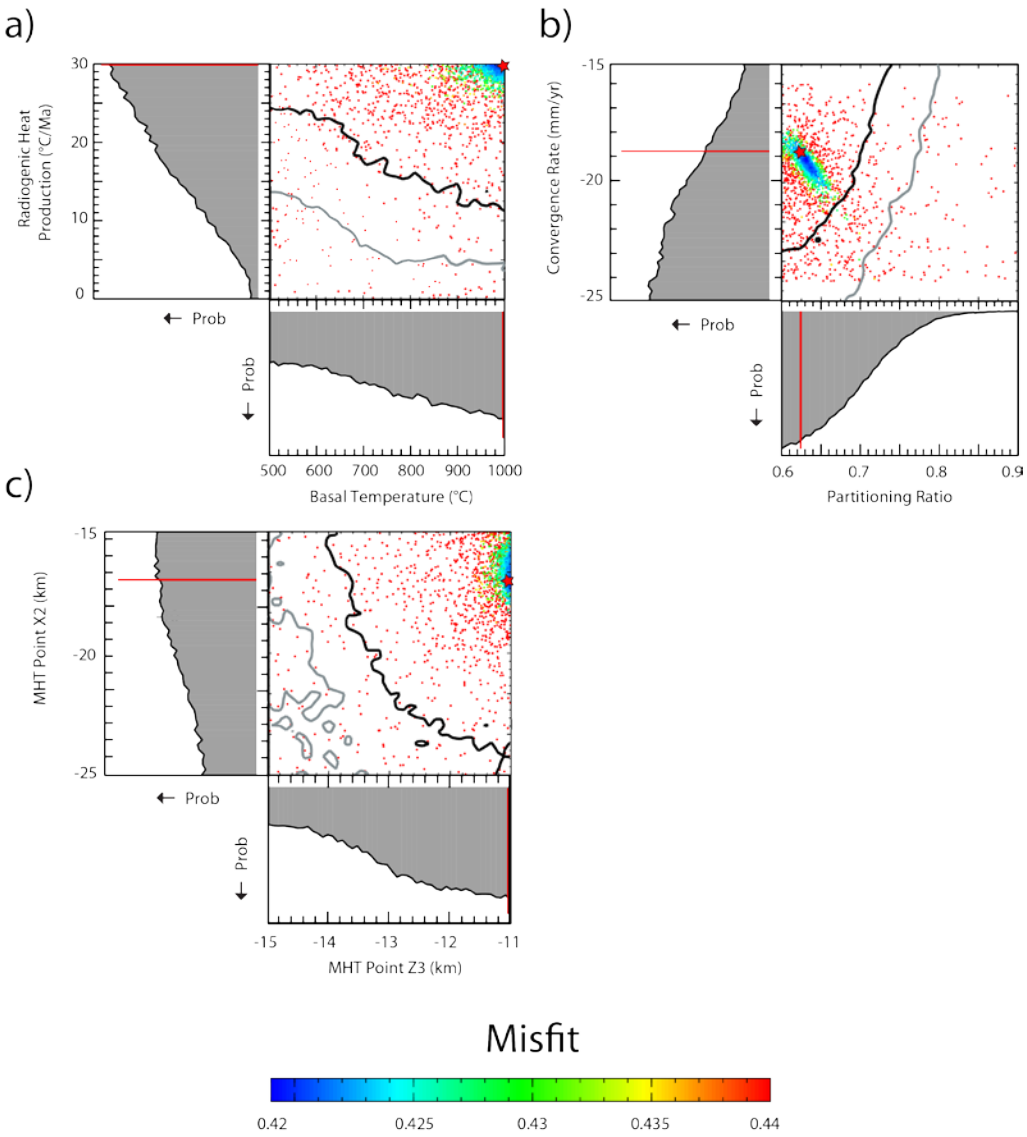

Figure 4.6: Inversion results for model SKI01 solving for six free parameters. Each of the 3 plots shows a comparison of the inversion results for two parameters. In the largest frames, each colored dot represents a single forward model, and the color scheme associated with each dot corresponds to the goodness of fit to the data set (see color scale: red dot = highest misfit, blue dot = lowest misfit). The red star represents the parameter values used in the forward model with the lowest overall misfit. One-dimensional posterior Probability Density Functions (PDFs) derived from the NA appraisal are shown adjacent to the axes for each parameter. The red lines indicate parameter values for the lowest misfit forward model. Two-dimensional PDFs are represented by lines overlying the scatter diagram where the solid black line is the 1σ confidence interval and the solid gray line the 2σ confidence interval. Most of the parameters tend to converge to the sides and corners of the plots which suggest that, for the variables used in the model, the ideal best-fit values may lie outside the ranges investigated in the inversion.

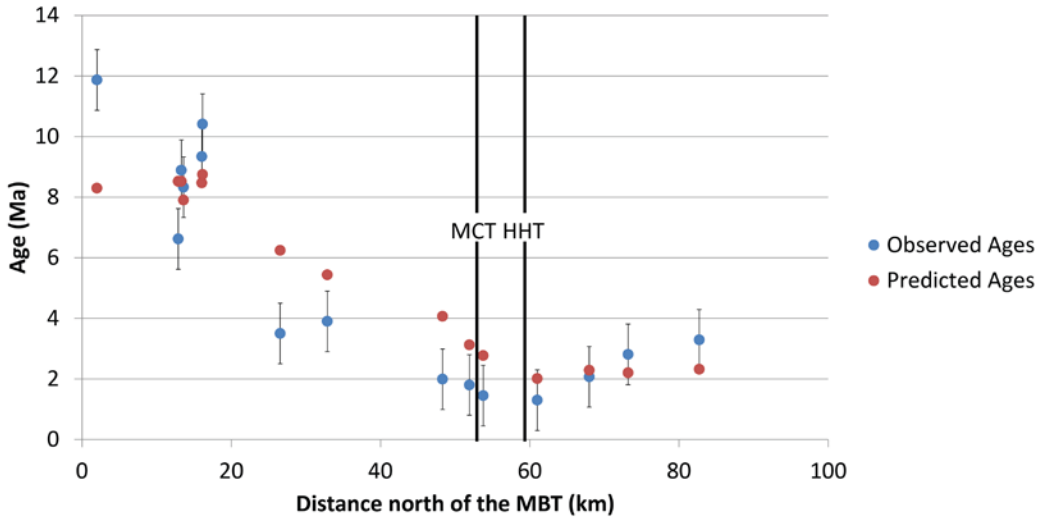

Figure 4.7: Observed cooling ages (blue) with associated 1 Ma error and predicted cooling ages (red) from the lowest misfit forward model from inversion SKI01 plotted against distance from the MBT. Black lines show the approximate locations of the MCT and HHT with respect to the samples on the transect.

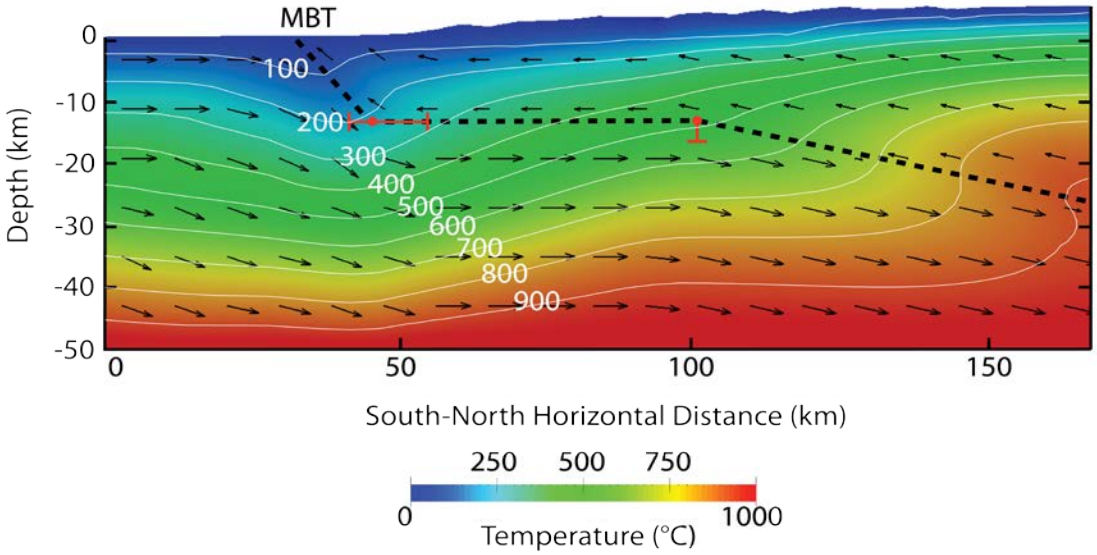

Figure 4.8: Thermal field, velocity field and MHT geometry produced by inversion SKI01. The size of the black arrows represents the average magnitude of the velocity field at that point. Velocity vectors, in this model, result from tectonic displacements along the MBT/MHT (dashed black line), which has advected and distorted the thermal field. Isotherms are shown as white lines with the temperature shown in Celsius. The capped red lines represent the 1σ error associated with the lowest misfit inverted MHT points X2 and Z3 measured using the 1σ uncertainty from the constructed 2-D PDFs in Figure 4.6.

The old predicted ages are located between ~65 -115 km on Figure 4.8, coinciding with a flat section of the MHT, producing velocity vectors with little to no vertical component within that zone. To improve the fit to the data, exhumation needs to be increased in the center of the model where the predicted ages are too old. In a second inversion (SKI02), we take into account the potential effect of the formation of the Rangit Duplex by simulating localized vertical accretion of crustal material (Figure 4.5).

4.5.2 - Scenario 2 (Inversion SKI02)

The scenario investigated in the second inversion (SKI02) introduces duplex-driven local uplift in the central part of the model coupled with steady-slip on the MHT (Figure 4.5). The location of the pro and retro-ward boundaries of the duplex zone were chosen both because they correspond to the current location of the Tista and Rangit windows (Figures 2.1 & 2.2) and because they encompass the zone in which our predicted cooling ages for SKI01 were too old as compared to the observed ages. This positioning however places the duplex zone over a flat portion of the MHT (Figure 4.5). This may not be geologically or geometrically accurate as the construction of a duplex through underplating requires a vertical component of the velocity field, which would be present if the duplex was located further north above the crustal ramp of the MHT (Figure 4.5). The inversions assess the effect of different rates and durations of localized vertical accretion related to duplex growth. Rather than simulating the complex structural deformation in natural duplexes, we use a simple zone of enhanced rock uplift as described by Herman et al. (2010). This zone of rock uplift does not emulate the

stacking of imbricates as a real duplex would so internal shortening that would occur within the duplex zone is not accounted for.

In this inversion, the basal temperature, radiogenic heat production, convergence rate and partitioning were given the same range as the previous SKI01 inversion but additional parameters were added to allow for an area of localized uplift representing the growth of a duplex in the model space above the MHT (Table 4.2). There is virtually no published geological information regarding the timing of activity, rate or spatial extent of duplexing in Sikkim. The timing of duplex initiation was allowed to vary between ~12 Ma and 2 Ma while the end time was fixed to 0 Ma. The rate of vertical uplift attributed to duplexing varied between 0 - 5 mm/yr. Since both the timing and the rate of duplexing is poorly resolved, both were given large ranges in order for Pecube to properly access the parameter space. Finally, the southern boundary of the duplex was given a range of 20 - 40 km north of the MBT and the northern boundary was given a range of 60 - 80 km north of the MBT (Figure 4.5).

SKI02 Inversion Results

A total of 16816 models were run during this inversion (Table 4.2, Figure 4.9) with a lowest misfit value of 0.236, which is considerably lower than the lowest misfit obtained in the previous inversion SKI01. The thermal parameters yielded more reasonable values during this run with a basal temperature of 549 °C and a radiogenic heat production of 12.68 °C/Ma (Figure 4.9a). These values are well within the parameter range specified, which suggests that they likely represent geologically more realistic values for this tectonic scenario. The convergence rate and partitioning ratio

yielded values of 21.77 mm/yr and 0.61, respectively (Figure 4.9b). These results still favour rapid uplift and exhumation of the hanging wall of the MHT. The preferred duplex initiation time (11.97 Ma) is essentially identical to the time at which the model starts, so that the duplex is active during the entire model run at an uplift rate of 2.51 mm/yr, in the middle of the defined range (Figure 4.9c). Finally the lowest misfit values for boundaries of the duplex are 28.75 km and 79.89 km (north of the MBT) for the southern and northern boundaries, respectively (Figure 4.9d).

As in SKI01 the 1 and 2-D PDFs suggest that many of the parameters are not well defined within the data ranges input in the model. The partitioning ratio once again shows the closest to a normal distribution while the heat production, convergence rate, duplex initiation time and southern duplex boundary parameters show much less distinct increases in probability near the lowest misfit value. The remaining parameters show very poor distributions with some showing nearly flat distributions and others showing only very poorly defined peaks.

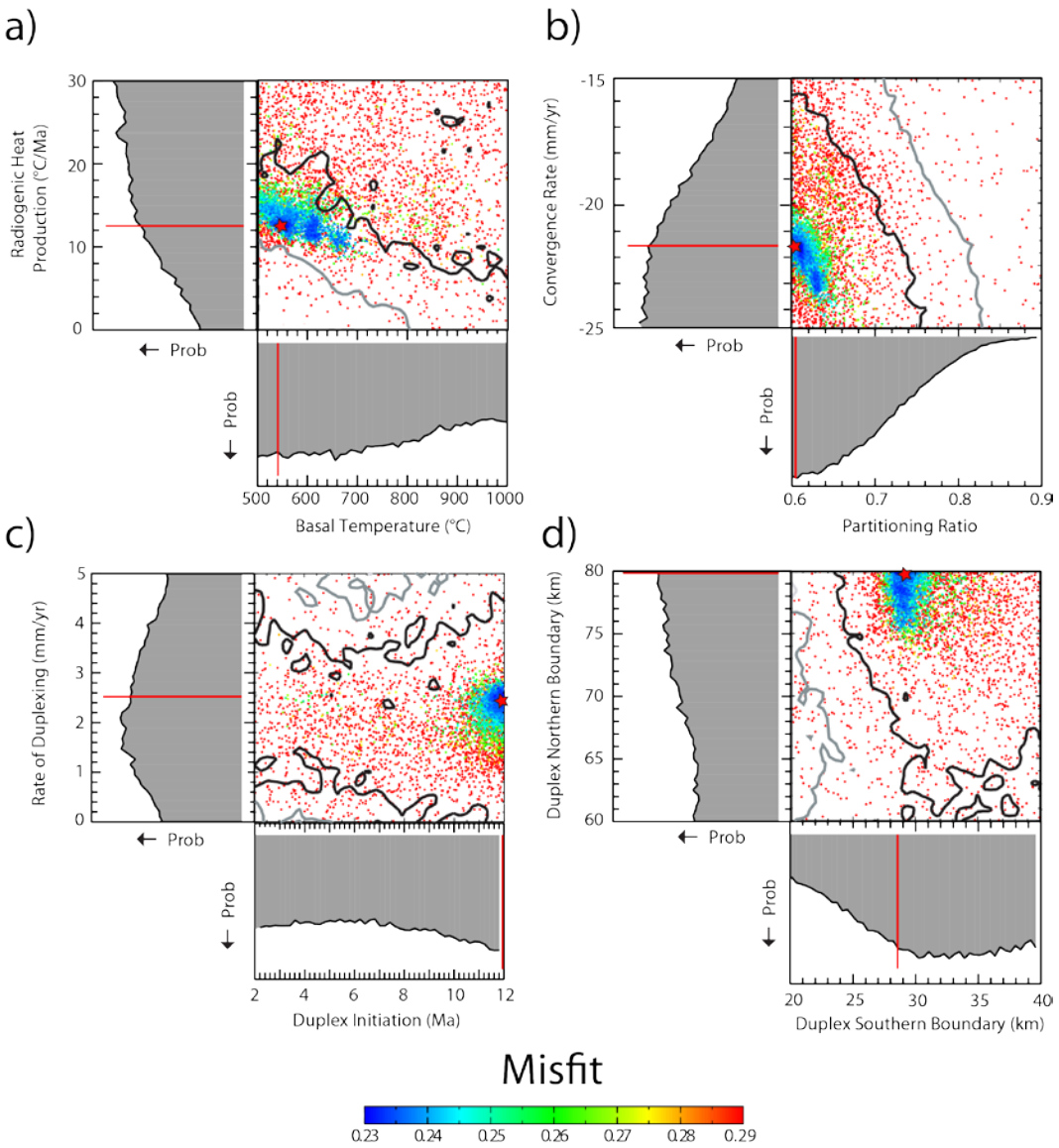

Figure 4.9: Inversion results for model SKI02 solving for eight free parameters. Plot layout and symbols are the same as in Figure 4.6.

SKI02 Forward Model

Using the parameter values from the best-fit model in inversion SKI02, a single forward model was run to compare observed and predicted ages (Figure 4.10).

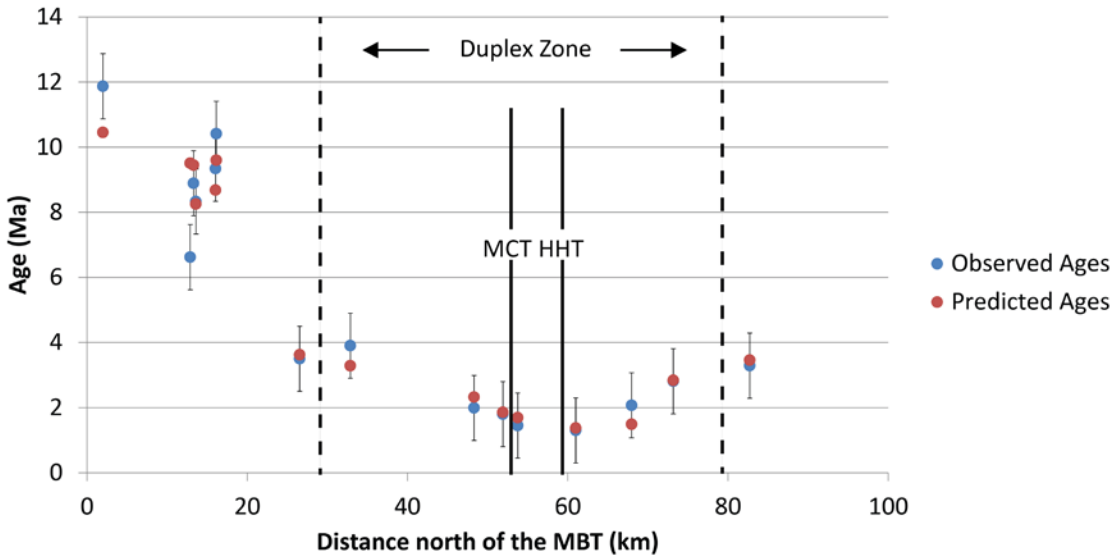

Figure 4.10: Observed cooling ages (blue) with associated 1 Ma error and predicted cooling ages (red) from the lowest misfit forward model from inversion SKI02 plotted against distance from the MBT. Black lines show the approximate locations of the MCT and HHT with respect to the samples on the transect, dashed black lines show the location of the inverted duplex zone boundaries.

In this inversion, the predicted and observed ages are, within the 1 Ma error, identical, except for the two southernmost samples (Figure 4.10). Most notably, the central part of the profile in the vicinity of the duplex shows a significant improvement in fit in this model. Overall, introducing the zone of enhanced uplift as defined by our input parameters has significantly improved the fit between the predicted and observed ages. The effects of this duplex-driven uplift zone are evident in the modelled velocity field (Figure 4.11); the velocity vectors within the duplex zone have a larger vertical component compared with the proximal vectors outside the duplex zone with the change occurring abruptly at the boundaries of the zone.

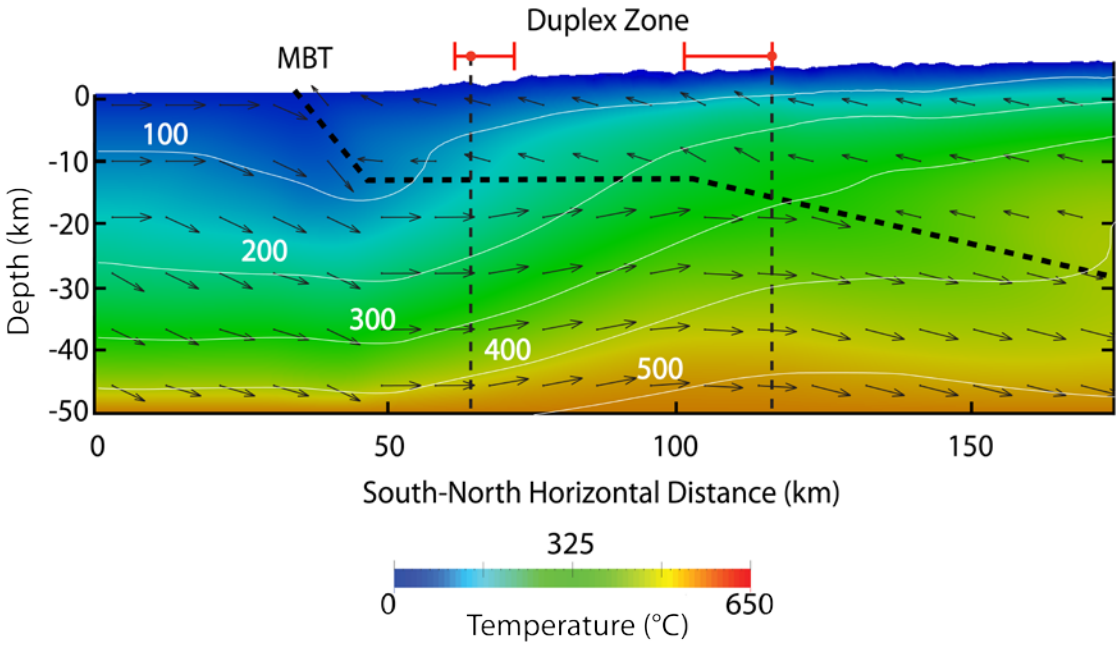

Figure 4.11: Thermal and velocity field for forward model SKI02. Vertical dashed lines indicate the lowest misfit inverted values for the foreland and hinterland boundaries of the duplex zone. Red capped lines show 1σ error (as defined by the 2-D PDFs from Figure 4.9) associated with the position of each boundary. The effect of duplexing is evident from the upward deflection of the velocity arrows in the center of the model where in the previous model they were essentially horizontal, parallel to the fault. There seems to be little obvious effect on the shape of the thermal field, however the temperature at the base of this model is 400 °C cooler than SKI01.

Although the best-fit model prescribed a duplex initiation time of ~12 Ma, there were no geological constraints placed on that parameter, as the timing of duplexing in Sikkim is currently unconstrained. The next set of models explore the possibility that duplexing initiated later than 12 Ma.

4.5.3 - Scenario 3 (Inversions SKI03 and SKI04)

While the previous scenario (Inversion SKI02) offered a very good fit to our data, it may not be completely consistent with the available geological observations. The MBT/MFT is the currently active thrust in Sikkim and is located south of the current location of the duplex zone (Figure 2.1). If the accommodation of the Indo-Tibetan

convergence by thrust faulting progressed in sequence from north to south (from the MCT to the MBT/MFT), then the duplex, which is located between the MCT and MBT, must have ceased accommodating this shortening, or at least slowed down considerably, at approximately the time at which the MBT became active or relatively soon after. This suggests that allowing the duplex to be active during the entire 12 Ma model run may not be geologically reasonable.

To test the effects of a shorter period of duplex-driven uplift, two inversions (SKI03 and SKI04) were run with only four free parameters (Table 4.2). Duplexing was set to start in the model at 12 Ma and to end between 10-8 Ma in SKI03 and 10-4 Ma in SKI04. The duplexing rate range was increased to 0-8 mm/yr for both inversions to allow a similar magnitude of rock uplift to Inversion SKI02 within the shorter duration of uplift. The convergence rate and partitioning ratio were treated as free parameters to allow the model a larger parameter space to invert for the duplexing parameters. They were given ranges of 20-23 mm/yr and 0.6-0.7, respectively. Thermal parameters and the location of the duplex zone were set using best-fit model values obtained from the previous inversion SKI02.

SKI03 Inversion Results

A total of 6168 models were run for this inversion (Table 4.2, Figure 4.12) with lowest misfit model yielding a misfit of 0.446, similar to inversion SKI01. The convergence and partitioning values are approximately the same values as in SKI02, 22.3 mm/yr and 0.63 (Figure 4.12a). The preferred values for the duplex parameters result in duplex cessation at 8 Ma and a rate of duplex-driven uplift of 8 mm/yr (Figure 4.12b).

These values suggest that in inversion SKI03 the duplexing must go on either for a longer period of time or at a faster rate to achieve the low misfit attained by the SKI02 model. They also suggest that the model is trying to produce more exhumation within the window, but could not within the defined parameter bounds. The 1-D PDFs for this model show that all four inverted parameters are poorly defined with no parameter even approaching a normal or a Gaussian distribution.

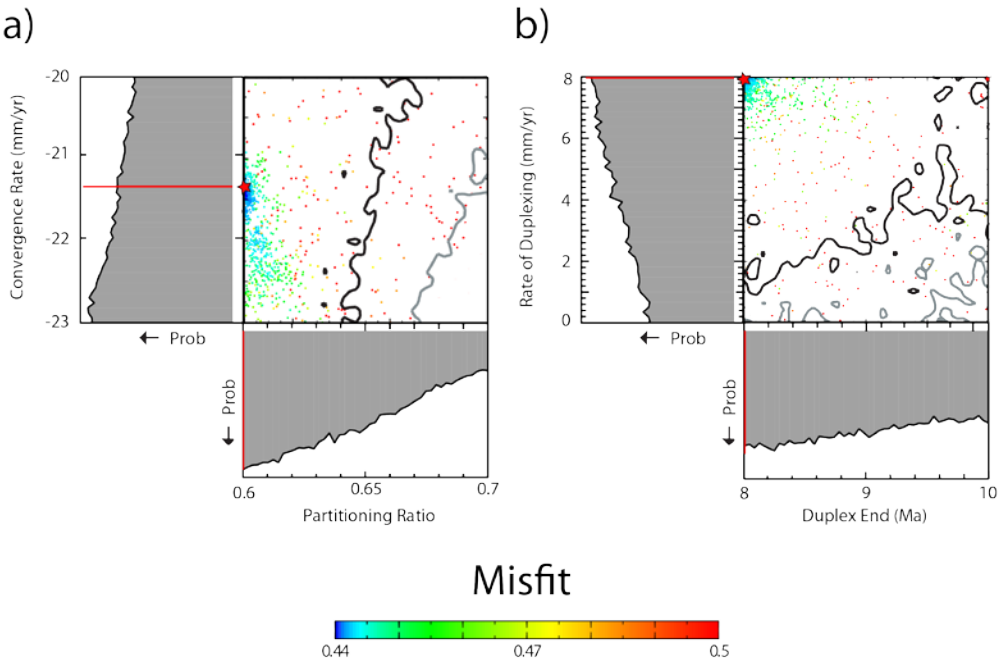

Figure 4.12: Inversion results for model SKI03 solving for four free parameters. Plot layout and symbols are the same as in Figure 4.6.

SKI03 Forward Model

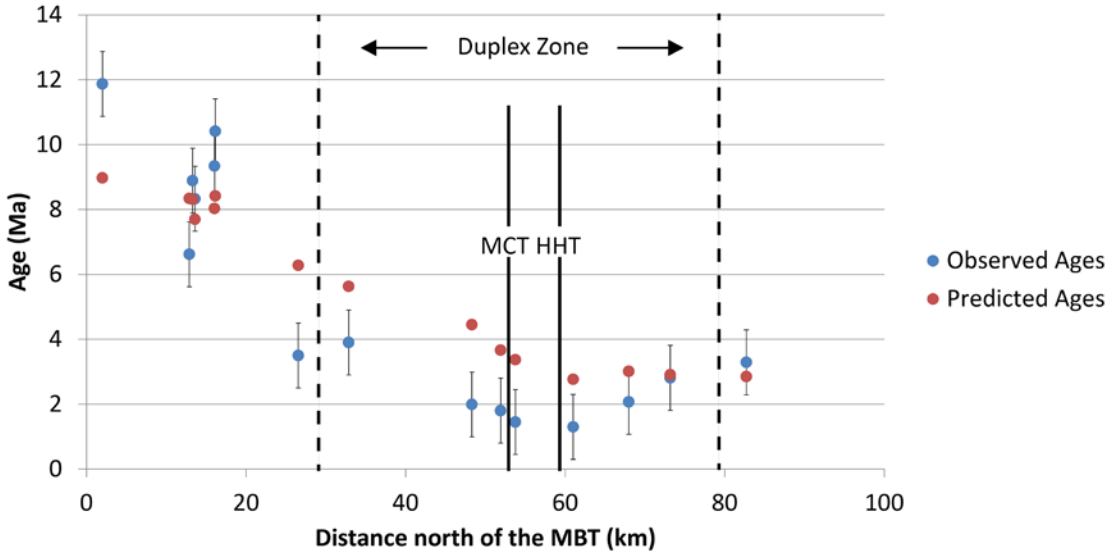

Figure 4.13: Observed cooling ages (blue) with associated 1 Ma error and predicted cooling ages (red) from the lowest misfit forward model from inversion SKI03 plotted against distance from the MBT. Black lines show the approximate locations of the MCT and HHT with respect to the samples on the transect, dashed black lines show the location of the inverted duplex zone boundaries.

Much like Inversion SKI01, the results of this model (Figure 4.13) show ages that are too old within the area of the duplex; a greater magnitude of exhumation within this zone appears to be required to resolve this, which suggests that duplexing needs to be active for a longer time period than 12-8 Ma or at a faster rate. The 8 mm/yr of uplift this model produced between 12-8 Ma creates clear distortions of the velocity and thermal fields (Figure 4.14).

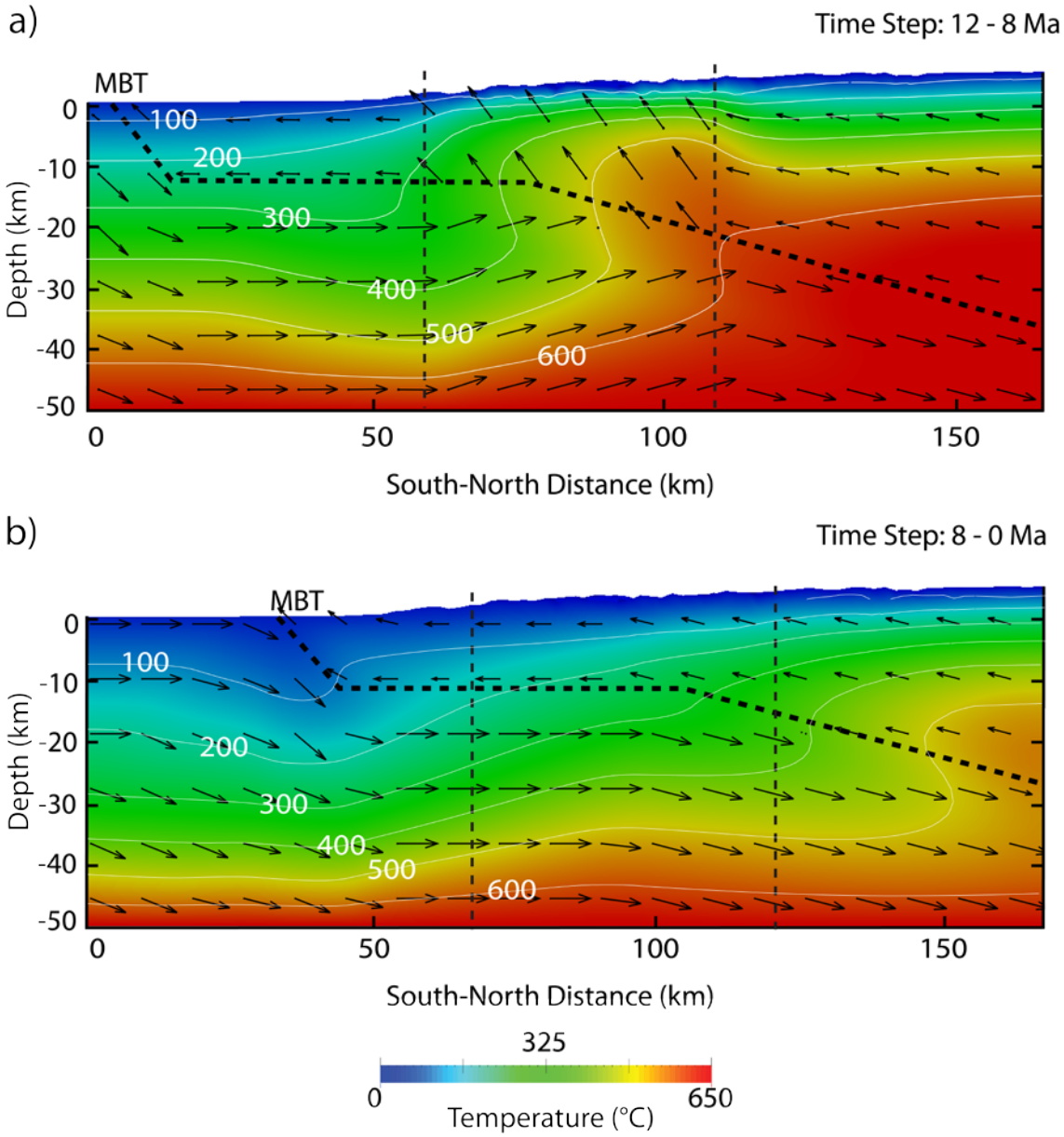

Figure 4.14: The thermal and velocity field for SKI03 shown in two time-steps to show the effects of the duplex zone over a period less than the 12 Ma model run. The boundaries of the duplex zone as defined by SKI02 are shown by the dashed black vertical lines. The location of the MBT/MHT is the same as in the previous models. a) Thermal and velocity field from 12 - 8 Ma during the time of duplex activity. There is a very clear disturbance visible in both the temperature field and the velocity field in the zone of duplexing. b) Thermal and velocity field from 8 - 0 Ma. 8 Ma after the duplex ceases uplift its effects are no longer visible on either the temperature or velocity field and the Figure looks similar to Figure 4.8.

SKI04 Inversion Results

A total of 8965 models were run for this inversion (Table 4.2; Figure 4.15) with minimum misfit of 0.33280, better than SKI03 but still not as good a fit to the data as SKI02. The convergence rate and partitioning ratio obtained from the lowest misfit model were a little higher than in SKI03 at 22.34 mm/yr and 0.63, respectively (Figure 4.15a). This inversion was given a larger range of duplex end-time values than in SKI03, allowing it to vary between 12 and 4 Ma and resulting in a lowest misfit value of 4 Ma (4.15b), once again at the younger edge of the range, as in SKI03. The lowest misfit value for the duplexing rate is 7 mm/yr (Figure 4.15b) which suggests a reasonable value since it is well within the data range and not at the edges of the value. As in SKI03, the 1-D PDFs show poorly defined parameter values with the exception of the duplex end time which shows a relatively steep increase in probability around the lowest misfit value (Figure 4.15b).

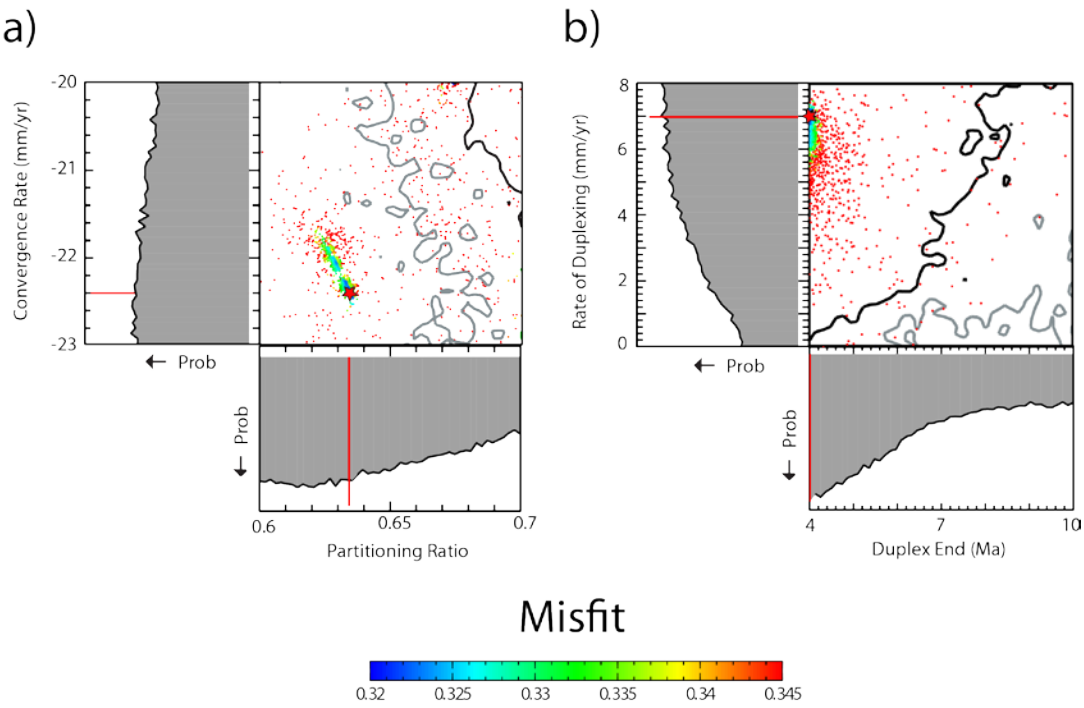

Figure 4.15: Inversion results for model SKI04 solving for four free parameters. Plot layout and symbols are the same as in Figure 4.6.

SKI04 Forward Model

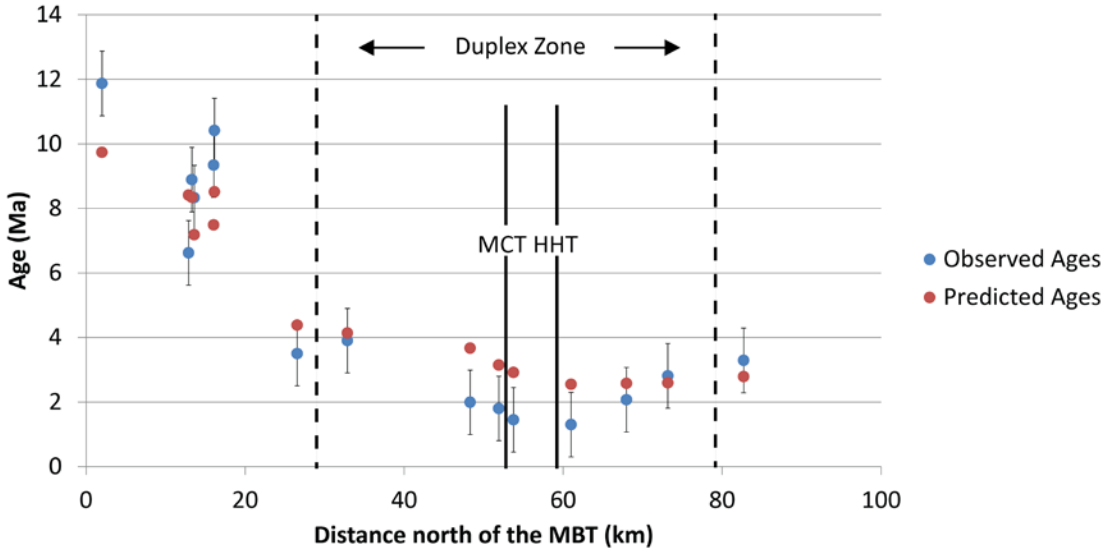

Figure 4.16: Observed cooling ages (blue) with associated 1 Ma error and predicted cooling ages (red) from the lowest misfit forward model from inversion SKI04 plotted against distance from the MBT. Black lines show the approximate locations of the MCT and HHT with respect to the samples on the transect, dashed black lines show the location of the inverted duplex zone boundaries.

The forward model age comparison (Figure 4.16) shows that, even with 8 Ma of duplexing at a relatively high rate of 7 mm/yr, the model has difficulty reproducing the younger ages in the center of the model without providing ages that are too young for the rest of the data. The thermal and velocity fields (Figure 4.17), which were once again split into two time frames of 12-4 Ma and 4-0 Ma, show significant vertical perturbations within the duplex zone during its active time frame (Figure 4.17a). However, within the 4 Ma that follows the thermal footprint of this perturbation is essentially erased by the influence of surface cooling (Figure 4.17b).

The results of SKI04 suggest that even 8 Ma of duplexing may not be enough to reproduce the age pattern seen at the surface today, even if the rate of duplexing is reasonable within the bounds of the model. From models SKI02, SKI03 and SKI04 it appears that the closer to present we allow the duplex to run, the better the modelled runs fit the data.

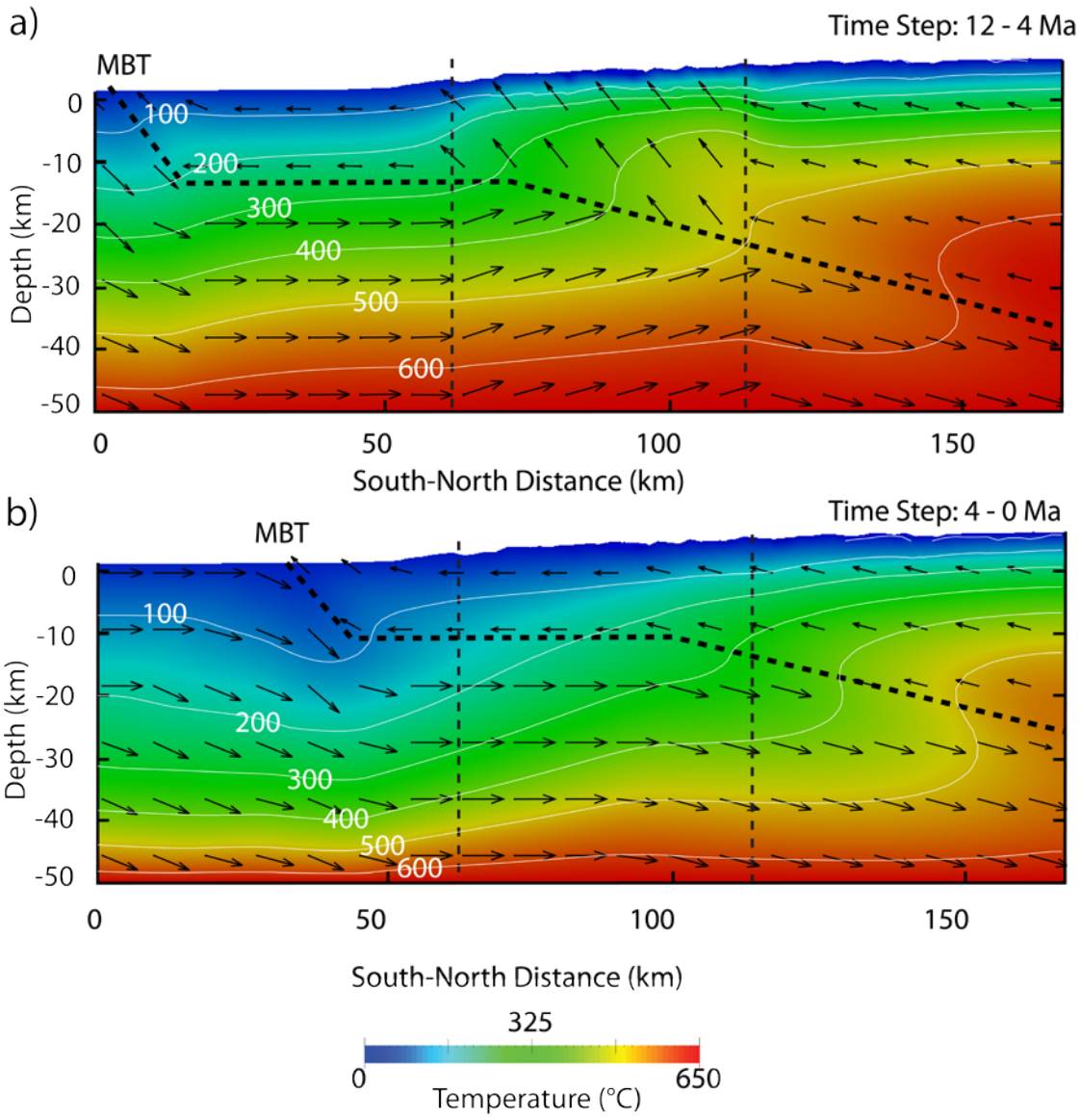

Figure 4.17: The thermal and velocity field for forward model SKI04 shown in two time-steps to illustrate the effects of the duplex zone over a period of time less than the 12 Ma model run. The boundaries of the duplex zone, as defined by inversion SKI02, are shown by the dashed black vertical lines. The location of the MBT/MHT is the same as in the previous models. a) Thermal and velocity field from 12 - 4 Ma during the time of duplex activity. There is again a very clear disturbance of both the temperature and the velocity fields in the zone of duplexing. b) Thermal and velocity field from 4 - 0 Ma. 4 Ma after the duplex ceases uplift its effects are no longer visible on either the temperature or velocity field and the Figure looks similar to Figure 4.8.

Chapter 5 – Discussion and Conclusions

The goal of this study was to use low temperature thermochronological data (ZHe) coupled with 3D thermokinematic modelling to test different scenarios regarding the tectonic evolution of the Sikkim Himalaya during the last 12 Ma. The observed ZHe cooling age pattern in Sikkim shows an abrupt decrease in ages coinciding with the southern boundary of the Rangit window and hypothesized duplex location in the subsurface (Figure 3.6). Cooling ages continue to get gradually younger northwards until the profile crosses the MCT and HHT into the GHS and the ages begin to increase gradually. In the following section I review the preferred tectonic models based on the goodness of fit with observed cooling age patterns and discuss possible limitations to the interpretations.

5.1 - Tectonic Models for the Sikkim Himalaya

The first tectonic model tested in inversion SKI01 involves only displacement on a geometrically variable MHT (Figure 4.8). While this inversion produced a predicted age pattern with an acceptably low misfit value (0.419), the model had difficulty reproducing the younger ages observed in the center of the transect within the Rangit/Tista windows (Figure 4.7). This observation suggests that thrust motion alone along the MHT is insufficient to advect crustal heat from depth to produce the observed age pattern and that, if we hold to the hypothesis that the cooling age pattern is primarily driven by tectonic processes, then there must be another tectonic mechanism at play.

The preferred model on the basis of the lowest misfit (0.236) is the tectonic scenario tested in inversion SKI02 which introduces a zone of enhanced uplift that

simulates the effects of a duplex (vertical accretion) in the upper crust beneath the Rangit/Tista windows, coupled with thrusting displacement on the MHT (Figure 4.11). The lowest-misfit model predicts an overthrusting rate of ~8 mm/yr along the MHT coupled with a rate of duplex-driven rock uplift of ~2.5 mm/yr from 12 Ma to present. The distribution of observed cooling ages is very well reproduced by predicted ages including the abrupt drop in cooling age within the duplex zone (Figure 4.10).

These results are comparable with the results obtained by Herman et al. (2010) for a duplex-related model in central Nepal. Their models yielded best-fit overthrusting rates of 4.4-6.8 mm/yr, which is slightly slower than the ~8 mm/yr predicted from my best fit model in Sikkim, and a duplex uplift rate of 3 ± 0.9 mm/yr, within error identical to the predicted rate of ~2.5 mm/yr. One of the major differences between my model and that of Herman et al. (2010) is the location of the duplex along the MHT. In this study, the duplex zone was placed based on the surface location of the Rangit/Tista windows, the zone that defines the abrupt drop in cooling age. This resulted in a duplex zone mostly located on a flat portion of the MHT (Figure 4.5). In contrast, Herman et al. (2010) placed the zone of localized rock uplift entirely on a ramp section of the MHT (Figure 15b in Herman et al., 2010). The interpretive cross-section of the duplex in Sikkim produced by Bhattacharrya and Mitra (2009) includes a small crustal ramp within the zone of duplexing (Figure 2.2) which may have added an increased vertical velocity gradient to help produce the antiformal stacks in the Rangit Duplex. This ramp is not imaged on the geophysical data used to define the geometry of the MHT, likely because it is small compared to the two major ramps on the MHT, so it was not included in the

models. In the cross section from Mitra et al. (2010) the ramp drops down ~ 2km, less than the 4 km vertical resolution on that section of the MHT in the geophysical data (Acton et al. 2011), over a horizontal distance of ~4 km, resulting in a dip angle of ~27 ° (Figure 2.2). However, the excellent fit of the predicted ages of SKI02 to the observed cooling pattern, especially in the duplex zone, suggests that the small ramp may have played a role in the construction of the duplex.

The two models that we have run to explore an early end of duplexing (SKI03 and SKI04) both resulted in unrealistically high duplex uplift rates (7-8 mm/yr) and larger misfit values (0.323 - 0.446) compared to the best fit model.

5.2 - Modelled Exhumation Rates

Both the instantaneous exhumation rate over the transect length and the average exhumation rate for each sample over the 12 Ma model interval were produced from the T-t-paths calculated during the model run (Figure 5.1a). The instantaneous exhumation rate, which corresponds to the near-surface vertical component of the velocity field, shows the highest exhumation rates near the active MBT (~7 mm/yr) and near the MCT/HHT (~5 mm/yr) because of the presence of crustal ramps in the subsurface that locally produce an increased vertical velocity component. The vertical accretion related to duplexing combines with that effect to maintain relatively high instantaneous exhumation rates of 2.5 mm/yr above the long flat segment of the MHT. The average exhumation rate (Figure 5.1a) for each sample is the amount of exhumation between the depth at which the particle passes through its effective closure temperature isotherm and the surface position of the sample, divided by the age of the

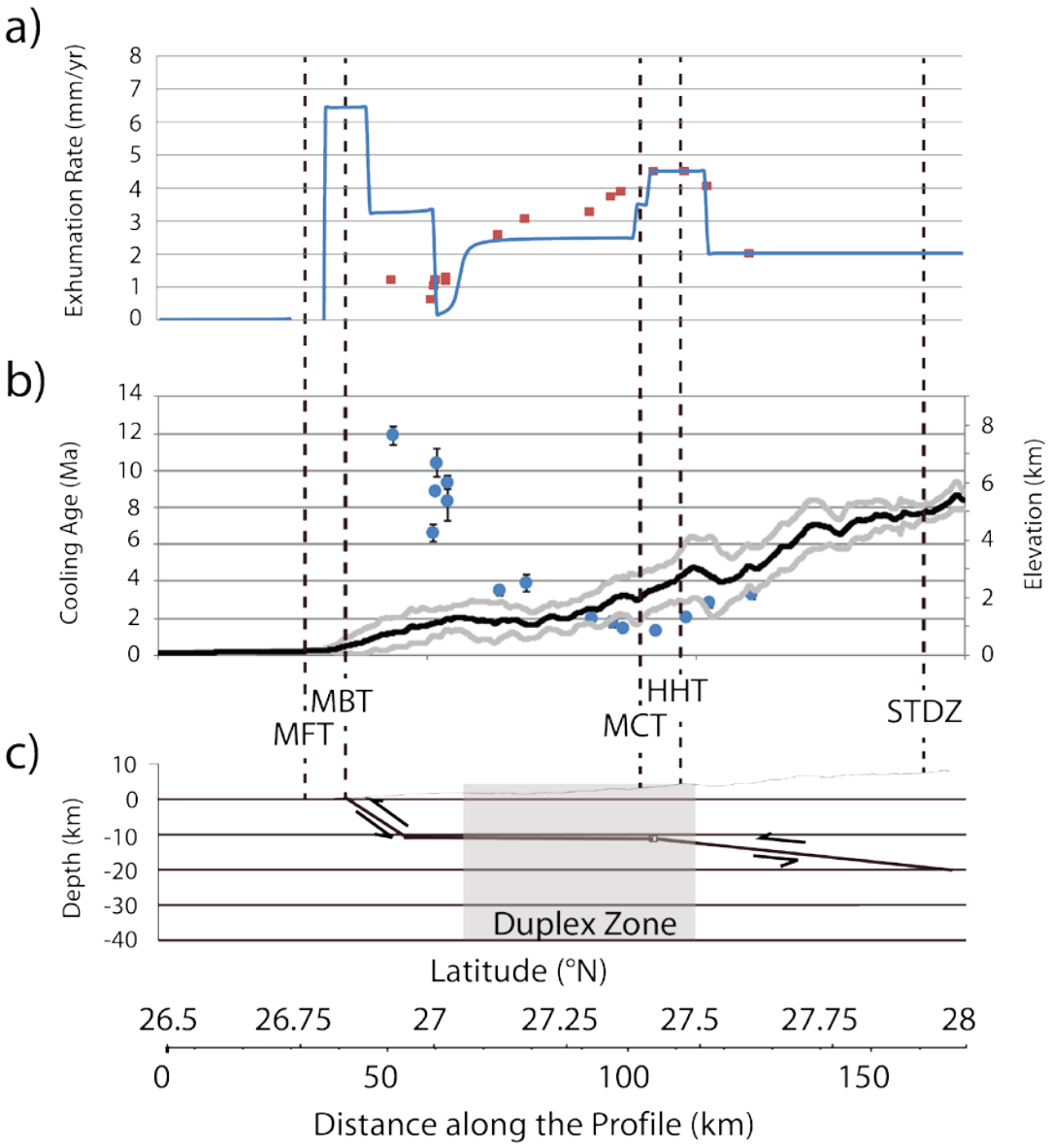

Figure 5.1: a) Instantaneous exhumation rate (blue line) within the model domain and average exhumation rate (red squares) experienced by each sample. b) Observed ZHe cooling ages (blue circles) with 1σ error plotted with average elevation (black solid line) and 1σ error (grey solid lines). Topographic profile is constructed from a DEM of Sikkim between 26.5 °N - 28 °N and 88 °E - 89 °E assembled from SRTM-90 m data (http://srtm.csi.cgiar.org/). c) Best fit tectonic model (SKI02) for Sikkim showing the geometry of the MHT and the area experiencing duplexing (grey transparent rectangle). All figures share the same x-axis. Major structures are denoted by the vertical dashed black lines.

sample (c.f., Figure 6b in Coutand et al., 2014). Average exhumation rates range between 0.6-4.6 mm/yr. The pattern of average exhumation rates approximates a mirror image of the pattern of cooling ages (Figure 5.1b), which is expected since a higher exhumation rate (or cooling rate) should produce younger ages.

The *Pecube* models do not include the effects of surface processes because the models are not coupled with a landscape-evolution model and topographic steady-state has been assumed here. The rationale for this choice is that we have noticed that the cooling ages do not correlate with the topography (Figures 3.7 and 5.1b). When plotted along the topographic swath profile (Figure 5.1b), cooling ages get younger as elevation increases until ~27.4 °N where the opposite occurs and cooling ages increase with increasing elevation. These patterns are quite inconsistent as the largest change in elevation occurs over a relatively flat section of the profile between 27-27.5 °N. When the cooling ages are plotted directly against sample elevation (Figure 3.7), there is no correlation between the two. This suggests that the modern topography, and by extension surface processes, may not have exerted a major control on the distribution of cooling ages along the range and that the distribution is more likely controlled by tectonic effects.

5.3 - Comparison of Models along Strike of the Orogen

We compared our results to applications of the same approach as ours in Nepal, eastern Bhutan and Arunachal Pradesh (Figure 5.2).

The westernmost transect (Figure 5.2A; Whipp et al., 2007) shows AFT ages between 28 °N and 29°N within the Marsyandi Valley in central Nepal and surrounding

tributary valleys. The ages are all younger than 4 Ma and do not show any noticeable trend along the main transect except that young ages (< 0.5 Ma) tend to occur at low elevations near rivers (Whipp et al., 2007). In this study, two tectonic scenarios were tested, one involving a simple displacement on the MHT over the past 20 Ma and a second involving out-of-sequence thrusting (reactivation) of the MCT as well as motion along the MHT, both active for 20 Ma. They found that the AFT data alone could not distinguish between the two model types during the last ~3 Ma because models both with and without the out-of-sequence MCT produced predicted cooling ages that fit the observed data equally well within error. No single model was able to reproduce >80% of the cooling age data which was suggested to be a result of a non-uniform erosion rate over the model area. Modelling of ten shorter age transects within individual valleys located within the larger study area produced exhumation rates of 1.8–5.0 mm/yr which also suggests a variable erosion rate. The Marsyandi valley seems to be an unusual place in the Himalaya, since there is no other place where such consistently young AFT ages have been identified to date.

Transect B (Figure 5.2B) shows AFT ages from the Langtang Transect from Robert et al. (2011). The general trend shows that the youngest ages are located north of the MCT in the MCTZ (< 4 Ma) with a gradual increase southwards to a maximum of ~9 Ma just north of the MBT. No significant offset in cooling ages is observed as the profile crosses the MCT, suggesting that the structure was no longer active at the time these samples crossed the effective closure temperature for the AFT chronometer. As for Whipp et al. (2007), the tectonic scenarios tested could not distinguish between models

with or without out-of-sequence thrusting within error of the AFT data and the range of thermal and kinematic parameters used because both scenarios produced models with comparably good fits to the data. They found, however that, in order for the out-of-sequence model to provide a good fit to their data, the MCT could only have been re-activated in the Quaternary. If that is true, then they conclude that their AFT dataset is too old to constrain the timing of the MCT reactivation.

Transect C from Herman et al., 2010 (Figure 5.2C) is the easternmost transect in Nepal and it used a large dataset (> 100 ages) of $^{40}Ar/^{39}Ar$ muscovite data combined with a small set of AFT and ZHe samples. Even though the $^{40}Ar/^{39}Ar$ system has a higher closure temperature than AFT (350-400 °C versus ~120 °C) the same trend in the ages is observed as in Transect B (Figure 5.2B). The youngest $^{40}Ar/^{39}Ar$ ages are located north of the MCT in the MCTZ with no significant decrease in age when crossing the MCT. South of the MCT, the ages show a linear increase from ~5 Ma to > 20 Ma. The AFT ages show a similar trend and although the data are sparse within the LHS the ages follow the same general pattern as in Robert et al. (2011). The ZHe ages were only in a single cluster in the southern end of the age profile and did not show a pattern at the scale of this transect. In this study, models exploring both out-of-sequence thrusting and underplating related to duplexing were run over a period of 10 Ma. Both models produced a predicted age pattern that fit the observed ages very well, suggesting that even with a very large dataset, it is difficult to discriminate between the effects of out-of-sequence faulting on the MCT and duplexing in its footwall using thermochronometer

data alone. In this case the duplex model was preferred because the best-fit out-of-sequence model required an unrealistically high slip rate on the MCT (>18 mm/yr).

Transect D is from this study (Figure 5.2D). The general cooling age pattern has a lot in common with the patterns seen in the data from Herman et al. (2010) and Robert et al. (2011); the youngest ZHe age in Sikkim (1.3 ± 0.07 Ma) occurs in the GHS just north of the MCTZ and the ages increase towards the south into the LHS to a maximum of 11.87 ± 0.49 Ma just north of the MBT. Ages north of the MCTZ also gradually increase north into the GHS. The Sikkim transect differs from the Nepalese transects in that it has a more distinct and drastic drop in ages north of the MBT correlating with the surface location of the Rangit and Tista windows. The best fit model suggests there has been underplating as a result of duplexing within the LHS, coupled with slip along the MHT (Figure 4.10).

Transects E and F show the western and eastern Bhutan transects from Coutand et al. (2014) (Figures 5.2E & F) where data from four low temperature thermochronometers (AHe, AFT, ZHe and ZFT) were used. The cooling age pattern in the western transect (Figure 5.2E) shows all chronometers generally increasing in age in the LHS towards the north across the MCT to ~27°15' N where ages begin to decrease across the GHS until ~27°45' N where they increase again toward the STDZ. The cooling age pattern in eastern Bhutan (Figure 5.2F) is very similar to that in western Bhutan with an abrupt increase in age at the start of the transect until ~27 °N, north of the MCTs, where the ages begin to decrease until just north of the MCTn where they begin to increase again. These patterns are nearly the opposite of what is seen in Sikkim and

further west in Nepal where ages in the LHS decrease towards the MCT and then increase to the north of it. Both transects produced models that fit the data well over the past 12 Ma using only an MHT with variable geometry and no additional structures such as duplexing or out-of-sequence faulting.

Transect G shows the data and best fit model from Adlakha et al. (2013) in Arunachal Pradesh (Figure 5.2G). Here, AFT and ZFT samples were used in order to discriminate whether out-of-sequence faulting played a role in the tectonic development of Bhutan. The general AFT pattern is similar to that found in the transects from Coutand et al. (2014) showing an increase in cooling age to the north from 20 km south of the MCT followed by a decrease north of the MCT, through the GHS and a klippe of TSS, until the end of the transect. The ZHe pattern is nearly identical except there is no initial rise in ages to the south, only a smooth decline in ages north through the transect. Three models were tested to attempt to reproduce the cooling age patterns: one with only slip along the MHT, one with an out-of-sequence MCT active at the beginning of the model and a third with a delayed onset of MCT re-activation. While all models showed a generally good fit to the data, the best fit model was the delayed re-activation model favoring an out-of-sequence MCT active between 6.5 Ma and 8.5 Ma.

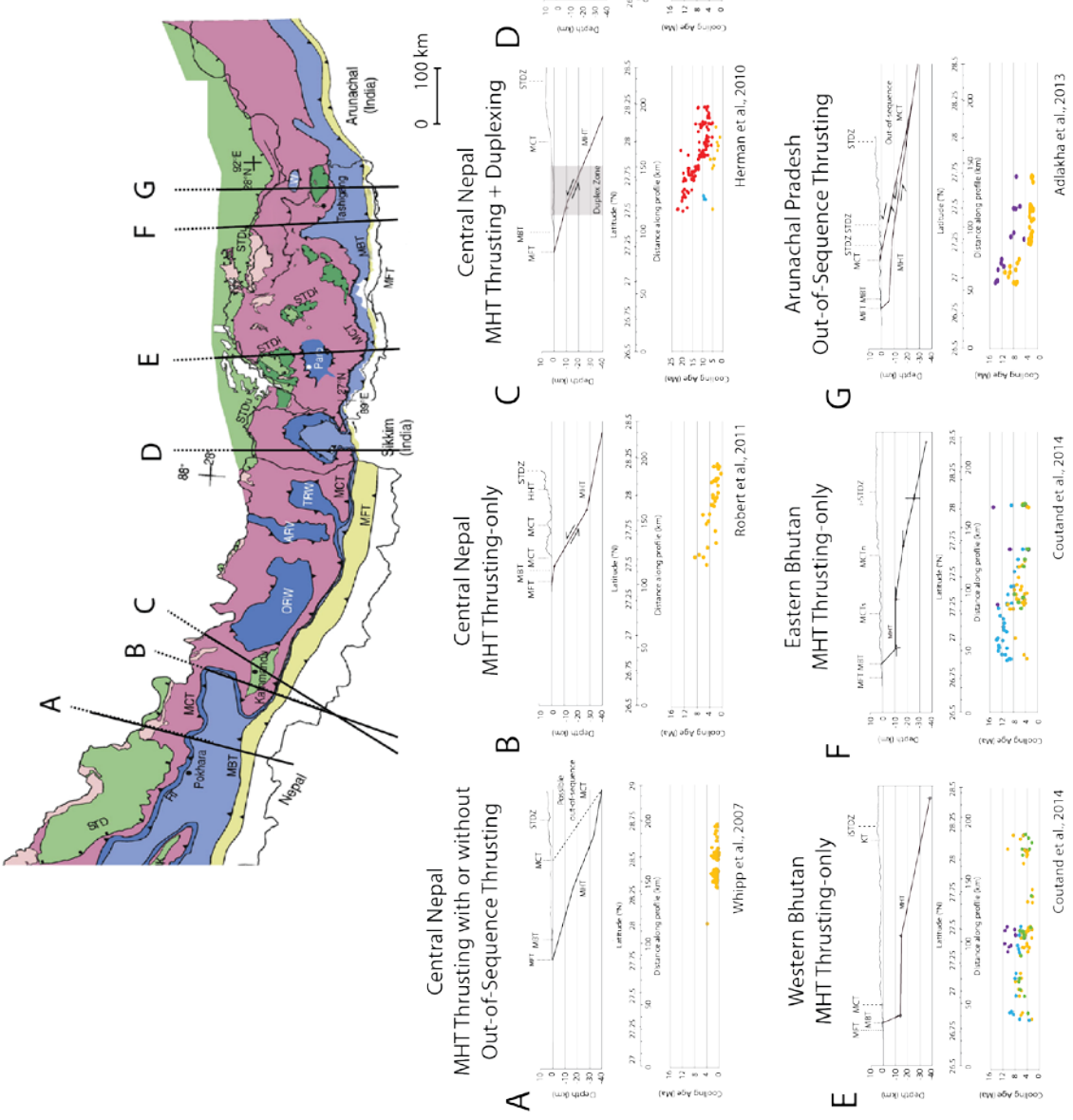

Figure 5.2: Compilation of low temperature thermochronology data and tectonic models across the central and eastern Himalaya showing seven transects. From west to east: A) Whipp et al., 2007, B) Robert et al., 2011, C) Herman et al., 2010, D) this study, E) Coutand et al., 2014, F) Coutand et al., 2014 and G) Adlakha et al., 2013. Map from McQuarrie et al., 2008.

The results of Adlakha et al. (2013) differ from the rest of the studies listed as they are based on forward models only (560 total over 3 model scenarios) compared to the inversions used elsewhere which run thousands or tens of thousands of models so that a larger parameter space can be searched iteratively for ideal parameter values. In addition, no out-of-sequence faulting has been observed in Arunachal Pradesh or Bhutan to the west. The inclusion of an out-of-sequence fault was done in order to compare with the studies of Herman et al. (2010) and Robert et al. (2011). The lack of a formal inversion of the data and more importantly, of field evidence for out-of-sequence faulting within the study area, suggests that these results may have limited value.

These studies show that thermochronometer cooling age patterns are not laterally consistent along the Himalaya. In the above transects, the cooling age pattern changes between Sikkim and Bhutan. To the west, Sikkim and Nepal in general show cooling age patterns that have the oldest ages just north of the MBT followed by a decrease in age northwards across the LHS and MCT and into the southern GHS where ages begin to slowly rise again (Figure 5.2a - d. To the east in Bhutan and Arunachal Pradesh the cooling ages rise within the LHS to the oldest ages either within the upper LHS (for western Bhutan and Arunachal Pradesh) or across the MCT and into the GHS (for eastern Bhutan) where the cooling ages gradually decrease northwards. The cooling ages only begin to rise again within the northern GHS approaching the STDZ (Figure 5.2e - g). In most cases the age trends cross the MCT without any noticeable offset. The tectonic models proposed also differ along strike; however in some cases the best fit model is only the best of several good fit models and may not be statistically much

better than the alternatives as is the case for the out-of-sequence thrusting model of Adlakha et al. (2013). In other cases, some models did not include specific processes (i.e. duplexing or out-of-sequence thrusting) because they were not observed in the study areas. In the case of Coutand et al. (2014), there is no evidence of out-of-sequence faulting of the MCT in Bhutan so this component was not included in the models. Duplexing in Bhutan is suggested to have ceased by 9 Ma and 10.5 Ma in western and eastern Bhutan, respectively, near the beginning of the model so it would only have had a short lived effect on the oldest ZHe and ZFT ages. Models including duplexing were tested but resulted in negligible rates of duplexing since the ages were already very well replicated using only displacement along the MHT alone.

There are several possible reasons for the variations in cooling age pattern across the orogen. One possible source of variability may be type of structures present within the subsurface and the amount of shortening they have accommodated within the LHS and GHS along the orogen. Mitra et al. (2010) compiled shortening amounts across the Himalaya from the MBT to the STDZ and showed pattern of decreasing shortening from central Nepal towards the east. With the exception of Central Nepal, the amount of shortening attributed to the LHS duplex also decreases from central Nepal to Bhutan. The increased duplex-driven shortening in the west may be the cause of the generally younger ages within the LHS in the west compared to the east. Specifically considering the transition between Sikkim and Bhutan, there is a large strike-perpendicular structure called the Yadong cross-structure this is suggested from earthquake data to have a left-lateral strike-slip motion and has been observed to be offset by ~70 km. This amount of

slip may have had consequences for the along strike continuity of the majors structures between Sikkim and Bhutan, such as the MCT, and maybe have influenced a difference in structural locations in the higher Himalaya. The cross-structure is currently the largest orogen-transverse structure within the higher Himalaya along the entire Himalayan chain (Wu et al., 2010), is known from seismic imaging to be a relatively deep seated structure (~43 km) and may be a cause of cooling age variations between the two areas. Variations in erosion rate may also be a factor in the variation in cooling ages along strike despite the model assumption of steady state erosion within Sikkim. Bookhagen and Burbank (2010) showed that while the total amount of rainfall along strike remains nearly constant, spatially the distribution of rainfall is primarily controlled by high topography. Areas with two step topography, such as Nepal and Sikkim (Figure blah), will show two major rainfall bands of high intensity correlating with area of high relief and the outcropping of more resistant GHS rocks. Bhutan, on the other hand, with its single step topography only gets a single large band of high intensity rainfall that falls in the south near the boundary of the GHS, which extends further south and as a more complete package compared to the GHS to the west. These local variations in erosion could be reason for the variation of cooling ages along strike.

5.4 - Limitations of the Models

The models predict cooling ages based on the kinematics of structures within a brittle regime in which all exhumation is accommodated along discrete structures such as faults or duplexes. However, a recent study (Bose et al., 2014) suggests that the formation of the now eroded LHS “dome” which is exposed in the Rangit/Tista windows

required both brittle and ductile deformation to produce the structure observed today. They performed analogue modelling experiments that suggested that overthrusting on a discrete structural ramp cannot alone produce the antiformal stacks found within the model of Bhattacharrya and Mitra (2009). Instead, based on field measurements of multiples episodes of folding, they suggest that the growth of the Rangit/Tista windows progressed through four episodes of superimposed buckling. Simulation of ductile deformation is possible in *Pecube*, however simulating four episodes of buckling would be complex and the kinematic velocity field would be extremely difficult to define.

In Sikkim, two major rivers, the Rangit and the Tista, flow through their respectively named windows and have produced deep river valleys. The rivers are fed not only by the upstream melting of the glaciers during the thaw season, but also by the significant rainfall brought on during the yearly Indian Summer Monsoon. Sikkim receives ≥ 2-4 m/yr precipitation from the monsoon (c.f., Figure 4A in Bookhagen and Burbank, 2010) which should increase localized incision rates and erosion. Furthermore, it has been suggested that the monsoon has been consistently active since 12-10.7 Ma (Dettman et al., 2001; 2003), essentially the entire duration of the models. If the erosion derived from monsoonal precipitation proves significant, it would become a source of error in the results. These effects were not taken into account in the modelling as *Pecube* alone currently does not simulate surface processes such as river incision and needs to be coupled with landscape-evolution models, which was beyond the scope of this study.

5.5 - Tectonic History of Sikkim

Figure 5.3 shows a simplified interpretive tectonic history of Sikkim based on the results of the best fit model and other published data.

Before ~12 Ma (Figure 5.3a) ductile deformation was the dominant tectonic process in Sikkim. The GHS was extruded from underneath Tibet between the opposite sense STDZ and MCT as a mid-crustal channel (e.g., Beaumont et al., 2001; 2004; Grujic et al., 2002; Godin et al., 2006). The TSS extended further south than its current position and was likely in contact with the LHS at the surface to the south. At 10-12 Ma (Figure 5.3b), when our models began, the MCT had become inactive in Sikkim (e.g., Harris et al., 2004; Catlos et al., 2004) after transporting the GHS nappe southwards above the LHS. Channel flow had ceased (e.g., Grujic et al., 2011) and convergence accommodation of Himalayan convergence shifted southwards to the RT which stacked the northern Daling duplex units on top of upper LHS units to the south.

By 10 Ma the MHT had shifted northwards again, breaking the surface south of the LHS as the MBT. As motion along the new MHT/MBT continued, underplating of material caused by the imbrication of LHS slices above a crustal ramp, initiating the Daling duplex. As material is thrust over the ramp, the LHS slices continued to stack due to the increased vertical velocity field forming the antiformal stacks of the Rangit duplex and shortening the LHS considerably (Figure 5.3c; Bhattacharrya and Mitra, 2009; Mitra et al., 2010). To the south, the GHS nappe was eroded, exposing the LHS units of the Rangit and Tista windows and leaving only a small klippe of high-grade rocks south of

the LHS. The MBT likely became inactive in the Quaternary when the MFT, the current toe of the Himalayan wedge, was activated.

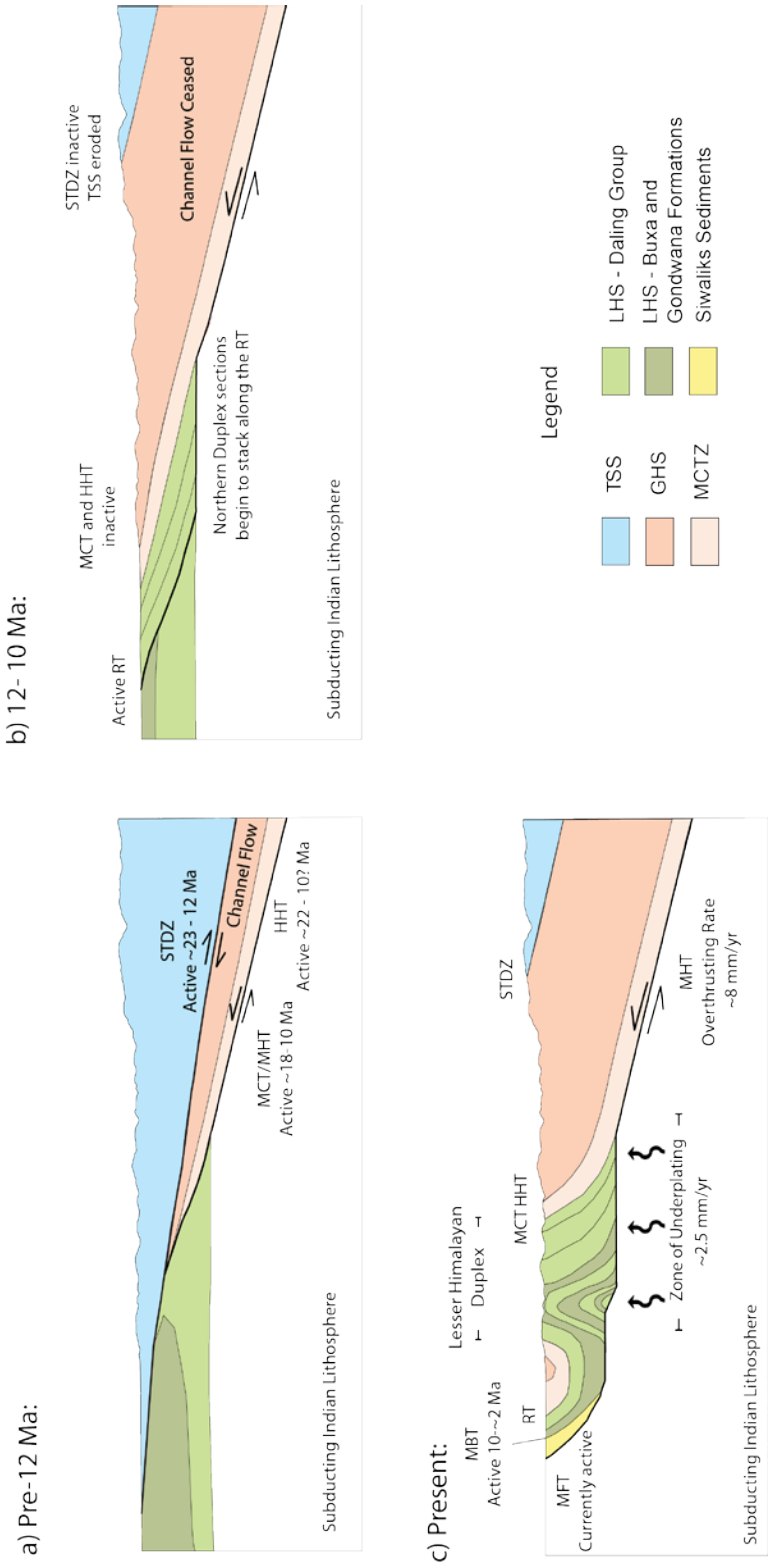

Figure 5.3: A simplified schematic model showing the proposed tectonic evolution of Sikkim in three stages. Thick black lines show the active structures during each stage. a) Pre-model conditions dominated by ductile deformation (channel flow), b) conditions at the beginning of the model with convergence being transferred from the MCT to the RT and then to the MBT and the beginning of duplexing, and c) present day tectonic configuration. Modified from Mitra et al., 2010.

5.6 - Conclusions

Across the Himalayan range front in Sikkim, the analysis of 15 new zircon (U-Th)/He *in situ* bedrock samples, combined with 3D thermokinematic modelling allowed us to draw the following conclusions:

1) The samples collected produced cooling ages ranging from 1.30 ± 0.07 Ma to 11.87 ± 0.49 Ma. The NS-trending cooling age profile shows that the oldest ages, located immediately north of the MBT, record an abrupt decrease northwards, near the southern boundary of the Rangit/Tista window with ages beginning to slightly increase again north of the MCTZ.
2) Age trends do not correlate with modern topography suggesting that tectonic processes are the dominant control on the cooling age pattern.
3) Inversion results for the first scenario (SKI01) suggest that thrust motion of the MHT alone is unable to reproduce the observed cooling age pattern to an acceptable degree and thus cannot be the sole structural control on the tectonic development of the Sikkim range front during the last 12 Ma.
4) In the second scenario, the addition of a ~ 50 km long zone of enhanced vertical uplift active for 12 Ma at 2.5 mm/yr, coupled with a MHT overthrusting rate of ~8 mm/yr, results in a predicted age pattern that is nearly identical to the observed age pattern.

5) The proposed tectonic model for the development of Sikkim during the last 12 Ma includes convergence accommodated by a basal thrust with a ramp-and-flat geometry coupled with a localized zone of accretion, active for the past 12 Ma, simulating rock uplift associated with the development of a duplex system within the Lesser Himalaya.

References

Acharyya, S. K., & Ray, K. K. (1977). Geology of the Darjeeling–Sikkim Himalaya. Guide to Excursion No. 3. In *Fourth International Gondwana Symposium (Calcutta). Geological Survey of India* (pp. 1-25).

Acton, C. E., Priestley, K., Mitra, S., & Gaur, V. K. (2011). Crustal structure of the Darjeeling-Sikkim Himalaya and southern Tibet. *Geophysical Journal International*, *184*(2), 829-852.

Adlakha, V., Lang, K. A., Patel, R. C., Lal, N., & Huntington, K. W. (2013). Rapid long-term erosion in the rain shadow of the Shillong Plateau, Eastern Himalaya.*Tectonophysics*, *582*, 76-83.

Alsdorf, D., Makovsky, Y., Zhao, W., Brown, L. D., Nelson, K. D., Klemperer, S., ... & Kuo, J. (1998). INDEPTH (International Deep Profiling of Tibet and the Himalaya: multichannel seismic reflection data: description and availability. .*Journal of Geophysical Research: Solid Earth (1978–2012)*, *103*(B11), 26993-26999.

Attendorn, H. G., & Bowen, R. (1988). *Isotopes in the earth sciences*. Springer. (p.109).

Avouac, J. P. (2003). Mountain building, erosion, and the seismic cycle in the Nepal Himalaya. *Advances in Geophysics*, *46*, 1-80.

Banerjee, P., Bürgmann, R., Nagarajan, B., & Apel, E. (2008). Intraplate deformation of the Indian subcontinent. *Geophysical Research Letters*, *35*(18).

Beardsmore, G. R., & Cull, J. P. (2001). *Crustal heat flow: a guide to measurement and modelling*. Cambridge University Press, 23-24.

Beaumont, C., Jamieson, R. A., Nguyen, M. H., & Lee, B. (2001). Himalayan tectonics explained by extrusion of a low-viscosity crustal channel coupled to focused surface denudation. *Nature*, *414*(6865), 738-742.

Beaumont, C., Jamieson, R. A., Nguyen, M. H., & Medvedev, S. (2004). Crustal channel flows: 1. Numerical models with applications to the tectonics of the Himalayan-Tibetan orogen. *Journal of Geophysical Research: Solid Earth (1978–2012)*, *109*(B6).

Berger, A., Jouanne, F., Hassani, R., & Mugnier, J. L. (2004). Modelling the spatial distribution of present-day deformation in Nepal: how cylindrical is the Main Himalayan Thrust in Nepal?. *Geophysical Journal International*, *156*(1), 94-114.

Berthet, T., Ritz, J. F., Ferry, M., Pelgay, P., Cattin, R., Drukpa, D., ... & Hetényi, G. (2014). Active tectonics of the eastern Himalaya: New constraints from the first tectonic geomorphology study in southern Bhutan. *Geology*, *42*(5), 427-430.

Besse, J., Courtillot, V., Pozzi, J. P., Westphal, M., & Zhou, Y. X. (1984). Palaeomagnetic estimates of crustal shortening in the Himalayan thrusts and Zangbo suture.

Bettinelli, P., Avouac, J. P., Flouzat, M., Jouanne, F., Bollinger, L., Willis, P., & Chitrakar, G. R. (2006). Plate motion of India and interseismic strain in the Nepal Himalaya from GPS and DORIS measurements. *Journal of Geodesy*,*80*(8-11), 567-589.

Bhattacharyya, K., & Mitra, G. (2009). A new kinematic evolutionary model for the growth of a duplex—an example from the Rangit duplex, Sikkim Himalaya, India. *Gondwana Research*, *16*(3), 697-715.

Bilham, R., Larson, K., Freymueller, J., Jouanne, F., LeFort, P., Leturmy, P., ... & de Voogd, B. (1997). GPS measurements of present-day convergence across the Nepal Himalaya. *Nature*, *386*(6620), 61-64.

Bollinger, L., Avouac, J. P., Beyssac, O., Catlos, E. J., Harrison, T. M., Grove, M., ... & Sapkota, S. (2004). Thermal structure and exhumation history of the Lesser Himalaya in central Nepal. *Tectonics*, *23*(5).

Bollinger, L., Henry, P., & Avouac, J. P. (2006). Mountain building in the Nepal Himalaya: Thermal and kinematic model. *Earth and Planetary Science Letters*, *244*(1), 58-71.

Bookhagen, B., & Burbank, D. W. (2010). Toward a complete Himalayan hydrological budget: Spatiotemporal distribution of snowmelt and rainfall and their impact on river discharge. *Journal of Geophysical Research: Earth Surface (2003–2012)*, *115*(F3).

Bose, S., Mandal, N., Acharyya, S. K., Ghosh, S., & Saha, P. (2014). Orogen-transverse tectonic window in the Eastern Himalayan fold belt: A superposed buckling model. *Journal of Structural Geology*, *66*, 24-41.

Braun, J. (2002). Quantifying the effect of recent relief changes on age–elevation relationships. *Earth and Planetary Science Letters*, *200*(3), 331-343.

Braun, J. (2003). *Pecube*: A new finite-element code to solve the 3D heat transport equation including the effects of a time-varying, finite amplitude surface topography. *Computers & Geosciences*, *29*(6), 787-794.

Braun, J. (2005). Quantitative constraints on the rate of landform evolution derived from low-temperature thermochronology. *Reviews in Mineralogy and Geochemistry*, *58*(1), 351-374.

Braun, Jean; Peter van der Beek; Geoffrey Batt (2006). *Quantitative Thermochronology: Numerical Methods for the Interpretation of Thermochronological Data*. Cambridge: Cambridge University Press. pp. 24–27

Braun, J., Van Der Beek, P., Valla, P., Robert, X., Herman, F., Glotzbach, C., ... & Prigent, C. (2012). Quantifying rates of landscape evolution and tectonic processes by thermochronology and numerical Modelling of crustal heat transport using *PECUBE*. *Tectonophysics*, *524*, 1-28.

Burbank, D. W., Leland, J., Fielding, E., Anderson, R. S., Brozovic, N., Reid, M. R., & Duncan, C. (1996). Bedrock incision, rock uplift and threshold hillslopes in the northwestern Himalayas. *Nature*, *379*(6565), 505-510.

Burchfiel, B. C., & Royden, L. H. (1985). North-south extension within the convergent Himalayan region. *Geology*, *13*(10), 679-682.

Burchfiel, B. C., Zhiliang, C., Hodges, K. V., Yuping, L., Royden, L. H., Changrong, D., & Jiene, X. (1992). The South Tibetan detachment system, Himalayan orogen: Extension contemporaneous with and parallel to shortening in a collisional mountain belt. *Geological Society of America Special Papers*, *269*, 1-41.

Burg, J. P., & Chen, G. M. (1984). Tectonics and structural zonation of southern Tibet, China.

Burg, J. P., Nievergelt, P., Oberli, F., Seward, D., Davy, P., Maurin, J. C., ... & Meier, M. (1998). The Namche Barwa syntaxis: evidence for exhumation related to compressional crustal folding. *Journal of Asian Earth Sciences*, *16*(2), 239-252.

Catlos, E. J., Dubey, C. S., Harrison, T. M., & Edwards, M. A. (2004). Late Miocene movement within the Himalayan Main Central Thrust shear zone, Sikkim, north-east India. *Journal of Metamorphic geology*, *22*(3), 207-226.

Catlos, E. J., Dubey, C. S., Marston, R. A., & Harrison, T. M. (2007). Geochronologic constraints across the main central thrust shear zone, Bhagirathi River (NW India): Implications for Himalayan tectonics. *Geological Society of America Special Papers*, *419*, 135-151.

Clark, M. K. (2012). Continental collision slowing due to viscous mantle lithosphere rather than topography. *Nature*, *483*(7387), 74-77.

Consultative Group on International Agricultural Research - Consortium for Spatial Information (CGIAR-CSI) - (http://srtm.csi.cgiar.org/).

Coutand, I., Whipp, D. M., Grujic, D., Bernet, M., Fellin, M. G., Bookhagen, B., ... & Duncan, C. (2014). Geometry and kinematics of the Main Himalayan Thrust and Neogene crustal exhumation in the Bhutanese Himalaya derived from inversion of multithermochronologic data. *Journal of Geophysical Research: Solid Earth*, *119*(2), 1446-1481.

Dahlen, F. A. (1990). Critical taper model of fold-and-thrust belts and accretionary wedges. *Annual Review of Earth and Planetary Sciences*, *18*, 55.

Daniel, C. G., Hollister, L. S., Parrish, R. T., & Grujic, D. (2003). Exhumation of the Main Central Thrust from lower crustal depths, eastern Bhutan Himalaya. *Journal of Metamorphic Geology*, *21*(4), 317-334.

Dasgupta, S., Ganguly, J., & Neogi, S. (2004). Inverted metamorphic sequence in the Sikkim Himalayas: crystallization history, P–T gradient and implications. *Journal of Metamorphic Geology*, *22*(5), 395-412.

Dasgupta, S., Chakraborty, S., & Neogi, S. (2009). Petrology of an inverted Barrovian sequence of metapelites in Sikkim Himalaya, India: constraints on the tectonics of inversion. *American Journal of Science*, *309*(1), 43-84.

Davis, D., Suppe, J., & Dahlen, F. A. (1983). Mechanics of fold-and-thrust belts and accretionary wedges. *Journal of Geophysical Research: Solid Earth (1978–2012)*, *88*(B2), 1153-1172.

De, R., & Kayal, J. R. (2003). Seismotectonic model of the Sikkim Himalaya: Constraint from microearthquake surveys. *Bulletin of the Seismological Society of America*, *93*(3), 1395-1400.

DeCelles, P. G., & Mitra, G. (1995). History of the Sevier orogenic wedge in terms of critical taper models, northeast Utah and southwest Wyoming.*Geological Society of America Bulletin*, *107*(4), 454-462.

DeCelles, P. G., Gehrels, G. E., Quade, J., & Ojha, T. P. (1998). Eocene-early Miocene foreland basin development and the history of Himalayan thrusting, western and central Nepal. *Tectonics*, *17*(5), 741-765.

DeCelles, P. G., Robinson, D. M., Quade, J., Ojha, T. P., Garzione, C. N., Copeland, P., & Upreti, B. N. (2001). Stratigraphy, structure, and tectonic evolution of the Himalayan fold-thrust belt in western Nepal. *Tectonics*, *20*(4), 487-509.

Dodson, M. H. (1973). Closure temperature in cooling geochronological and petrological systems. *Contributions to Mineralogy and Petrology*, *40*(3), 259-274.

Duncan, C., Masek, J., & Fielding, E. (2003). How steep are the Himalaya? Characteristics and implications of along-strike topographic variations. *Geology*,*31*(1), 75-78.

Edwards, M. A., & Harrison, T. M. (1997). When did the roof collapse? Late Miocene north-south extension in the high Himalaya revealed by Th-Pb monazite dating of the Khula Kangri granite. *Geology*, *25*(6), 543-546.

Ehlers, T. A., & Farley, K. A. (2003). Apatite (U–Th)/He thermochronometry: methods and applications to problems in tectonic and surface processes. *Earth and Planetary Science Letters*, *206*(1), 1-14.

Ehlers, T. A. (2005). Crustal thermal processes and the interpretation of thermochronometer data. *Reviews in Mineralogy and Geochemistry*, *58*(1), 315-350.

England, P., & Molnar, P. (1990). Surface uplift, uplift of rocks, and exhumation of rocks. *Geology*, *18*(12), 1173-1177.

England, P., Le Fort, P., Molnar, P., & Pêcher, A. (1992). Heat sources for Tertiary metamorphism and anatexis in the Annapurna-Manaslu Region central Nepal.*Journal of Geophysical Research: Solid Earth (1978–2012)*, *97*(B2), 2107-2128.

Farley, K. A., Wolf, R. A., & Silver, L. T. (1996). The effects of long alpha-stopping distances on (U- Th)/He ages. *Geochimica et Cosmochimica Acta*, *60*(21), 4223-4229.

Farley, K. A. (2002). (U-Th)/He dating: Techniques, calibrations, and applications.*Reviews in Mineralogy and Geochemistry*, *47*(1), 819-844.

Fellin, M.G. (2011). Personal communication.

Gaetani, M., & Garzanti, E. (1991). Multicyclic history of the Northern India continental margin (Northwestern Himalaya) (1). *AAPG Bulletin*, *75*(9), 1427-1446.

Ganguly, J., Dasgupta, S., Cheng, W., & Neogi, S. (2000). Exhumation history of a section of the Sikkim Himalayas, India: records in the metamorphic mineral equilibria and compositional zoning of garnet. *Earth and Planetary Science Letters*,*183*(3), 471-486.

Gansser, A. (1964). Geology of the Himalayas. (p.289). International Publishers, London and New York.

Gansser, A. (1983) Geology of the Bhutan Himalaya, (p.181), Birkhauser Verlag.

Ghosh, A. K. (1968). Quantitative analysis of polymetallic orebody zoning at Rangpo, Sikkim. *Economic Geology*, *63*(6), 682-687.

Godin, L., Grujic, D., Law, R. D., & Searle, M. P. (2006). Channel flow, ductile extrusion and exhumation in continental collision zones: an introduction. *Geological Society, London, Special Publications*, *268*(1), 1-23.

Grujic, D., Hollister, L. S., & Parrish, R. R. (2002). Himalayan metamorphic sequence as an orogenic channel: insight from Bhutan. *Earth and Planetary Science Letters*, *198*(1), 177-191.

Grujic, D., Coutand, I., Bookhagen, B., Bonnet, S., Blythe, A., & Duncan, C. (2006). Climatic forcing of erosion, landscape, and tectonics in the Bhutan Himalayas. *Geology*, *34*(10), 801-804.

Grujic, D., Warren, C. J., & Wooden, J. L. (2011). Rapid synconvergent exhumation of Miocene-aged lower orogenic crust in the eastern Himalaya.*Lithosphere*, *3*(5), 346-366.

Harris, N., & Massey, J. (1994). Decompression and anatexis of Himalayan metapelites. *Tectonics*, *13*(6), 1537-1546.

Harris, N. B. W., Caddick, M., Kosler, J., Goswami, S., Vance, D., & Tindle, A. G. (2004). The pressure–temperature–time path of migmatites from the Sikkim Himalaya. *Journal of Metamorphic Geology*, *22*(3), 249-264.

Hauck, M. L., Nelson, K. D., Brown, L. D., Zhao, W., & Ross, A. R. (1998). Crustal structure of the Himalayan orogen at∼ 90 east longitude from Project INDEPTH deep reflection profiles. *Tectonics*, *17*(4), 481-500.

Herman, F., Copeland, P., Avouac, J. P., Bollinger, L., Mahéo, G., Le Fort, P., ... & Henry, P. (2010). Exhumation, crustal deformation, and thermal structure of the Nepal Himalaya derived from the inversion of thermochronological and thermobarometric data and Modelling of the topography. *Journal of Geophysical Research: Solid Earth (1978–2012)*, *115*(B6).

Hirschmiller, J., Grujic, D., Bookhagen, B., Coutand, I., Huyghe, P., Mugnier, J. L., & Ojha, T. (2014). What controls the growth of the Himalayan foreland fold-and-thrust belt?. *Geology*, *42*(3), 247-250.

Hodges, K. V., Parrish, R. R., Housh, T. B., Lux, D. R., Burchfiel, B. C., Royden, L. H., & Chen, Z. (1992). Simultaneous Miocene extension and shortening in the Himalayan orogen. *Science*, *258*(5087), 1466-1470.

Hodges, K. V., Parrish, R. R., & Searle, M. P. (1996). Tectonic evolution of the central Annapurna range, Nepalese Himalayas. *Tectonics*, *15*(6), 1264-1291.

Hodges, K. V. (2000). Tectonics of the Himalaya and southern Tibet from two perspectives. *Geological Society of America Bulletin*, *112*(3), 324-350.

Hodges, K. V., Wobus, C., Ruhl, K., Schildgen, T., & Whipple, K. (2004). Quaternary deformation, river steepening, and heavy precipitation at the front of the Higher Himalayan ranges. *Earth and Planetary science letters*, *220*(3), 379-389.

Hourigan, J. K., Reiners, P. W., & Brandon, M. T. (2005). U-Th zonation-dependent alpha-ejection in (U-Th)/He chronometry. *Geochimica et Cosmochimica Acta*,*69*(13), 3349-3365.

Jade, S. (2004). Estimates of plate velocity and crustal deformation in the Indian subcontinent using GPS geodesy. *Current Science*, *86*(10), 1443-1448.

Jamieson, R. A., & Beaumont, C. (2013). On the origin of orogens. *Geological Society of America Bulletin*, *125*(11-12), 1671-1702.

Jouanne, F., Mugnier, J. L., Pandey, M. R., Gamond, J. F., Le Fort, P., Serrurier, L., ... & Avouac, J. P. (1999). Oblique convergence in the Himalayas of western Nepal deduced from preliminary results of GPS measurements. *Geophysical Research Letters*, *26*(13), 1933-1936.

Kellett, D. A., & Grujic, D. (2012). New insight into the South Tibetan detachment system: Not a single progressive deformation. *Tectonics*, *31*(2).

Kellett, D. A., Grujic, D., Coutand, I., Cottle, J., & Mukul, M. (2013). The South Tibetan detachment system facilitates ultra rapid cooling of granulite-facies rocks in Sikkim Himalaya. *Tectonics*, *32*(2), 252-270..

Larson, K. M., Bürgmann, R., Bilham, R., & Freymueller, J. T. (1999). Kinematics of the India-Eurasia collision zone from GPS measurements. *Journal of Geophysical Research: Solid Earth (1978–2012)*, *104*(B1), 1077-1093.

Lavé, J., & Avouac, J. P. (2000). Active folding of fluvial terraces across the Siwaliks Hills, Himalayas of central Nepal. *Journal of Geophysical Research: Solid Earth (1978–2012)*, *105*(B3), 5735-5770.

Lavé, J., & Avouac, J. P. (2001). Fluvial incision and tectonic uplift across the Himalayas of central Nepal. *Journal of Geophysical Research: Solid Earth (1978–2012)*, *106*(B11), 26561-26591.

Le Fort, P. (1975). Himalayas: the collided range. Present knowledge of the continental arc. *Am. J. Sci*, *275*(1), 1-44.

Le Fort, P., Cuney, M., Deniel, C., France-Lanord, C., Sheppard, S. M. F., Upreti, B. N., & Vidal, P. (1987). Crustal generation of the Himalayan leucogranites.*Tectonophysics*, *134*(1), 39-57.

Leloup, P. H., Mahéo, G., Arnaud, N., Kali, E., Boutonnet, E., Liu, D., ... & Haibing, L. (2010). The South Tibet detachment shear zone in the Dinggye area: Time constraints on extrusion models of the Himalayas. *Earth and Planetary Science Letters*, *292*(1), 1-16.

Long, S., McQuarrie, N., Tobgay, T., Rose, C., Gehrels, G., & Grujic, D. (2011). Tectonostratigraphy of the Lesser Himalaya of Bhutan: Implications for the along-strike stratigraphic continuity of the northern Indian margin. *Geological Society of America Bulletin*, *123*(7-8), 1406-1426.

Macfarlane, A. M. (1995). An evaluation of the inverted metamorphic gradient at Langtang National Park, central Nepal Himalaya. *Journal of Metamorphic Geology*,*13*(5), 595-612.

Makovsky, Y., Klemperer, S. L., Huang, L., & Lu, D. (1996). Structural elements of the southern Tethyan Himalaya crust from wide-angle seismic data. *Tectonics*,*15*(5), 997-1005.

Mancktelow, N. S., & Grasemann, B. (1997). Time-dependent effects of heat advection and topography on cooling histories during erosion. *Tectonophysics*,*270*(3), 167-195.

Mancktelow, N. S., & Grasemann, B. (1997). Time-dependent effects of heat advection and topography on cooling histories during erosion. *Tectonophysics*,*270*(3), 167-195.

McQuarrie, N., Robinson, D., Long, S., Tobgay, T., Grujic, D., Gehrels, G., & Ducea, M. (2008). Preliminary stratigraphic and structural architecture of Bhutan: Implications for the along strike architecture of the Himalayan system. *Earth and Planetary Science Letters*, *272*(1), 105-117.

Meesters, A. G. C. A., & Dunai, T. J. (2005). A noniterative solution of the (U-Th)/He age equation. *Geochemistry, Geophysics, Geosystems*, *6*(4).

Meigs, A. J., Burbank, D. W., & Beck, R. A. (1995). Middle-late Miocene (> 10 Ma) formation of the Main Boundary thrust in the western Himalaya. *Geology*, *23*(5), 423-426.

Min, K., Farley, K. A., Renne, P. R., & Marti, K. (2003). Single grain (U–Th)/He ages from phosphates in Acapulco meteorite and implications for thermal history. *Earth and Planetary Science Letters*, *209*(3), 323-336.

Mitra, G. (1997). Evolution of salients in a fold-and-thrust belt: the effects of sedimentary basin geometry, strain distribution and critical taper. In *Evolution of Geological Structures in Micro-to Macro-scales* (pp. 59-90). Springer Netherlands.

Mitra, G., Bhattacharyya, K., & Mukul, M. (2010). The Lesser Himalayan duplex in Sikkim: Implications for variations in Himalayan shortening. *Journal of the Geological Society of India*, *75*(1), 289-301.

Mohan, A., Windley, B. F., & Searle, M. P. (1989). Geothermobarometry and development of inverted metamorphism in the Darjeeling-Sikkim region of the eastern Himalayan. *Journal of Metamorphic Geology*, *7*(1), 95-110.

Molnar, P., & Stock, J. M. (2009). Slowing of India's convergence with Eurasia since 20 Ma and its implications for Tibetan mantle dynamics. *Tectonics*, *28*(3).

Mottram, C. M., Argles, T. W., Harris, N. B. W., Parrish, R. R., Horstwood, M. S. A., Warren, C. J., & Gupta, S. (2014). Tectonic interleaving along the Main Central Thrust, Sikkim Himalaya. *Journal of the Geological Society*, *171*(2), 255-268.

Mukul, M. (2000). The geometry and kinematics of the Main Boundary Thrust and related neotectonics in the Darjiling Himalayan fold-and-thrust belt, West Bengal, India. *Journal of Structural Geology*, *22*(9), 1261-1283.

Mukul, M., Jaiswal, M., & Singhvi, A. K. (2007). Timing of recent out-of-sequence active deformation in the frontal Himalayan wedge: Insights from the Darjiling sub-Himalaya, India. *Geology*, *35*(11), 999-1002.

Mukul, M. (2010). First-order kinematics of wedge-scale active Himalayan deformation: Insights from Darjiling–Sikkim–Tibet (DaSiT) wedge. *Journal of Asian Earth Sciences*, *39*(6), 645-657.

Mukul, M., Jade, S., Bhattacharyya, A. K., & Bhusan, K. (2010). Crustal shortening in convergent orogens: Insights from global positioning system (GPS) measurements in northeast India. *Journal of the Geological Society of India*, *75*(1), 302-312.

Mukul, M., Jade, S., Ansari, K., & Matin, A. (2014). Seismotectonic implications of strike–slip earthquakes in the Darjiling–Sikkim Himalaya. *Current Science*, *106*(2), 198-210.

Nábělek, J., Hetényi, G., Vergne, J., Sapkota, S., Kafle, B., Jiang, M., ... & Huang, B. S. (2009). Underplating in the Himalaya-Tibet collision zone revealed by the Hi-CLIMB experiment. *Science*, *325*(5946), 1371-1374.

Najman, Y. (2006). The detrital record of orogenesis: a review of approaches and techniques used in the Himalayan sedimentary basins. *Earth-Science Reviews*,*74*(1), 1-72.

Nelson, K. D., Zhao, W., Brown, L. D., Kuo, J., Che, J., Liu, X., ... & Edwards, M.

(1996). Partially molten middle crust beneath southern Tibet: synthesis of project INDEPTH results. *Science*, *274*(5293), 1684-1688.

Neogi, S., Dasgupta, S., & Fukuoka, M. (1998). High P–T polymetamorphism, dehydration melting, and generation of migmatites and granites in the Higher Himalayan Crystalline Complex, Sikkim, India. *Journal of Petrology*, *39*(1), 61-99.

Pan, G., Ding, J., Yao, D. & Wang, L. (2004), Geological map of Qinghai-Xiang (Tibet) plateau and adjacent areas (1:1,500,000), Chengdu Institute of Geology and Mineral Resources, China Geological Survey, Chengdu Cartographic Publishing House, Chengdu, China.

Parrish, R. R., & Hodges, V. (1996). Isotopic constraints on the age and provenance of the Lesser and Greater Himalayan sequences, Nepalese Himalaya. *Geological Society of America Bulletin*, *108*(7), 904-911.

Patrait, M. R., & Achache, J. (1984). India-Eurasia collision chronology and its implications for crustal shortening and driving mechanisms of the plates.*Nature*, *311*(18), 615-621.

Paul, D. K., McNaughton, N. J., Chattopadhyay, S., & Ray, K. K. (1996). Geochronology and Geochemistry of the Lingtse Gneiss, Darjeeling-Sikkim Himalaya: revisited. *Journal of the Geological Society of India*, *48*(5), 497-506.

Pearson, O. N., & DeCelles, P. G. (2005). Structural geology and regional tectonic significance of the Ramgarh thrust, Himalayan fold-thrust belt of Nepal. *Tectonics*,*24*(4).

Reiners, P. W., Farley, K. A., & Hickes, H. J. (2002). He diffusion and (U–Th)/He thermochronometry of zircon: initial results from Fish Canyon Tuff and Gold Butte.*Tectonophysics*, *349*(1), 297-308.

Reiners, P. W., Spell, T. L., Nicolescu, S., & Zanetti, K. A. (2004). Zircon (U-Th)/He thermochronometry: He diffusion and comparisons with $^{40}Ar/^{39}Ar$ dating. *Geochimica et Cosmochimica Acta*, *68*(8), 1857-1887.

Reiners, P. W. (2005). Zircon (U-Th)/He thermochronometry. *Reviews in Mineralogy and Geochemistry*, *58*(1), 151-179.

Reiners, P. W., & Brandon, M. T. (2006). Using thermochronology to understand orogenic erosion. *Annu. Rev. Earth Planet. Sci.*, *34*, 419-466.

Reiners, P. W., & Nicolescu, S. (2006). Measurement of parent nuclides for (U-Th)/He chronometry by solution sector ICP-MS. ARHDL Report 1. *University of Arizona*.

Rickwood, P., & Sambridge, M. (2006). Efficient parallel inversion using the Neighbourhood Algorithm. *Geochemistry, Geophysics, Geosystems*, *7*(11).

Robert, X., Van Der Beek, P., Braun, J., Perry, C., Dubille, M., & Mugnier, J. L. (2009). Assessing Quaternary reactivation of the Main Central thrust zone (central Nepal Himalaya): New thermochronologic data and numerical Modelling. *Geology*,*37*(8), 731-734.

Robert, X., Van Der Beek, P., Braun, J., Perry, C., & Mugnier, J. L. (2011). Control of detachment geometry on lateral variations in exhumation rates in the Himalaya: Insights from low-temperature thermochronology and numerical Modelling. *Journal of Geophysical Research: Solid Earth (1978–2012)*, *116*(B5).

Rubatto, D., Chakraborty, S., & Dasgupta, S. (2013). Timescales of crustal melting in the Higher Himalayan Crystallines (Sikkim, Eastern Himalaya) inferred from trace element-constrained monazite and zircon chronology. *Contributions to Mineralogy and Petrology*, *165*(2), 349-372.

Sambridge, M. (1999a). Geophysical inversion with a neighbourhood algorithm—I. Searching a parameter space. *Geophysical Journal International*, *138*(2), 479-494.

Sambridge, M. (1999b). Geophysical inversion with a neighbourhood algorithm—II. Appraising the ensemble. *Geophysical Journal International*, *138*(3), 727-746.

Schelling, D., & Arita, K. (1991). Thrust tectonics, crustal shortening, and the structure of the far-eastern Nepal Himalaya. *Tectonics*, *10*(5), 851-862.

Schelling, D. (1992). The tectonostratigraphy and structure of the eastern Nepal Himalaya. *Tectonics*, *11*(5), 925-943.

Schopf, J. W., Tewari, V. C., & Kudryavtsev, A. B. (2008). Discovery of a new Chert-Permineralized Microbiota in the Proterozoic Buxa Formation of the Ranjit window, Sikkim, northeast India, and its astrobiological implications. *Astrobiology*, *8*(4), 735-746.

Schwan, W., & Saklani, P. S. (1980). *Shortening structures in eastern and northwestern Himalayan rocks* (Vol. 3). Today and Tomorrow's Printers & Publishers.

Searle, M. P., Cooper, D. J. W., Rex, A. J., Herren, E., Rex, A. J., & Colchen, M. (1988). Collision Tectonics of the Ladakh--Zanskar Himalaya [and Discussion].*Philosophical Transactions of the Royal Society of London. Series A, Mathematical and Physical Sciences*, 117-150.

Searle, M. P., & Rex, A. J. (1989). Thermal model for the Zanskar Himalaya. *Journal of Metamorphic Geology*, *7*(1), 127-134.

Searle, M. P., Simpson, R. L., Law, R. D., Parrish, R. R., & Waters, D. J. (2003). The structural geometry, metamorphic and magmatic evolution of the Everest massif, High Himalaya of Nepal–South Tibet. *Journal of the Geological Society*,*160*(3), 345-366.

Searle, M. P., & Szulc, A. G. (2005). Channel flow and ductile extrusion of the high Himalayan slab-the Kangchenjunga–Darjeeling profile, Sikkim Himalaya. *Journal of Asian Earth Sciences*, *25*(1), 173-185.

Searle, M. P., Law, R. D., & Jessup, M. J. (2006). Crustal structure, restoration and evolution of the Greater Himalaya in Nepal-South Tibet: implications for channel flow and ductile extrusion of the middle crust. *Geological Society, London, Special Publications*, *268*(1), 355-378.

Segev, A. (2002). Flood basalts, continental breakup and the dispersal of Gondwana: evidence for periodic migration of upwelling mantle flows (plumes).*EGU Stephan Mueller Special Publication Series*, *2*, 171-191.

Strutt, R. J. (1908). On the accumulation of helium in geological time. *Proceedings of the Royal Society of London. Series A*, *81*(547), 272-277.

Stüwe, Kurt, and Terence D. Barr. On uplift and exhumation during convergence.*Tectonics,* 17.1 (1998): 80-88.

Tiwari, V. M., Vyghreswara Rao, M. B. S., Mishra, D. C., & Singh, B. (2006). Crustal structure across Sikkim, NE Himalaya from new gravity and magnetic data. *Earth and Planetary Science Letters*, *247*(1), 61-69.

Urey, H. C. (1955). The cosmic abundances of potassium, uranium, and thorium and the heat balances of the Earth, the Moon, and Mars. *Proceedings of the National Academy of Sciences of the United States of America*, *41*(3), 127.

Vermeesch, P. (2008). Three new ways to calculate average (U–Th)/He ages.*Chemical Geology*, *249*(3), 339-347.

Whipp, D. M., Ehlers, T. A., Blythe, A. E., Huntington, K. W., Hodges, K. V., & Burbank, D. W. (2007). Plio-Quaternary exhumation history of the central Nepalese Himalaya: 2. Thermokinematic and thermochronometer age prediction model.*Tectonics*, *26*(3).

Whipple, K. X., & Meade, B. J. (2006). Orogen response to changes in climatic and tectonic forcing. *Earth and Planetary Science Letters*, *243*(1), 218-228.

Whipple, K. X. (2009). The influence of climate on the tectonic evolution of mountain belts. *Nature Geoscience*, *2*(2), 97-104.

Willett, S. D., & Brandon, M. T. (2002). On steady states in mountain belts. *Geology*,*30*(2), 175-178.

Wobus, C., Heimsath, A., Whipple, K., & Hodges, K. (2005). Active out-of-sequence thrust faulting in the central Nepalese Himalaya. *Nature*, *434*(7036), 1008-1011.

Wolf, R. A., Farley, K. A., & Kass, D. M. (1998). Modelling of the temperature sensitivity of the apatite (U–Th)/He thermochronometer. *Chemical Geology*, *148*(1), 105-114.

Wu, C., Nelson, K. D., Wortman, G., Samson, S. D., Yue, Y., Li, J., ... & Edwards, M. A. (1998). Yadong cross structure and South Tibetan Detachment in the east central Himalaya (89–90 E). *Tectonics*, *17*(1), 28-45.

Zhang, H., Harris, N., Parrish, R., Kelley, S., Zhang, L., Rogers, N., ... & King, J. (2004). Causes and consequences of protracted melting of the mid-crust exposed in the North Himalayan antiform. *Earth and Planetary Science Letters*, *228*(1), 195-212.

APPENDIX A - Bedrock Sample Information

Sample #	Location		Elevation (m)	Unit	Geology	Zircon (U-Th)/He Age (Ma)	Error (Ma)
	°N	°E					
ISIK08-01	26°53.089'	88°28.427'	228	Lower to Middle Siwaliks	Coarse-grained sandstone with flat lamination and also cross-bedding	12.94	1.05
ISIK08-03	26°54.938'	88°27.800'	201	Upper Siwaliks	Very coarse-grained sandstones with conglomeratic intercalations	10.90	1.10
ISIK08-04	26°55.462'	88°27.292'	181	Lower Siwaliks (?)	Fine-grained blue sandstone	273.59	29.80
ISIK08-05	26°55.462'	88°27.292'	181	Gondwana	Thin layers of fine-grained sandstones and quartz-rich layers	11.87	0.49
ISIK08-07	27°2.284'	88°25.612'	215	Daling	Coarser-grained than at the bridge with even mmic eyes of Fk in a greenish matrix	8.33	1.05
ISIK08-08	27°0.623'	88°25.516'	794	Daling/ Reyang?	Quartzites	6.62	0.48
ISIK08-09	27°0.957'	88°22.360'	1162	Daling / Reyang	Finely layered quartzite with muscovite schist interbeds	8.89	0.25
ISIK08-10	27°2.285'	88°20.752'	1729	GHS	Migmatitic gneisses with large muscovite, Bt + Ga. Q-Fe veins.	9.34	0.36
ISIK08-11	27°01.099'	88°18.131'	2088	GHS	Migmatitic gneisses	10.41	0.78
ISIK08-34	27°18.334'	88°22.063'	1923	Daling		1.99	0.08
ISIK08-36	27°08.101'	88°16.770'	326	Gondwana/Daling?	Slates+medium-grained sandstones	3.50	0.25
ISIK08-37	27°11.089'	88°19.026'	457	Gondwana?	Massive and coarse-grained sandstones	3.90	0.25
ISIK08-38	27°31.468'	88°11.044'	3978	GHS	Pegmatites	2.81	0.27
ISIK08-39	27°36.184'	88°11.271'	4909	GHS	Augengneiss	3.29	0.25
ISIK08-41	27°28.932'	88°10.746'	3761	GHS	Granite	2.07	0.16
ISIK08-42	27°25.481'	88°11.483'	2237	GHS	Gneiss Bt+Qtz+Grt	1.30	0.07
ISIK08-44	27°21.845'	88°13.467'	1571	GHS	Gneiss Bt+Qtz+Grt	1.45	0.19
ISIK08-45	27°20.700'	88°15.771'	1509	Daling	Sandstone	1.80	0.30

APPENDIX B - Contributions to the Thesis

Sample collection was performed by supervisor Dr. Isabelle Coutand in 2008 who provided the sample descriptions, context and location information compiled in Appendix A. Samples were collected in a profile perpendicular to the major structures in Sikkim and crossing the windows. The profile followed the major river valleys up from the Siwaliks in the south to base camp of Kangchenjunga. Crushing of approximately half of the samples was performed by lab technician Matt Kliffer with the rest performed by myself. I processed all of the samples through crystal isolation for zircons and selected the zircons for analysis.

Degassing of 25 zircons was performed by noble gas technician Keith Taylor at Dalhousie. The remaining degassing and all of the U-Th extraction was performed by me under the supervision of Dr. Jeremy Hourigan at UCSC. The original model code for Pecube was compiled by Jean Braun (Braun, 2003) and modified by Dr. David Whipp for use in this study. All forward models were run using my personal computer and all inversions were run using the Ace-net Glooscap computing cluster.